CLUSTER-BASED ORGANOMETALLIC POLYMERS AND COMPUTATIONAL DESIGN OF [3]RADIALENE DERIVATIVES

by

Jonathan H. Gillen

A dissertation submitted to the faculty of
The University of North Carolina at Charlotte
in partial fulfillment of the requirements
for the degree of Doctor of Philosophy in
Chemistry & Nanoscale Science

Charlotte

2024

Approved by:

____
Dr. Christopher Bejger

____
Dr. Jordan C. Poler

____
Dr. Daniel Rabinovich

____
Dr. Thomas A. Schmedake

____
Dr. Tsing-Hua Her

ABSTRACT

JONATHAN HUNTER GILLEN. Cluster-Based Organometallic Polymers and
Computational Design of [3]Radialene Derivatives.
(Under the direction of DR. CHRISTOPHER BEJGER)

Herein we describe the first main-chain organometallic polymer in which the directionality is not dictated by the poly-N-heterocyclic carbene, but rather that of the precise coordination geometry of metal-sulfide cubane clusters, including a synthetic analogue of biologically ubiquitous, fully ferrous Fe_4S_4 cubane cluster. These charge-delocalized metal-sulfide cubane clusters are crucial to metalloenzymes yet largely unexplored within the realm of reticular chemistry. Such clusters can also be extracted from the polymers pos-synthetically with excess of the original stabilizing N-heterocyclic carbene (NHC) ligands. The surprising reversibility of these organometallic bonds provides strong evidence for possible modulation synthetic approaches. The discrete cubanes are also shown to form, surprisingly, solution processible superatomic ion pairs with fullerene. Main-chain organometallic polymers (MCOPs) formed from these superatomic ion pairs have electrical conductivities far exceeding that of their constituents or MCOPs formed from other cluster-ion pairs.

Lastly, a computational investigation of hexa-substituted [3]radialenes as redox flow battery materials (RFBs) is described. Computational methods were used to better understand the dimerization of a series of -cyano -ester substituted [3]radialene derivatives. Additionally, preliminary density functional theory (DFT) methods for identifying suitable derivatives for synthesis were investigated. Specific emphasis is placed on readily calculated properties including Mulliken spin density and buried volume. The unifying

theme of our research has been tunability. From the superatomic building blocks, N-heterocyclic carbene linkers, to hexa-substituted [3]radialenes our lab has explored constituents with extraordinary degrees of synthetic flexibility. Thus, the broader impacts of this research are not restrained to the specific molecules described within.

ACKNOWLEDGEMENTS

Scientists are gamblers. Often not of our own money, but nothing short of our time and lives. We sit down where other scientists have left off in hopes of grasping what they could not. We seek mysteries we do not yet understand and often walk away with prizes we were not looking for. Creation itself is the house, and even a glimmer of its wealth is enough to make many of us lifelong addicts. Those who often pay the most for our gambling addiction are those who love us the most. As such I have many loved ones and enablers I need to thank.

Thank you to my advisor, Dr. Bejger! You took me on as a novice to the field of chemistry and from the beginning you have encouraged and sharpened my own creativity in this once unfamiliar field. As any general chemistry TA can attest, the principles of wet chemistry are often learned through error, and I appreciate the patience of you and my fellow collaborators during those early years. To all my collaborators, you have all been topnotch, and it has been a sincere pleasure to work with and learn from every one of you.

Thank you to my committee and professors for your insights and for pushing me to be a better researcher and to crack more books. For keeping Burson running I must give thanks to the whole chemistry department and facilities management, but a special thanks to Dr. Jon Merkert, Paul Brainbridge, Rebecca Hawes, Liz Buttler, and Joconda Guertin. To my classmate, colleague, and friend, Dr. Adam Fessler, thank you for your support for me and our lab. In many ways all Burson graduate students are collaborators, and I thank you all for sharing your instrumentation knowledge, chemicals, and camaraderie. One of the greatest pleasures I have had during my time here has been working one on one with dozens of undergraduates and highschoolers in the lab. Your love of science and curiosity are refreshing, and I wish you all the best in your endeavors.

To my parents, you have loved, encouraged, and pushed me my whole life. I may not be a child anymore, but I still hope to grow up to be like you some day, thank you. To my brother, my closest of friends, you are a constant source of motivation. To my whole family, you have all been a blessing and encouragement all the days of my life. To my families away from home, Colsons, Yandles, and all of University Hills Baptist Church, I would not have been able to persevere without your support. Finally, I thank God for the countless blessings I have had in my life. Family, friends, opportunities, health; in any way that really matters I have been blessed. While I was here in Charlotte with the opportunity to get a degree in nanoscale science, I met the greatest blessing of them all, my wife. Karen, I love you. Thank you for your continual love, support, and sacrifices over all these years I have been in school.

DEDICATION

To my greatest blessing, wife, and mother of our child

I love you and I would not be here without you.

TABLE OF CONTENTS

LIST OF TABLES ix

LIST OF FIGURES x

LIST OF ABBREVIATIONS xiii

CHAPTER 1: INTRODUCTION 1

- 1.1 Reticular Chemistry 1
- 1.2 Superatoms 6
- 1.3 Metal-Chalcogenide Clusters 8
- 1.4 Cubane Cluster 11
- 1.5 N-heterocyclic Carbenes 15
- 1.6 Redox Flow Batteries 17
- 1.7 Radialenes 19
- 1.8 Dissertation Summary 23

CHAPTER 2: MAIN-CHAIN ORGANOMETALLIC POLYMERS 26

- 2.1 Introduction 26
- 2.2 Experimental 28
  - 2.2.1 Chemicals 28
  - 2.2.2 Instrumentation 29
  - 2.2.3 Synthesis 32
- 2.3 Results and Discussion 35
- 2.4 Conclusions 43
- 2.5 Appendix A: Chapter 2 Supplementary Information 44
  - 2.5.1 Single Crystal X-ray Diffraction Figures 44

2.5.2 Scanning Electron Micrographs & Energy Dispersive X-ray Spectroscopy 45

2.5.3 Nuclear Magnetic Resonance Spectroscopy 46

2.5.4 Infrared Spectroscopy 48

2.5.5 X-ray photoelectron spectroscopy 48

2.5.6 UV-Vis Absorption Spectroscopy 51

2.5.7 Surface Area Analysis 51

2.5.8 Electrochemistry 52

2.5.9 Digestion/Excision Experiment 53

2.5.10 SEM Micrographs of Modulated Polymerization 53

2.5.11 Pre and Post Cyclic Voltammetry SEM/EDS Study 54

2.5.12 Characterization of Co4S4-MCOP-Et 54

2.5.13 X-ray Diffraction Procedures and Tables 55

CHAPTER 3: CONDUCTIVE ORGANOMETALLIC POLYMERS FROM SOLUBLE SUPERATOM IONS 59

3.1 Introduction 59

3.2 Experimental 61

3.2.1 Chemicals 61

3.2.1 Synthesis 61

3.2.1 Characterization 65

3.3 Results and Discussion 69

3.4 Conclusions 78

3.5 Appendix B: Chapter 3 Supplementary Information 80

3.5.1 SEM Micrographs of 1•C60 and 2•C60 80

3.5.2 Powder X-ray Diffraction 80

3.5.3 Energy dispersive X-ray spectrograph of 1•C60 81

3.5.4 Photographs of Dissolved Superatomic Crystals 1•C60 81

3.5.5 Electrochemical analysis of 1•C60 and 2•C60 82

3.5.6 UV-Vis-NIR Absorption Spectroscopy of 2•C60 83

3.5.7 NMR Spectroscopy of Dissolved Superatomic Crystals. 83

3.5.8 Scanning Electron Micrograph and EDS Survey of MCOP-2•C60 84

3.5.9 UV-Vis Absorption Spectroscopy of MCOP-2•C60 85

3.5.10 Characterization of MCOP-1 85

3.5.11 UV-vis-NIR studies of MCOPs Postsynthetically Doped with Fullerene. 88

3.5.12 Images of MCOP Postsynthetically Doped with Fullerene. 88

3.5.13 Electrical Conductivity Measurements 89

3.5.14 X-ray Diffraction Procedures and Tables 89

CHAPTER 4: COMPUTATIONAL SCREENING OF [3]RADIALENES FOR REDOX FLOW BATTERIES 92

4.1 Introduction 92

4.2 Experimental 94

4.3 Results and Discussion 97

4.3.1 [3]Radialene Dimerization Investigation 97

4.3.2 Screening of [3]Radialene Derivatives 100

4.4 Conclusions 104

4.5 Appendix C: Chapter 4 Supplementary Information 107

CHAPTER 5: CONCLUSIONS 120

REFERENCES 123

LIST OF TABLES

Table 1: Electrical Conductivities of Clusters, Cocrystals, and MCOPs in (mS/cm). 77

Table 2: DFT calculated interaction energies and max Mulliken spin densities of the σ-and π-dimers of **1-3.** 98

Table 3: DFT calculated $E^{1/2}$ experimental redox potentials vs those measured aqueously by CV vs a saturated Ag/AgCl reference. 101

LIST OF FIGURES

Figure 1.1 (a) Simplified crystal structure of $[Cu(ADI)_2](NO_3)$ (b) Representative network showing two points of extension as edges and nodes with four points of extensions highlighting the underlying dia topology. (c) Augmented dia-a net shown in its highest symmetry embedding by replacing vertices with representative polyhedra. Tetrahedral nodes are shown in blue, edges in gray. One adamantane cage is shown in (a) and highlighted in orange in (b) and (c). 3

Figure 1.2 Isoreticular synthesis of MOF-5 and IRMOF-3. IRMOF-3 highlights post-synthetic global introduction of amide groups yielding PSM-IRMOF3. Frameworks constructed from octahedral $Zn_4O(-CO_2)_6$ SBUs and linear ditopic 4-benzene-dicarboxylate linkers. The yellow sphere reveals the large spherical volume outside of the van der Waals radius of any framework atom. All hydrogen atoms are omitted for clarity. Color code: Zn, blue; C, gray; O, red. 4

Figure 1.3 An example of a superatomic crystal with the large blue and red spheres representing superatoms which remain unchanged after assembly. The different bond colors represent different inter-superatom interactions or bonding. Such materials can be assembled in solution and characterized by single-crystal X-ray diffraction. 7

Figure 1.4 An array of known phosphine stabilized metal-chalcogenide clusters with diverse structural motifs. 8

Figure 1.5 Diagram of a simple heterocubane cluster without ligands. A tetrahedron of metal atoms (black) and one of non-metal atoms (white) emphasizes coordination geometry. 11

Figure 1.6 Representation of Mo-nitrogenase from *Azotobacter vinelandii*. The Fe protein is shown in gray and the MoFe protein is shown in cyan. Fe = rust, S = yellow, C = gray, N = blue, O = red, Mo = cyan, Mg = green. 13

Figure 1.7 Cartoon illustration of a generic protein (center) containing Fe_4S_4 cubane cluster showing conventional modifications used by biology to tune reduction potential from low to high. 14

Figure 1.8 (a) structural features of first isolable NHC highlighting the structural influences on stability and reactivity. (b) ground-state structure of imidazol-2-ylidenes depicting the stabilizing σ-withdrawing and π-donating effects of the nitrogen heteroatoms. (c) Primary molecular orbitals involved in an NHC-M bond. 16

Figure 1.9 Schematic of a conventional redox flow battery. 18

Figure 1.10 A computational benchmark of lifetime cost for organic aqueous RFB electrolytes highlighting the promise of these materials to surpass current vanadium RFBs, but with catholytes trailing behind anolytes. 21

Figure 1.11 Examples of [3]radialene compounds and their electrochemical properties in aqueous solutions. 23

Figure 2.1 Synthesis of $[Co_4S_4(Pr^i_2NHCBz)_4]$ (**2**) and Co_4S_4-MCOP. Single crystal X-ray structure of **2**. Hydrogen atoms omitted. 36

Figure 2.2 (a) Synchrotron powder X-ray diffraction pattern of Co_4S_4-MCOP (black) and simulated pattern (red) of model (inset), (b) normalized UV-vis absorption spectra (inset image of Co_4S_4-MCOP in epoxy) and (c) TGA traces of Co_4S_4-MCOP (purple), 2 (green), and 1 (orange), and (d) cyclic voltammograms of Co_4S_4-MCOP (purple; solid-state modified glassy carbon working electrode), 2 (green), and background (blue dashed). Recorded at 100 mV s^{-1} in MeCN with $TBAPF_6$. 39

Figure 2.3 NMR spectra overlay of Co_4S_4-MCOP (purple); $Pr^i_2NHCMe_2$ (blue); discrete $Co_4S_4(Pr^i_2NHCMe_2)_4$ (red); and mixture of Co_4S_4-MCOP and $Pr^i_2NHCMe_2$ after digestion (green) in C_6D_6. 42

Figure 3.1 Schematic of (a) superatomic crystals formed from electron-donor metal-chalcogenide clusters and fullerene acceptors. (b) Main-chain organometallic polymers formed from phosphine stabilized metal chalcogenide cluster and Janus N-heterocyclic carbenes. (c) Forming main-chain organometallic polymers via soluble superatomic ions from superatomic crystals. 59

Figure 3.2 Structure of **2•C$_{60}$** showing the crystal packing looking down the *c*-axis (a) and a single layer view down the *b*-axis (b). Hydrogen atoms are removed for clarity. Solvent atoms are omitted in (b). Carbon, black; cobalt, dark-blue; chlorine, green; nitrogen, light-blue; sulfur, yellow. 70

Figure 3.3 Characterization of **1•C$_{60}$**. (a) Photograph of **1•C$_{60}$** in *o*-DCB and graphical depiction of cluster electron transfer. (b) Cyclic voltammogram of **1•C$_{60}$** recorded at 100 mV s^{-1} in THF with $TBAPF_6$ using a glassy carbon working electrode. (c) UV-Vis-NIR spectra of **1** (red) and **1•C$_{60}$** (purple) in THF. 71

Figure 3.4 NMR spectroscopy studies of **2•C$_{60}$**. (a) ^{1}H NMR spectra of **2** and (b) **2•C$_{60}$** in chlorobenzene-d_5. All spectra recorded at 500 MHz. 73

Figure 3.5 Synthesis of M_4S_4•C_{60} superatomic crystals, organometallic polymers, and superatomic organometallic polymers. 74

Figure 3.6 Electrical properties of pressed pellets. Plots of current density versus electric field strength (*J–E*) curves at 297 K. 77

Figure 3.7 Single crystal x-ray structure of Co_4S_2(2,6-dimethylphenyl isocyanide$)_{10}$ with hydrogens omitted along with its CV measurements. 79

Figure 4.1 Visual representation of the multi-step screening process in which [3]radialene candidates for aqueous redox flow battery may be removed from a larger pool with successively more computationally intensive filters. 94

Figure 4.2 Radical stability score calculation on hexa-cyano [3]radialene using Paton's method. Showing a maximum normalized Mulliken spin density at three alpha carbons of 14.0%, a buried volume of 59.3% around atomic site of maximum spin density, and a resultant radical stability score of 102.3. 96

Figure 4.3 Hexa-substituted [3]radialene radical anions and their dimerization behavior in different solvents. 97

Figure 4.4 Gas optimized structures of hexa-cyano (1), di-ester (2), and tri-ester (3). Free radical (top), π-dimer (middle), and sigma-dimer (bottom). 99

Figure 4.5 Stability analysis of [3]radialene hexa-cyano derivatives (methyl ester series, methyl sulfone series, mono 4-benzonitrile, and mono amide). Green arrows show predicted increase in stability based off the derivatives ordered by radical stability score (top) or isolated maximum spin density metric (bottom). Red numbers indicate irreversible CV measurements. 102

Figure 4.6 Optimized structure of tri-pyridinium^{-1} in the lowest energy confirmation. Neighboring pyridiniums as shown are also the lowest energy confirmation for the dianion. 103

Figure 4.7 Synthesis of a predicted hexa-cyano [3]radialene di-ester derivative using dimethyl malonate showing a σ-dimer that can be broken with mechanical force. 105

LIST OF ABBREVIATIONS

^{13}C-NMR	carbon-13 nuclear magnetic resonance
^{1}H-NMR	proton nuclear magnetic resonance
^{31}P-NMR	phosphorus-31 nuclear magnetic resonance
(0-3)D	zero, one, two, or three-dimensional
BET	Brunauer-Emmett-Teller
COF	covalent organic framework
CV	cyclic voltammetry
EDS	energy dispersive spectroscopy
HiPIP	high-potential iron protein
IR	infrared
MCOP	main-chain organometallic polymer
MOF	metal organic framework
NHC	*N*-heterocyclic carbene
NHE	normal hydrogen electrode
NMR	nuclear magnetic resonance
$Pr^{i}_{2}NHCMe_{2}$	1,3-diisopropyl-4,5-dimethylimidazol-2-ylidene
RFB	redox flow battery
SCXRD	single-crystal X-ray diffraction
SEM	scanning electron microscopy
$TBAPF_6$	tetrabutylammonium hexafluorophosphate
TGA	thermal gravimetric analysis
XPS	X-ray photoelectron spectroscopy

ZIF	zeolitic imidazolate framework

CHAPTER 1: INTRODUCTION

1.1 Reticular Chemistry

Our journey began with one simple question. Can we apply the principles of reticular chemistry to superatoms? For most this raises two immediate questions. What is reticular chemistry and what are super atoms? Those questions will be answered herein briefly and thirdly why it matters. For we have yet to answer that original question in full, but this paper will describe the significant strides our laboratory has made toward expanding the use of reticular chemistry toward preassembled superatoms.

The geometry of atoms in space is something all chemists inevitably seek to understand. Even when not directly tackling this question, the beginning of any explanation for our observations will be found in how the atoms are connected into molecules and how those molecules interact with others. It is this very understanding that has allowed chemists to design the molecules (0D) and polymers (1D) that have shaped the 20th century.[1] The deliberate synthesis approaches of organic chemistry are so well developed now that near any reasonable target molecule can be made with a high precision.[2] The same cannot be said for metal complexes since metal ions introduce an inherent level of uncertainty due to their variable geometries and coordination numbers. Additionally functionalizing organic molecules can typically be pursued through multiple chemical reactions whereas metal complexes are largely modified exclusively through substitution-addition reactions due to their lower chemical stability. As such, a common element of metal-ion chemistry is often trial-and-error. It should be noted that complex multi-dentate ligands can often alleviate this uncertainty but are more challenging to design, especially for the polynuclear complexes investigated herein.

Over the 20th century, rational molecular-level design of periodic 2D (planar) and 3D (bulk) materials largely eluded material scientists. That is until the rapid development of reticular chemistry leading into the 21st century.[3] Reticular chemistry describes the methods by which well-defined molecular building blocks are linked by strong bonds into crystalline frameworks.[4-6] The pursuit of such a level of control requires two basic considerations: what is the directionality and type of interactions the linkages impart to the framework, and secondly what is the geometry and metrics of the molecular building units that will guide the synthesis toward a targeted structure.[7] An example of which can be seen in **Figure 1.1a** for which adiponitrile acts as a 2-connected linker while copper atoms coordinate as tetrahedral nodes, illustrated in **Figure 1.1c**. These structures are typically classified by a simplified net (**Figure 1.1b**) which is an assembly of nodes and links as coined by Alexander F. Wells.[8] These nets can be comprised of large discrete entities as in metal/covalent organic polyhedral or extended frameworks such as metal organic frameworks (MOFs)[9], zeolitic imidazolate frameworks (ZIFs)[10], and covalent organic frameworks (COFs).[11] In certain instances, frameworks behave as fundamentally extended molecules on which it is possible to carry out reactions while maintaining order and porosity. This chemistry has enabled the widescale synthesis of over a hundred thousand, as reported by the Cambridge Structural Database, highly modular and versatile frameworks over the past 25 years.[12]

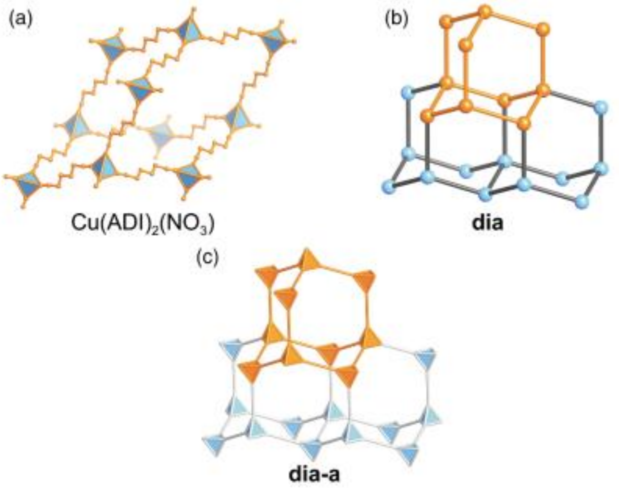

Figure 1.1 (a) Simplified crystal structure of [Cu(ADI)$_2$](NO$_3$) (b) Representative network showing two points of extension as edges and nodes with four points of extensions highlighting the underlying dia topology. (c) Augmented dia-a net shown in its highest symmetry embedding by replacing vertices with representative polyhedra. Tetrahedral nodes are shown in blue, edges in gray. One adamantane cage is shown in (a) and highlighted in orange in (b) and (c*). Adapted from Yaghi, O. M.; Kalmutzki, M. J.; Diercks, C. S. Introduction to reticular chemistry : metal-organic frameworks and covalent organic frameworks; Wiley-VCH, 2019, Copyright (2019), with permission from Elsevier.*

MOFs represent the vast majority of these structures, and the extensive research attributed to their development has had to address many challenges. As mentioned previously, the intrinsic ambiguity that metal ions bring, consequent of their coordination number and geometry, impede the very principles of design that rest upon well-defined building blocks. Exceptions to this may be found in circumstances for which a metal ion has a propensity for a specific arrangement, for which single metal ions are used as square, tetrahedral (**Figure 1.1**), and octahedral building blocks. However, the foundation of reticular chemistry, enabling high crystallinity and porosity, was built upon overcoming this coordination ambiguity by linking metal ions through the strong bonds of charged organic linkers, such as carboxylates. These polynuclear complexes lock the metal ions into positions such that the coordination geometry is determined by that of the cluster. Clusters of this type have been termed secondary building units (SBUs). The intrinsically larger metrics of these SBUs and organic linkers is why the reticular process consistently produces open structures. The strong bonding of the organic linkers forms rigid and directional SBUs allowing for the design of targeted structures with architectural stability facilitating permanent porosity. This permanent porosity enables functional modifications to be achieved throughout the extended structures post-synthetically (**Figure 1.2**). Furthermore, the ability to tailor the organic linker's size and functional groups enables isoreticular synthesis.[13] This results in the underlying structure type, e. g. primitive cubic lattice, being retained, but with unique pore functionality and metrics. It is this extreme level of control and constituent flexibility that has made the properties and applications of MOFs as varied as their structures.

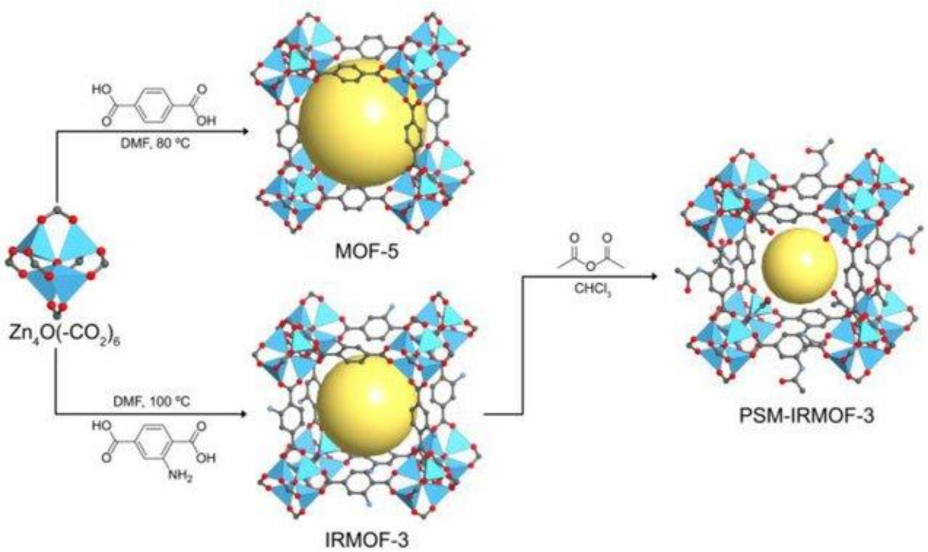

Figure 1.2 Isoreticular synthesis of MOF-5 and IRMOF-3. IRMOF-3 highlights post-synthetic global introduction of amide groups yielding PSM-IRMOF3. Frameworks are constructed from octahedral $Zn_4O(-CO_2)_6$ SBUs and linear ditopic 4-benzene-dicarboxylate linkers. The yellow sphere reveals the large spherical volume outside of the van der Waals radius of any framework atom. All hydrogen atoms are omitted for clarity. Color code: Zn, blue; C, gray; O, red. *Adapted with permission from Lyle, S. J.; Flaig, R. W.; Cordova, K. E.; Yaghi, O. M. Facilitating Laboratory Research Experience Using Reticular Chemistry. Journal of Chemical Education 2018, 95 (9), 1512-1519. Copyright 2018 American Chemical Society.*

The commercial significance of MOFs has so far paled in comparison to that of the class of purely inorganic crystalline porous materials known as zeolites.[14] These materials are comprised of tetrahedral Si and/or Al metal ions linked by oxide ions at approximately 144º M-O-M angles. These produce homogeneously sized and shaped micropores possessing high thermal stability which have become benchmarks for size-selective molecular absorbents, catalysts, and ion exchangers. There are currently less than 300 recognized zeolites due to the highly limited design and tunability of their atomic constituents, but even the modest tunability they do allow can markedly alter their applications. As any modern chemist can attest, sieves comprising pure silica are hydrophobic and can therefore be used to remove organic components from water while aluminosilicate sieves are hydrophilic and therefore absorb water from organic solvents.

Modest tuning of a zeolite can produce profound changes in application. Thus, even more can be expected from highly tunable reticular constituents. Alas, the coordination bonds that make up MOFs are inherently weaker than the fully inorganic covalent bonds that comprise zeolites. Moreover, MOFs regularly achieve pores much larger than zeolites which introduces further instability.[15] Much of the industrial success of zeolites can be attributed to their incredibly high thermal and chemical stability, which MOFs have yet to achieve due to their intrinsically weaker coordination bonds. Yet, it is evident from the literature that the synthetic flexibility of MOFs is unparalleled. The commercial success of MOFs will not be found in competing for the role of zeolites, but rather by enabling functionalities that no other material ever could. This leaves the onus of MOF’s success to the creativity of the researchers designing them.

1.2 Superatoms

Crystalline solids are foundational to modern technologies such as computers, solar cells, and lithium-ion batteries. Of which they are all built from 82 stable atomic building blocks. The solid-state chemistry on which these materials are derived relies upon the intrinsic bonding interactions of these atomic elements. When designing materials with tunable properties the control of a solid-state chemist is rather limited. For instance, the electronic properties of silicon can be tuned by the doping of minor impurities into the crystal lattice, but the atoms themselves cannot be tuned and any significant replacement of atoms that make up the crystal often leads to an entirely new structure with new properties. Further these materials are often derived from high temperature reactions producing thermodynamically stable compounds. However, nature’s organic systems take a very different approach, relying on the design of complex, tunable, metastable structures by assembling hierarchal materials from nanoscale building blocks. In this vein, clusters have emerged as appealing building blocks for modern solid-state chemists.[16] As depicted in **Figure 1.3,** these clusters can be synthesized and assembled in a variety of ways. This provides a large degree of control over the resulting solid-state material. Since these superatomic solids can often be assembled from an array of structurally comparable superatom analogues the possible materials with unique collective properties increases combinatorially with the available cluster analogues.

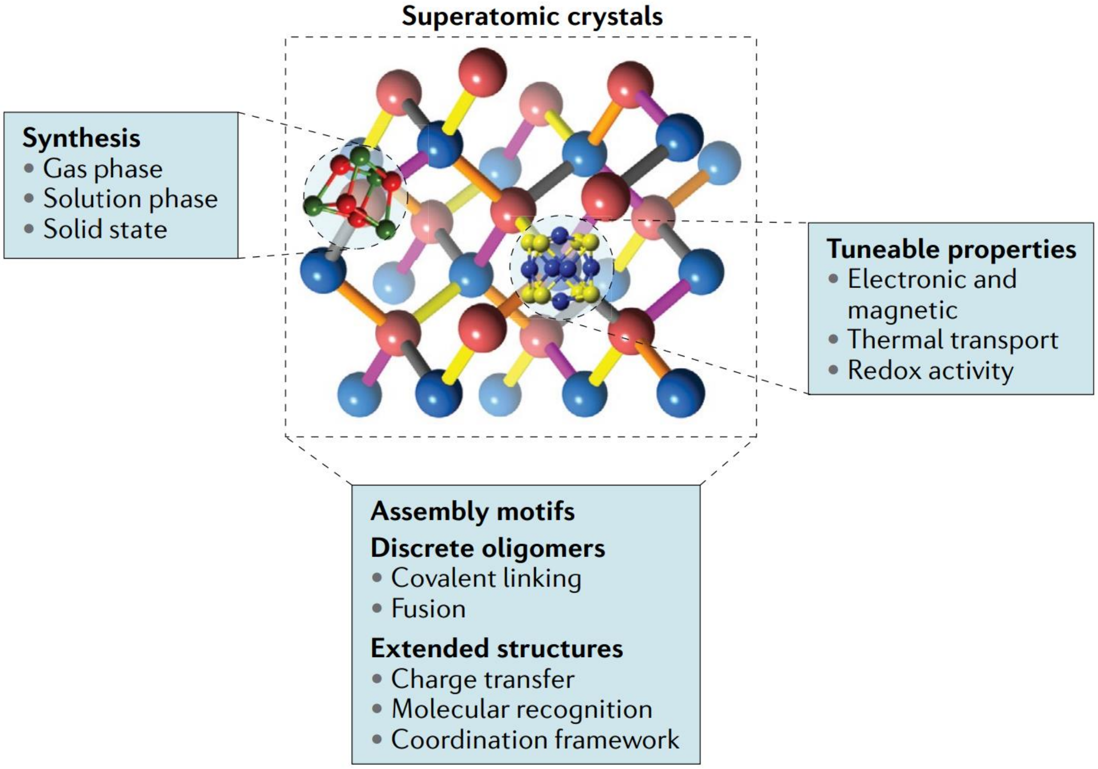

Figure 1.3 An example of a superatomic crystal with the large blue and red spheres representing superatoms which remain unchanged after assembly. The different bond colors represent different inter-superatom interactions or bonding. Such materials can be assembled in solution and characterized by single-crystal X-ray diffraction. *Reproduced with permission from [16] Springer Nature.*

Often, molecular clusters are made from ensembles of atoms and can be thought of as fragments of bulk materials.[17] Many clusters adopt structural motifs with particularly enhanced stability and collaborative behaviors. Such cooperative behavior often leads to such clusters being deemed as ‘superatoms’. Fullerenes, Zintl ions, boron, silicon, aluminum, noble metal ‘magic-number’, and metal chalcogenide clusters all fall under the general umbrella of superatoms.[16] Often, these clusters are stabilized with capping ligands, which can be used as handles for directing the self-assembly of oligomers and extended structures. The term superatom originally developed from the surprising theoretical realization that select atomic clusters like Al_{13}^{-} could form delocalized orbitals that strongly resembled atomic s, p, and d orbitals.[18] It is more broadly used to acknowledge any ensemble behaviors presenting atomic mimicry and with it the idea of superatomic materials built from these highly tunable constituents. The challenges of this burgeoning field are very similar to those of reticular chemistry and hinge on controlling the self-assembly of suitable building blocks through strong coupling. The antecedent to this goal is the identification of a superatom building block suitable for the anticipated assembly and applications.

1.3 Metal-Chalcogenide Clusters

Chalcogenide ions E^{2-}, including S, Se, and Te, can effectively bridge most of the transition metals. In part, this is due to their considerable polarizability and negative charges. In combination with strong stabilizing ligands, metal-chalcogenides can form clusters with a large variety of structural motifs (**Figure 1.4**). Many of these structural motifs can be accessed by a variety of transition metals and chalcogenides leading to highly tunable superatoms that can be used as constituents for a wide range of superatomic materials.[17, 19]

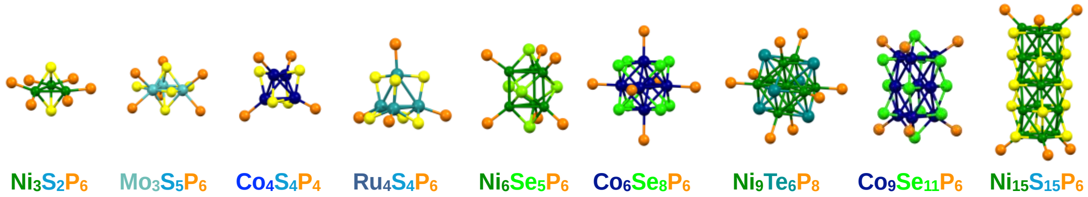

Figure 1.4 An array of known phosphine stabilized metal-chalcogenide clusters with diverse structural motifs.

Of the many metals that clusters can be assembled from, iron stands out from a biological perspective. The Earth-abundant transition metal iron is a catalytic cornerstone for reactions that are essential to all known life. Iron's catalytic properties are also indispensable to the industrial processes used to produce ammonia and hydrocarbon fuels through the Haber-Bosch process and Fischer-Tropsch synthesis.[20] These reactions are vital for meeting the food and energy demands of the current global economy but come at an immense energy cost from the temperatures and pressures required for sufficient catalytic activity. Yet, such transformations occur in nature under ambient conditions through metalloenzymes built around metal-chalcogenide based clusters.[21-23]

Enzymes selectively accelerate chemical reactions with 10 to 15-fold rate enhancements over uncatalyzed reactions through specific binding and catalysis while providing regio-, stereo-, and chemo- selectivity. This is achieved through the formation of an enzyme-substrate complex according to Michaelis-Menten kinetics which stabilizes the transition state, lowering the activation energy.[24] Accordingly the rate of the reaction is directly dependent on the concentration of the enzyme. The technical applications of such metalloenzymes are severely limited by their low thermal stability, poor environmental adaptability, limited substrate versatility, high cost of purification, and their homogeneous catalytic nature consequent of the protein environment.

Metalloproteins employ a variety of polynuclear clusters composed of iron, copper, zinc, nickel, molybdenum, and cobalt as essential redox active cofactors for energy harvesting, electron-transfer, and catalysis. Though among these iron-sulfur clusters are by far the most prevalent and biologically available. Synthetic metal chalcogenide active sites with ligands producing similar electronic structures have been synthesized, but in isolation lack the H-bond interactions, electrostatic interactions, and steric confinement that is necessary to stabilize critical transition states.[25] Isolated from the protein environment, these clusters have been shown to facilitate Fischer-Tropsch-like reactions in both aqueous and organic solvent environments[26]; however, no homogenous Fe-S cluster to date has been shown to facilitate the vital reduction of N_2 to NH_3 at any appreciable rate. Highlighting the essential role that the protein environment plays in catalysis.[27]

Catalysis was one of the earliest proposed applications for functional MOFs due to their tunable, uniform channel sizes and large internal surface area.[28] It has been noted that their inherent thermal stability barrier highlights the need for MOFs to develop as artificial enzyme models.[29, 30] For which their highly tunable pores make them ideal for imitating the protein pockets of these biological active sites, while providing a high density of heterogeneous binding sites that can accommodate both substrates and functionality inducing molecules. Unfortunately, most MOFs are built from charge-localized metal-oxo clusters that inhibit charge mobility unlike the redox-active, delocalized metal-sulfide clusters that are foundational to metalloenzymes.[31, 32] According to the Pearson hard-soft acid-base theory, chalcogenide ligands are considered "softer" and as such promote lower oxidation states in the metals they bridge.[33] This can be attributed to their strong pπ-dπ overlap with metals, unlike that of 2nd row nonmetals, O and N. Such charge delocalized SBUs enabling electron conduction and the necessary adaptation of reticular chemistry principles for metal-chalcogenide clusters are largely unexplored. The reader should be aware this work is not focused on catalysis, but it is the inspiration that drove us to investigate metal-chalcogenide superatoms and the synthetic challenges necessary for the engineering of these conjectural enzyme mimics. That said, conductive chalcogenide-based MOFs have electrochemical applications beyond electrocatalysis including batteries and supercapacitors.[34]

1.4 Cubane Cluster

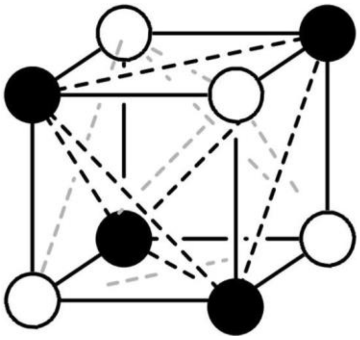

Figure 1.5 Diagram of a simple heterocubane cluster without ligands. Tetrahedron of metal atoms (black) and one of non-metal atoms (white) emphasizes coordination geometry. *Adapted from Bigness, A.; Vaddypally, S.; Zdilla, M. J.; Mendoza-Cortes, J. L. Ubiquity of cubanes in bioinorganic relevant compounds. Coordination Chemistry Reviews 2022, 450, 214168, Copyright (2022), with permission from Elsevier.*

The cubane cluster, or heterocubane, is an 8-membered molecular species comprising a cube shaped core with different atoms across the body diagonals (**Figure 1.5**). For the metal-chalcogenide cubane cluster the chalcogenide p-orbitals are unavailable for π-bonding, but in all μ_3 binding modes are ideally suited for σ-bonding, which is similar down the columns of nonmetals. Because of this, extensive synthetic exploration has shown that the cubane structural motif can be accessed with many different metal and bridging ligand atoms.[35] This structure's reactivity and versatility make it a universal redox cofactor for some of nature's most crucial enzymes. As a redox-innocent Lewis acid catalyst, substrate binding site, and reservoir for redox equivalents, iron-sulfur cubanes engage in both simple one-electron transfers as well as challenging reactions such as catalytic water splitting, nitrogen fixation, and the citric acid cycle.[36] This is in part due to the ability of cubanes to accommodate reduction potentials from as low as -600 mV (vs. NHE) in 7-Fe ferredoxin to as high as +400 mV in high-potential iron protein (HiPIP) with minimal structural or compositional variation.

Their extensive biological research can be attributed to their prevalence in essential metalloproteins. Further they are hypothesized to be a building block of the largely unknown cluster conversions that produce some nature's most essential and complex clusters.[37] Even beyond their biological relevance, cubane clusters have gripped the broader interest of chemists due purely to their tunable functions as synthetic redox, magnetic, and catalytic materials.[38-41]

Nitrogenase is the bacterial enzyme responsible for nitrogen fixation; the multielectron/proton reduction of molecular nitrogen to two ammonia molecules along with hydrogen. This is an essential process for life, since reduced nitrogen is not geologically prevalent. Despite the reduction of nitrogen to ammonia through hydrogen being exothermic, there exists a notoriously high energy barrier due to the necessary reductive cleaving of one of the strongest bonds in nature, the N-N triple bond. The Fe-protein of nitrogenase contains a single Fe_4S_4 cubane which in its fully reduced state is the sole reductase capable of passing reducing equivalents to the active site clusters responsible for this reductive cleaving (**Figure 1.6**).[42] The only other significant source of reduced nitrogen on earth comes from the industrial Haber-Bosch process, which occurs at extreme temperatures and pressures in contrast to the ambient conditions at which metalloenzymes operate. The ubiquitous and necessary use of iron-sulfur clusters in electron transfer reactions is apparent, not only in the Fe-protein, but also in ferredoxins, and other homologues.[43] Nitrogenase can also facilitate the reduction of CO_2 to CO to hydrocarbons in the presence of ATP and a reductant.[44] It has been identified that this reduction to hydrocarbons is performed by the much simpler Fe_4S_4 cubane cluster of the nitrogenase Fe protein. The relevant redox states for this process have charges of +2, +1, and 0. It has been noted that the ‘super-reduced’ fully ferrous cluster is essential to driving the catalytic reduction of CO_2 and CO in the absence of ATP hydrolysis and protein-protein binding which has industrial significance for replacing current heterogenous surface catalysts (Fischer–Tropsch synthesis).[45]

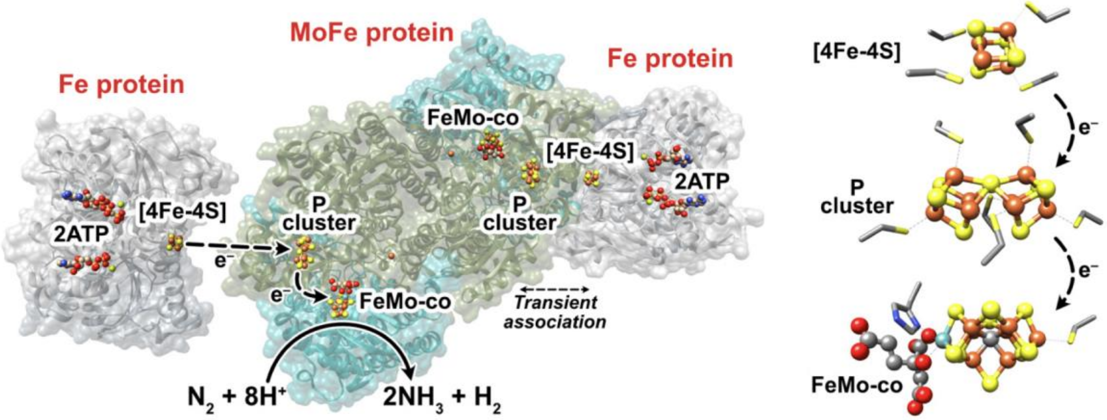

Figure 1.6 Representation of Mo-nitrogenase from *Azotobacter vinelandii*. The Fe protein is shown in gray and the MoFe protein is shown in cyan. Fe = rust, S = yellow, C = gray, N = blue, O = red, Mo = cyan, Mg = green. *Reproduced from [42] MDPI.*

The importance of the cubane cluster in biological chemistry has been known and with it an abundance of literature attempting to derive synthetic models for over 50 years. After the Fe-S cubane, ligated by four cysteine residues, was identified through X-ray studies as the long-sought “nonheme” iron center of the HiPIP in 1971[46] a synthetic model replicating the tetrahedral ligand structure using benzylthialoto was developed by Holm *et al.* in 1972.[47] It was not until 2005 that Holm synthetized the first fully ferrous Fe-S cubane, inspired by that of the Fe-protein of nitrogenase. This cyano-ligated, low-electron count, heterocubane was structurally similar to that of its biological inspiration, with the iron atoms moving closer to the center, but outside of the covalent bonding distance (2.68-2.69 Å).[48] The Mössbauer spectrum of this cluster exhibited 4 equivalent iron centers whereas that of nitrogenase cubane has a distinct Mössbauer signal exhibiting a 3:1 electronic distortion.[49] Later, Holm reported a more robust N-heterocyclic carbene (NHC)-stabilized cluster that first showed both a close structural and electronic match to that of the protein bound cluster.[50]

Tuning of cubane reduction potentials is achieved naturally by the proximity of the cofactors to neighboring dipoles or charges. Even the presence of negatively charged (carboxylates) and positively charged (ammonium) surface amino acids which solubilize the proteins can lower and raise the reduction potential over 400 mV.[51] Additional reduction potential tuning can be achieved via solvent accessibility, with cubanes near the surface of the protein having higher reduction potentials due to the shielding of negative charge by water's molecular dipole which can alternatively be limited within the hydrophobic interior of the protein (**Figure 1.7**). This high degree of electronic tuning, which controls the cubanes thermodynamics and kinetics, is what allows proteins to selectively and precisely control the flow of redox equivalents between proteins within the cell.[52] The tailorable synthetic environments that reticular chemistry provides could allow electronic tuning, similar to enzymes, to be achieved in the solid state.

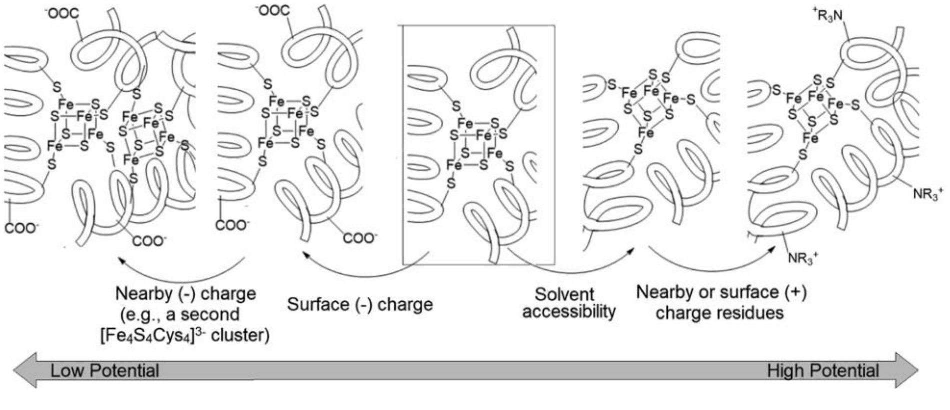

Figure 1.7 Cartoon illustration of a generic protein (center) containing Fe_4S_4 cubane cluster showing modifications used by Nature to tune reduction potential from low to high. *Adapted from Bigness, A.; Vaddypally, S.; Zdilla, M. J.; Mendoza-Cortes, J. L. Ubiquity of cubanes in bioinorganic relevant compounds. Coordination Chemistry Reviews 2022, 450, 214168, Copyright (2022), with permission from Elsevier.*

1.5 N-heterocyclic Carbenes

A carbene is a divalent, six-valence electron carbon. In the absence of significant stabilization, carbenes are inherently unstable and exist only as transient intermediates in organic reactions. The exceptional stability of *N*-heterocyclic carbenes (NHCs) have made them one of the most investigated ligands for transition metals for 25 years[53], but they were first described in 1968.[54, 55] It was not until 1988 that Betrand and colleagues showed that neighboring heteroatoms such as phosphorus and silicon considerably enhanced the carbene's stability.[56] Though it was the seminal X-ray structure of the first carbene, isolated using a remarkably stable and bulky nitrogen heterocycle, in 1991 by Arduengo et al. that conferred extensive interest into these remarkable structures (**Figure 1.8a**).[57] The high electronegativity of the adjacent nitrogen atoms inductively withdraws electron density from the non-bonding lone pair while their lone pairs mesomerically participate in π-electron donating with the empty p-orbital of C^2 (**Figure 1.8b**).[58, 59] The resultant electronic ground-state distribution for most NHCs is aptly described as an sp^2-hybridized lone pair, structurally favored by the bent geometry imparted from the cyclic structure, and an unoccupied p-orbital of C^2 leading to a highly nucleophilic C^2 with a high propensity for binding metal centers (**Figure 1.8c**).[60, 61] Evidence of this ground-state electronic structure is reflected in the C^2-N bond lengths of the free carbenes which fall between those of their imidazolium and C^2-saturated analogues indicating a partial double-bond character. The sterics of the N-substituents control the degree of kinetic protection. This can readily be seen in the self-dimerization that is observed with smaller substituents forming electron-rich olefins (the Wanzlick equilibrium).[62] Thermodynamic stability is enhanced by unsaturation in the cyclic backbone; with a 25 kcal mol^{-1}

difference predicted by isodesmic DFT calculations between imidazole and imidazolin.[63] Control over these nitrogen and backbone substituents provides considerable influence over the sterics and electronics of NHCs. Regulating these parameters is essential for the design of catalyst and linkers.[64]

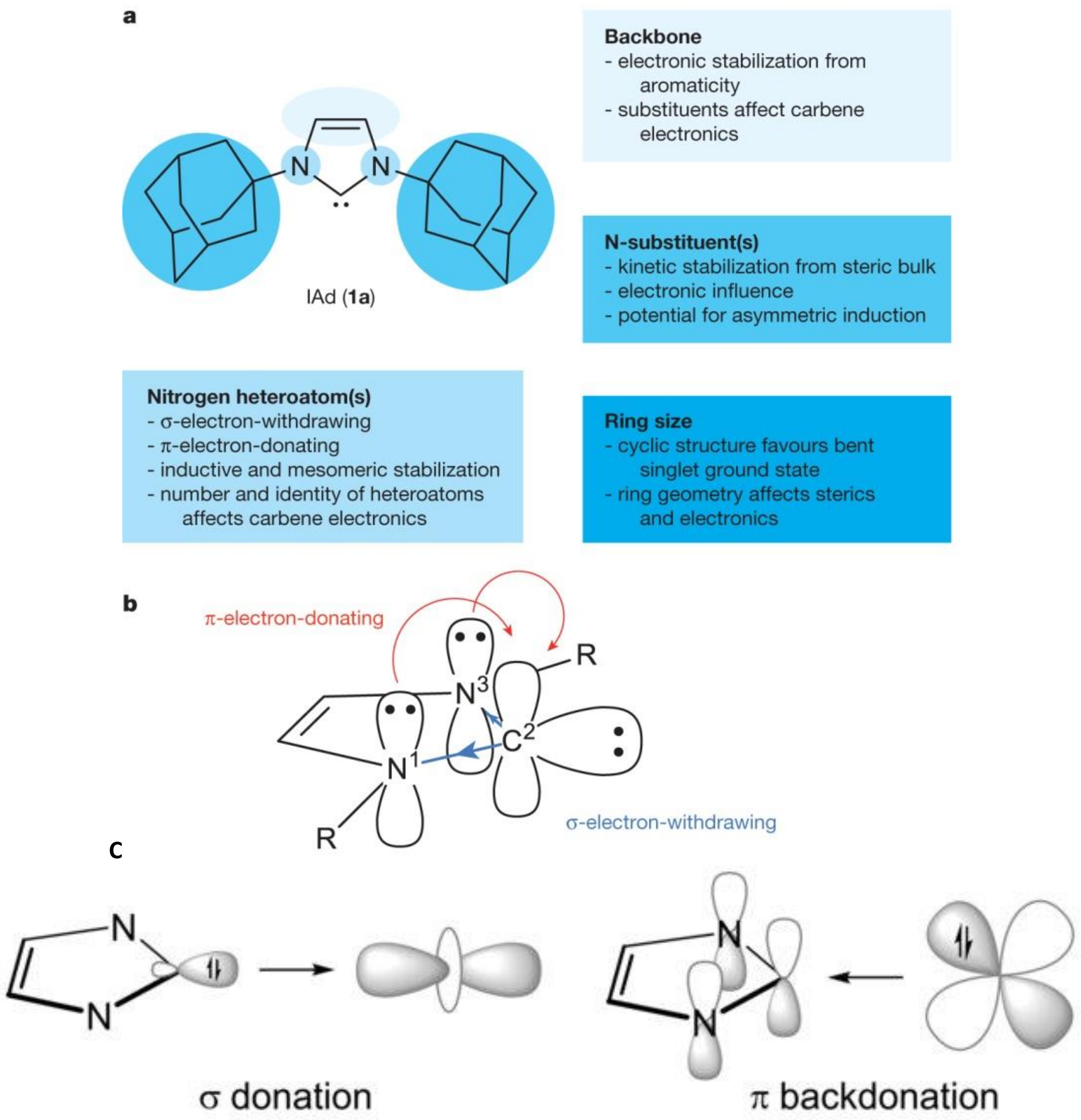

Figure 1.8 (a) structural features of first isolable NHC highlighting the structural influences on stability and reactivity. (b) ground-state structure of imidazol-2-ylidenes depicting the stabilizing σ-withdrawing and π-donating effects of the nitrogen heteroatoms. (c) Primary molecular orbitals involved in an NHC-M bond. *(a) and (b) adapted with permission from [59] Springer Nature. (c) Adapted with permission from [61] Copyright 2021 Wiley-VCH.*

1.6 Redox Flow Batteries

The ever-growing energy demands of the global population and the current solutions come with many accompanying environmental concerns. Especially with the increasingly intermittent and decentralized energy output of modern solutions, energy production and consumption are rarely in a natural equilibrium. Efficient large-scale energy storage that is both scalable and sustainable will be a cornerstone of any long-term solutions. There are many ways to store energy, but batteries dominate in a modern context, specifically electrochemical accumulators.[65] For example, the lithium-ion batteries in our phones or the lead-acid batteries in our cars. Such devices can store energy for long periods of time, are rechargeable, and have high energy densities. However, these traditional accumulators store energy in the electrodes themselves. This introduces inherent design limitations. Redox flow batteries (RFBs) are a promising electrochemical storage approach that decouples the location of the electrochemical reaction (electrodes) from the energy storage.[66] This is achieved by using soluble charge carriers (catholytes and anolytes) stored in an electrolytic solution which are pumped through the electrochemical cell (flow cell) during charge and discharge cycles (**Figure 1.9**). RFBs allow for the scaling of the peak power and the capacity independently.[67] The energy density of RFBs is often lower than that of accumulators, but their versatility and safety have made them prime candidates for stationary grid-scale energy storage.

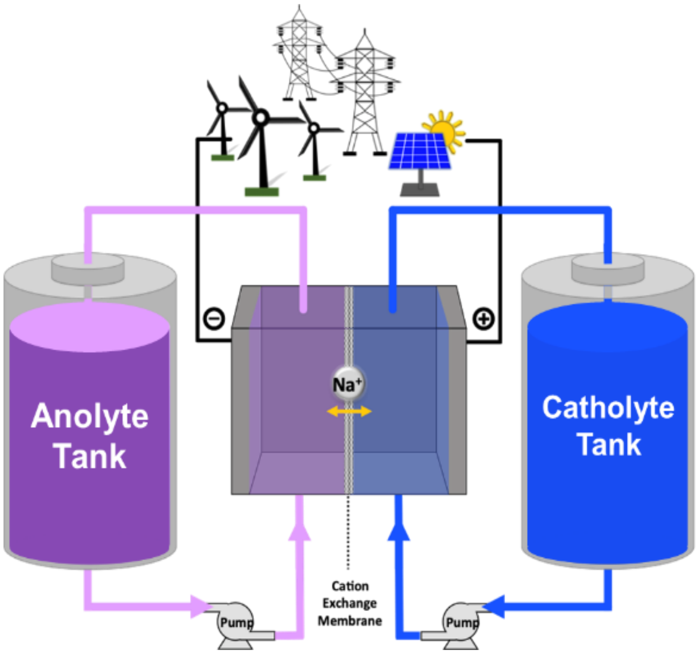

Figure 1.9 Schematic of a conventional redox flow battery.

The most commercially advanced RFB technology is based on vanadium salt electrolytes ($300/kWh). A key to their success is stability, with modern RFB lifetimes of up to 20 years.[68] However, vanadium is inherently toxic and comes with a high acquisition cost due to material scarcity and the necessity of costly ion exchange membranes. Organic electrolytes provide a promising alternative due to their abundance and tailorability. Their solubilities, redox potentials, and number of electrons transferred can be synthetically tailored. Additionally, with inherently larger sizes, organics can take advantage of size-selective separation rather than the costly ion exchange membranes. The leading problems with most organic electrolytes are their inferior long-term cycling stability, necessary for battery lifetime and ultimately cost. In addition, poor aqueous solubility can result in low energy density and in effect low efficiency. Organic constituents often have capacity fade rates exceeding 0.1%/day at adequate concentrations primarily due to decomposition and to a lesser extent membrane permeation. Non-aqueous media typically enhance both solubility and radical stability of organic electrolytes while providing a larger electrochemical window to work within, but at a detriment to sustainability, conductivity, safety, and cost.

Lithium-ion 100 MW batteries ($162/kWh) are the current baseline set by the DOE being used for long- and short-term storage initiatives in 2021. Economic analysis of an aqueous RFB system with a 1.5 V window estimates that an active solution with a solubility of ~1-2 mol/L would need to cost roughly $0.75 per mole of transferable electrons to achieve $120/kWh.[23] Aqueous systems benefit substantially from very cheap solvent and electrolytes leaving almost all the cost available to the active species. Nonetheless, this is a very steep goal due to the low cost of electricity in the U.S. and the small voltage window of water. These factors make the targets nearly unobtainable for most metal ions, due to raw material cost. Lost electrolyte can often be periodically replaced, but this must be factored into the lifetime cost. The acquisition cost of organic species can largely be brought down through the scale of production. Currently, the responsibility for lowering lifetime cost is up to researchers designing stable active species.

1.7 Radialenes

Of the few organic compounds that can operate as efficient redox couples under aqueous conditions, anthraquinone[69], methyl viologen derivatives[70-72], and phenazine[73] have considerable progress as anolytes. There are only a few organic redox-active moieties possessing redox couples with an appropriate free energy change to be considered for aqueous positive cell reactions including amine (indigo carmine), aminoxyl (TEMPO and N-hydroxyphthalimide), carbonyl (quinones and biphenol), Aza-aromatic, ether and thioether (thian-threne).[74, 75] These are typically small molecules (<500 Da) with a redox potential between 0.5-1.0 V vs. SHE. The reduction or oxidation of the closed shell molecule generates the radical species for which a majority are centered on electronegative heteroatoms O, S, or N. Radical stabilization is typically achieved through delocalization and conjugation realized by means of cyclic and conjugated structures. Many of which have multiple heteroatoms allowing for two electron processes to change the total bond number and reform a stable close shell system.[76] The reorganization energy of organic redox couples is usually low compared to solvated metal ions. This means they typically have redox kinetics orders of magnitude faster than metal ions resulting in improved efficiency and accessible power density. A recent computational investigation by Schröder *et. al.* showed that although phenazine anolytes are approaching a competitive cost with current vanadium RFBs, the current organic catholytes (posolytes) are far from meeting the current standard (**Figure 1.10**).[75]

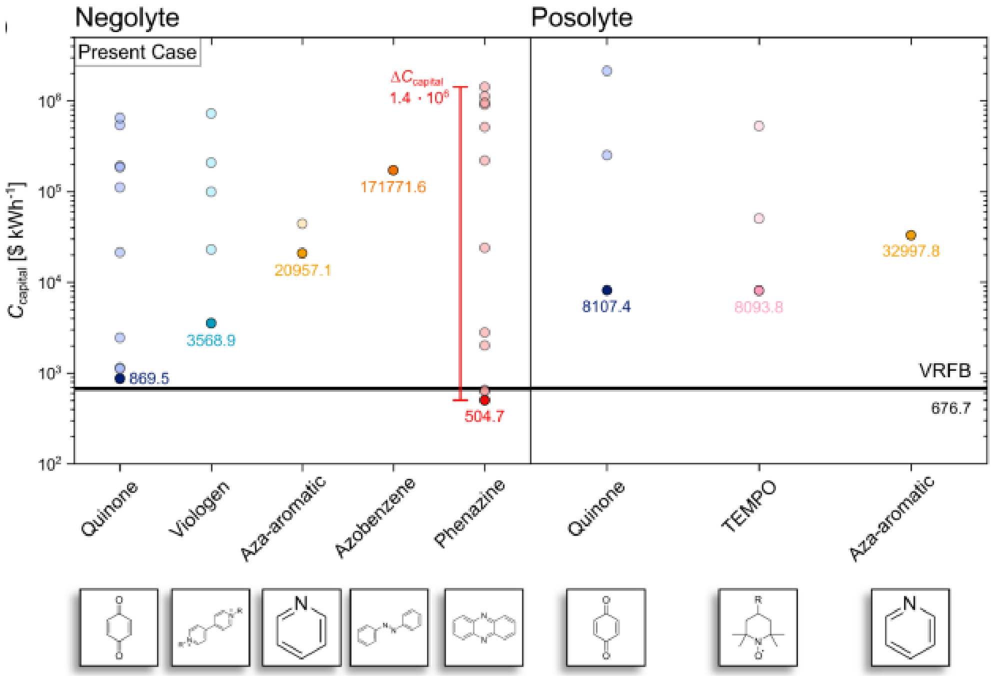

Figure 1.10 A computational benchmark of lifetime cost for organic aqueous RFB electrolytes highlighting the promise of these materials to surpass current vanadium RFBs, but with catholytes trailing behind anolytes. *Adapted from [75].*

Redox potentials of organic molecules are both functions of their chemical structure and environment. Functional group interactions, hydrogen bonding, and protonation all can alter the reduction potential. A principal means of synthetic control comes down to controlling the electron density in the vicinity of the redox center. Typically, electron-donating groups (e.g. alky, amine, hydroxyl) reduce the redox potential whereas electron-withdrawing groups (e.g. cyano, carboxyl, sulfonate) increase the redox potential. High redox potentials within the electrochemical window are favorable, but the high electron affinity of high potential, oxidized molecules make them prone to nucleophilic attack like that of hydroxide ions and subsequent decomposition. The thermodynamic decomposition of water by means of hydrogen and oxygen evolution reactions occurs between 0.00 V and 1.23 V on the pH independent RHE scale, imposing a fundamental limit on the aqueous cell voltage. Though the inherently sluggish kinetics of oxygen evolution have, in practice, allowed the positive electrode to push values of up to 1.6 V vs RHE at which point carbon electrode oxidation becomes an issue.[77]

TEMPO-derivatives are the most well studied and successful neutral pH, aqueous catholytes. In pH neutral water the standard potential of water oxidation is around 0.817 V vs. SHE for which TEMPO's redox potential is well suited, 0.8-1.0 V vs. SHE. TEMPO derivates have been shown to have capacity fades <1% per day and with solubility and kinetics well above that of vanadium. Even though synthetic control of TEMPO substituents provides excellent control over the solubility there is minimal control of the potential due to the isolation of the redox center. There is a continued push to investigate less studied, high potential, aqueous redox active molecules to expand the design space.[74] In this vein, the Bejger lab began investigating the largely unexplored hexa-substituted [3]radialenes in 2018 as a RFB catholyte.

Hexa-cyano[3]radialene disodium dianion and radical showed promise being stable in air and neutral water up 180 °C with a redox potential of 0.68 V vs. SHE (**Figure 1.11**).[78] Unfortunately, its poor aqueous solubility makes it unsuitable for an aqueous RFB. Less withdrawing hexa-aryl substituents showed nonaqueous stabilization of the first and second oxidation state with redox potential reductions, compared to hexa-cyano, of up to 2.0 V.[79] The hexa-substituted [3]radialene provides an opportunity for modulating both the redox and solubility properties beyond that of most catholytes, with six substitutional positions that can be modified asymmetrically.[75] In 2020, Turner prepared a series of asymmetric, ester-substituted, [3]radialenes through step-wise synthesis. The compounds exhibit enhanced solubility and stability for the diester-tetracyano[3]radialene catholyte (**Figure 1.11**).[80] These ester-substituted systems also presented unique and unexplained dimerization patterns that were solvent, counter-ion, concertation, and temperature dependent. Thus, there is a need for computational investigation to understand the radical dimerization and to rapidly screen a vast landscape of substituent patterns.

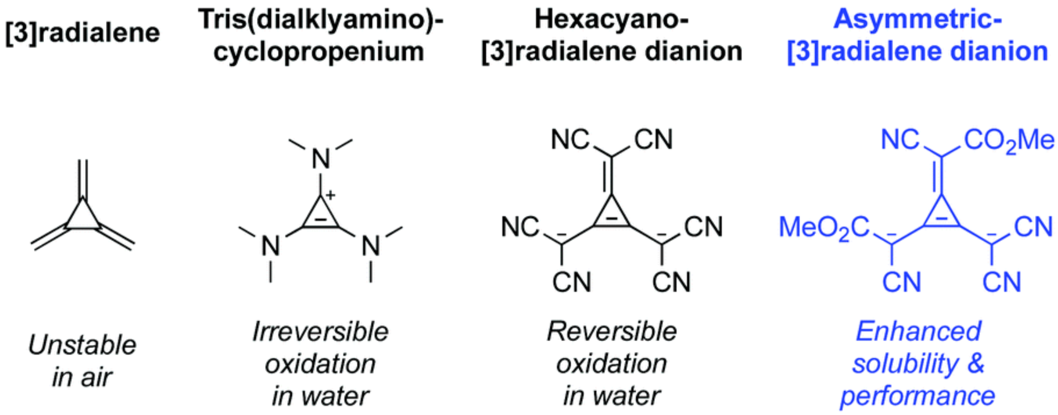

Figure 1.11 Examples of [3]radialene compounds and their electrochemical properties in aqueous solutions. *Adapted from [80].*

1.8 Dissertation Summary

Although most MOFs use clusters as metal-containing SBUs, they are almost always formed *in situ*, precluding *ex situ* tuning or the integration of many preformed clusters. Consequently, charge-delocalized SBUs suitable for electron conduction remain unexplored. Charge-delocalized, metal-chalcogenide superatoms are the foundation of the metalloenzymes responsible for some of nature’s most consequential catalytic reactions. The lower thermal stability of coordination polymers, in comparison to the industrially relevant and covalently bonded zeolites, provides a strong incentive for developing them as enzyme mimics for which the integration of the fully reduced, electron conducting Fe_4S_4 cubane would be an enormous step. Tetrahedral SBUs are staples in the design of 3D MOFs and ZIFs for which the cubane’s coordination symmetry is ideally suited. Integrating these clusters into porous, crystalline frameworks would provide a high level of environmental control, like that of enzymes, over these clusters while simultaneously improving their stability. The seminal work of Mak *et al.* highlighted this very principle with silver chalcogenide clusters coordinately linked and spatially separated via modulating the coordination shell by replacing coordinated CH_3CN ligands with linear bridging ligand 4,4′-bipyridine. In practice their yields were much improved through a one-pot synthesis with the cluster being formed in situ.[81] But this control over spatial separation and orientation dramatically improved the clusters stability and luminescence.

The phosphine stabilized Fe_4S_4 core, when reduced to the fully ferrous oxidation state, consistently results in core aggregation producing di/tetra-cubanes due to phosphine dissociation. The ability of NHC's to stabilize the fully ferrous Fe_4S_4 cubane was pivotal in our selection of a linear reticular linker for synthetic investigation. The metal-chalcogenide cubane motif can be accessed with many different metal and bridging ligand atoms. Along with the turnability of the NHC linker, these structures could provide access to many isoreticular materials with a large degree of synthetic control. Our seminal research aim focused on the isostructural cobalt cubane as a tetrahedral SBU, due to the proclivity of the phosphine stabilized iron cubane to aggregate. Chapter 2 details the development of the first main chain organometallic polymer (MCOP) to use Janus NHC linkers and superatomic nodes. Further, we show the modularity of the carbene ligand highlighting a potential mechanism for achieving MCOPs with high crystallinity.

Chapter 3 builds upon the foundation of chapter 2 by preparing the Fe_4S_4 MCOP. An additional focus is the formation of superatomic ionic solids from neutral electron donating, M_4S_4 (M = Fe, Co) cubanes and electron accepting fullerene. It was hypothesized that C_{60} could be used to ionically fill the open space of the MCOP, effectively stabilizing the structure. It was then realized that such superatomic ion pairs were surprisingly soluble. This allows them to be used in the formation of MCOPs with particularly enhanced electrical conductivities. This section also outlines some of our related pursuits of these superatomic polymers using isocyanide ligands and ZIF-inspired analogues.

The final chapter is directed to our research on hexa-substituted [3]radialenes as RFB catholytes. The stepwise synthesis allowing for substitution of one methylene nitrile group at a time, as reported by Fukunaga[33,34], makes this molecule an ideal candidate for molecular engineering. Yet the extremely large number of possible molecules that can be synthesized comes as a double-edged sword, as exploring the synthetic landscape is expensive and time consuming. Thus, there are many possible pitfalls due to the stringent requirements to be an effective RFB active species. Moreover, many hexa-cyano [3]radialene radical derivatives have known dimerization and stability challenges that are difficult to predict.[23] Experimentation for discovering aqueous electroactive molecules is already slowed by the trial and error of determining adequate synthetic conditions and purification procedures. The Bejger Lab has a history of expertise in the synthesis of redox active materials, but [3]radialenes have proved to be particularly challenging due to their seemingly unpredictable radical ground states. In parallel with wet chemistry efforts, we will review the low-cost computational screening techniques to accelerate the discovery of new radialenes as aqueous RFB catholytes and predict dimerization.

CHAPTER 2: MAIN-CHAIN ORGANOMETALLIC POLYMERS

Reproduced from *Chem. Commun*., 2022, 58, 4885-4888 with permission from the Royal Society of Chemistry.

2.1 Introduction

Rigid, non-chelating, poly-N-heterocyclic carbene (NHC) ligands are emerging building blocks in the assembly of functional main-chain organometallic polymers (MCOPs).[82, 83] Structurally, such materials consist of bridging, poly-NHC organic linkers and single transition metal ions that serve as branching points of extension. So far, the dimensionality of this class of polymer has been dictated by the topicity and geometry of the poly-NHC linker. Specifically, one,[84, 85] two,[86-89] and three-dimensional (3D)[90, 91] MCOPs have all been reported using various poly-NHC ligands and single-metal atoms including palladium,[84, 87, 90, 92] platinum,[92] nickel,[92] iridium,[85, 91] and gold.[86, 88, 89] Utilizing polynuclear complexes or ensembles of multiple metal atoms could afford further control over dimensionality and polymer structure. However, the investigation of NHC-based MCOPs comprising molecular clusters remains an open issue. This is surprising for several reasons. For instance, there are numerous known NHC-stabilized metal cluster compounds, including those containing metal-carbonyl,[93] noble metal,[94-96] metal-chalcogenide,[50, 97] and metal-halide[98] cluster-cores. Thus, similar synthetic protocols used to prepare these discrete clusters can be applied to incorporate them into poly-NHC MCOPs. Additionally, molecular clusters are attractive from a structural standpoint. They are well-defined and can be prepared in a variety of sizes and geometries.[99-102] In fact, the abstraction of clusters as polyhedral nodes is central to the field of reticular chemistry and gave rise to the first crystalline metal organic frameworks (MOFs).[103] Substituting single metal atoms for clusters could, therefore, lead to crystalline NHC-MCOPs. This is significant, as all known NHC-MCOPs have all been isolated as amorphous solids. Finally, molecular cluster compounds have rich catalytic[104, 105] photophysical,[106, 107] magnetic,[108, 109] and redox[110-112] properties beyond what single transition metals can offer. Consequently, a diverse new class of functional MCOPs can be envisioned from the coupling of clusters with poly-NHC linkers.

Our group is using metal chalcogenide clusters as building blocks for redox active MOF-hybrids.[113, 114] This is accomplished using pre-assembled clusters stabilized with bifunctional phosphine ligands. Ancillary sites on the phosphines, and periphery of the cluster, then undergo further assembly in the presence of metal cations. However, diphosphine ligands are nonlinear linkers and produce distorted frameworks with bent connections between building units. The use of phosphine linkers thus makes the prediction of the final structure challenging, preventing the reticular design principles of MOF synthesis from being applied. Other organic ligands have been used to crosslink metal-chalcogenide clusters but suffer from similar issues. For example, coordination polymers assembled from benzenedithiolate ligands and both $[Fe_4S_4]^{2+}$ and $[Mo_3S_7]^{4+}$ clusters, respectively, have recently been reported.[32, 115] However, these polymers are 1D chains, presumably due to the flexibility and bent nature of the metal–sulfur bond between the bridging ligands and the cluster cores. Rigid, linear linkers are therefore essential to develop metal-chalcogenide clusters as building blocks in reticular chemistry. Here, we report that aromatic-fused, Janus di-NHC ligands[82] are efficient bridging units for the assembly of Co_4S_4 clusters into redox active MCOPs.

2.2 Experimental

2.2.1 Chemicals

All manipulations were performed under an inert atmosphere of dry N_2 using a Schlenk line or MBraun UniLab Pro glovebox unless otherwise noted. Tetrahydrofuran (THF), toluene, dichloromethane (DCM), hexane, and diethyl ether were purged with N_2 and dried on an MB-SPS solvent purification system from MBraun. Anhydrous acetonitrile (99.8%, Aldrich), anhydrous benzene (Drisolve), anhydrous 1,4-dioxane (99.8%, Alfa Aesar) were freeze-pump-thawed 3-4x. NaH 60% in mineral oil (Aldrich) for imidazolium deprotonation was washed thoroughly over a medium fritted filter funnel with hexane under a N_2 atmosphere and dried under vacuum. All other chemicals were purchased from commercial sources and used as received, including N,N-dimethylformamide anhydrous/under argon (99.8%, Alfa Aesar), 1,2,4,5-benzene tetramine tetrahydrochloride (95%, Aldrich), formic acid (96%, Alfa Aesar), hydrochloric acid (Macron Fine Chemicals), 2-bromopropane (99%, TCI), bromoethane (98% Alfa Aesar), sodium carbonate monohydrate (99.5%, Alfa Aesar), anhydrous potassium carbonate (99%, EMD), benzimidazole (98%, Acros Organics), cobalt (II) chloride anhydrous (99.7%, Alfa Aesar), triisopropylphosphine (98%, Alfa Aesar), bis(trimethylsilyl)-sulfide (95%, Acros Organics), KOtBu (potassium tert-butoxide, 98%, Aldrich), and potassium chunks in mineral oil (98%, Alfa Aesar).

2.2.2 Instrumentation

Nuclear Magnetic Resonance (NMR) Spectroscopy

NMR spectra were obtained on a Jeol ECA-500 NMR for ^{1}H (500 MHz), ^{13}C (125 MHz), and ^{31}P (202 MHz). NMR samples were prepared using deuterated solvents purchased from Cambridge Isotope Laboratories >95% and sealed by parafilm or a J-Young needle valve.

Thermogravimetric Analysis (TGA)

Thermogravimetric analysis was performed on vacuum dried solid in a platinum pan using a Mettler Toledo TGA/SDTA851e continuously purged with compressed N_2.

Electrochemistry

All electrochemical measurements were obtained on a Gamry 1000E potentiostat and were recorded on Gamry Framework Software (Version 7.02). Analysis of the data was done using S5 Gamry Echem Analyst (Version 7.02). Measurements were performed with a three-electrode setup with a working glassy carbon electrode (3.0 mm), a platinum wire counter electrode, and a platinum wire as a pseudo-reference electrode. The solid polymer was physically absorbed onto the surface of the glassy carbon electrode while still wet with THF. Approximately 2 mg of wet polymer covering ½ of the surface of the grassy carbon electrode were loaded for each measurement. All measurements were collected inside the glovebox under a dinitrogen atmosphere. Ferrocene was used post analytically to reference voltages. CV scans taken with modified electrodes did not exhibit redox activity when the adsorbed solid is physically removed. Additionally, no oxidation or reduction events could be measured (with a clean working electrode) in the residual solution after the polymer-modified electrode had been submerged for an hour.

Electronic Absorption Spectroscopy

A Cary 300 Bio UV-Visible Spectrometer running Scan v1.00(6) was used to collect the UV-vis spectra with solutions of THF inside of sealed quartz cuvettes to maintain an air free atmosphere. The dried polymer was run as a powdered solid, sealed between two slides, and suspended in bSi-201 quick cure epoxy to prevent oxidation.

Scanning Electron Microscopy and Energy Dispersive X-ray Spectroscopy

Scanning electron micrographs were obtained on a JEOL JSM-6460LV SEM instrument using a 5-15kV accelerating voltage while collecting data through the SEM Control User Interface (Version 6.21). Energy dispersive X-ray spectrographs were taken using the built in EDAX and worked up using the APEX software. SEM samples were dried under vacuum and placed on a copper or carbon tape background with a 60 second air exposure while being loaded. During this exposure, samples would occasionally produce smoke from an exothermic reaction.

Single Crystal X-ray Diffraction

Single Crystal X-ray diffraction was performed using an Oxford Diffraction Gemini A Ultra SCXRD. Samples were dried for 30 min by vacuum and suspended in Nujol mineral oil before being transferred to the sampling stage and mounted on loops. (Additional details in section 2.5.13)

X-ray Photoelectron Spectroscopy

X-ray Photoelectron Spectroscopy was collected using a Thermo Scientific ESCALAB Xi with a twin crystal monochromatic Al Kα source (500 μm), and a pass energy of 20.0 eV, with a spot size of 200 μm. Samples were stored in an inert atmosphere and transferred rapidly to the loading chamber of the XPS after mounting the sample. To prevent charging of the surface, all samples were probed in the presence of a low energy electron flood gun. Charging can lead to shifting and distortion of the XPS spectra, so a low energy electron flood gun was used to limit charging.

Powder X-ray Diffraction

Powder X-ray diffraction patterns were obtained from 11-BM APS Synchrotron Beamline (Bending Magnet Source) at the Argonne National Laboratory (Lemont, Il, USA). X-ray samples were dried under vacuum, ground by mortar and pestle, and packed into a 1.105 mm outer diameter, 0.1 mm wall Kapton capillary inside a nitrogen glovebox. The capillary ends were then sealed with bSi-201 quick cure epoxy and allowed to cure for at least 24 hours.

High resolution synchrotron powder diffraction data were collected using beamline 11- BM at the Advanced Photon Source (APS), Argonne National Laboratory using an average wavelength of $\lambda = 0.4581$ Å. Discrete detectors covering an angular range from 0.5 to 50° 2θ, with data points collected every 0.001º 2θ and scan speed of 0.01º/s. The predicted structure was generated by forming a diamond cubic crystal structure with each Co_4S_4 unit representing a single lattice point and a lattice constant of $a = 29.56$ Å as based upon the SCXRD data for the free carbene and model cluster. It should be noted that this structure omits the alkyl groups and assumes a carbene-cobalt bond length and core geometry as found in the model cluster.

Surface Area Analysis

Surface area was estimated by BET isotherms using a Quantachrome Instruments NOVA 2200e Surface Area & Pore Size Analyzer supplied by compressed N2. Samples were dried under vacuum for 24 hours with a potential air exposure while the BET tube was being transferred to the degassing line.

2.2.3 Synthesis

Synthesis of 1,3-Dihydro-1,3-bisisopropyl-2H-benzimidazol-2-ylidene (Pri2NHCBz) **(3)**. The free carbene was prepared using a modified literature preparation.[116] KOtBu (208 mg, 1.85 mmol) was placed in a 20 mL vial inside the glovebox and dissolved in THF (6 mL). 1,3-Diisopropylbenzimidazolium bromide[117] (526 mg, 1.85 mmol) was added to the vial and the suspension was stirred for one day at room temperature. The suspension was filtered to yield a yellow solution, which was dried in vacuo to give free carbene **3**, as confirmed by ^{1}H NMR, as an off-white solid. Yield 333 mg (88%).

Synthesis of biscarbene **(4)**. 1,1’,3,3-Tetra-isopropyl-5,5’-bisbenzimidazolium bromide was first prepared following a modified procedure.[118] Briefly, the reported preparation yielded a product with an 85% purity (as measured via ^{1}H-NMR). The reaction was repeated three times on the resulting product of precursory reactions to achieve a 98% purity of an overall 25% yield. Solid product was washed with chloroform to remove any dimethyl amine, formed in situ from DMF, that formed during the reaction. The free biscarbene was then prepared following a modified procedure by Bielawski and coworkers.[84] The imidazolium dibromide (100 mg, 0.20 mmol), NaH (12.2 mg, 0.51 mmol), and KOtBu (2 mg, 18 μmol) were suspended in THF or benzene (5 mL) and stirred for 2 days. The resulting suspension was syringe filtered and dried in vacuo producing a yellow/tan solid product. A concentrated solution of the biscarbene in THF layered with hexanes produced X-ray quality single crystals. Yield: 25mg (37%). (Note: freeze drying from benzene produces a yellow "cotton candy" like solid). ^{1}H NMR (500 MHz, C_6D_6) δ 7.00 (2 H, s, Ar-H), 4.48 (4 H, sept, N-CH), 1.65 (24 H, d, CH-CH_3) ppm. ^{13}C NMR (125 MHz, C_6D_6) δ 225.07 (N-C-N), 131.81 (Ar-C_{ipso}), 90.06 (Ar-C), 49.51 (N-CH), 23.46 (CH-CH_3) ppm.

*Synthesis of $Co_4S_4(Pr^i{}_2NHCBz)_4$ (**2**).* $Co_4S_4(PPr^i{}_3)_4$ (**1**)[119] (251 mg, 0.25 mmol) and $Pr^i{}_2$NHCBz (3) (253 mg, 1.5 mmol) were placed in a 25 mL Schlenk flask and dissolved in THF (10 mL). The dark yellow-green solution was stirred at 60 ºC under an N_2 atmosphere for two days and then refluxed at 78 ºC for an additional two days. The resulting dark red solution was evaporated under vacuum to a solid film, dissolved in ether (2mL), syringe-filtered, and placed in a 20 mL vial. After three days sealed and undisturbed, X-ray quality crystals formed and were gently washed with chilled ether (4 x 3 mL). Yield: 296 mg (quantitative) (single crystal yield 30%). ^{1}H NMR (500 MHz, C_6D_6) δ 12.54 (12 H, s (br)), 6.66 (2H, s), 6.45 (2H, s) ppm. Anal. Calc. for $Co_4S_4N_8C_{52}H_{72}$: C 53.93%, H 6.63%, N 8. 98%. Found: C 49.60%, H 6.22%, N 8.58%.

Synthesis of Co_4S_4-MCOP. Cluster **1** (30.8 mg, 0.0306 mmol) and biscarbene **4** (25.0 mg, 0.0766 mmol) were weighed into two, separate 20 mL vials and each dissolved in benzene (2.5 mL). The solutions were then transferred and mixed into a 15 mL Chemglass pressure vessel and sealed under a N_2 atmosphere. The vessel was placed in an oven at 100 °C. After 2-5 days the resulting purple solid was separated by centrifugation and washed with THF (6 × 1 mL) inside the glovebox. Subsequent drying under vacuum produced a black solid with substantially less volume. Yield: 14 mg (45%). The reaction has also been repeated using toluene, dioxane, and THF with similar yields/products (~20-50%).

We also prepared a less sterically hindered tetrakis-N-ethyl-biscarbene in order to probe the steric effect of the linker on crystallinity. Polymers were synthesized using this smaller linker under the same conditions listed above. The Co_4S_4-MCOP-ET solids were similar in color, morphology, and composition via SEM and EDS. Structurally, the PXRD pattern of this ethyl analog did not differ from that of Co_4S_4-MCOP. Fabricated electrodes using the polymer made with tetrakis-N-ethyl-biscarbene linkers exhibit one oxidation at a similar potential. See Section XIII below for PXRD, SEM, EDS, and CV of this derivative.

Depolymerization of Co_4S_4-MCOP. A suspension of polymer (13.8 mg) in deuterated benzene (1.2 mL) was mixed with a solution of free carbene $Pr^i_2NHCMe_2$ (48 mg, ~20 equiv., 1.2 mL) in a 2-dram vial. The solution was stirred for two days inside the glovebox on a hotplate at 50 ºC. During this time, the majority of the solid dissolved and the solution turned dark, reddish brown. The solution was allowed to sit for several hours before an aliquot (1 mL) was taken from the top of the reaction mixture and analyzed by NMR.

2.3 Results and Discussion

The synthetic methodology to prepare Co_4S_4-MCOP is based on a report by Holm and coworkers that the phosphine ligated cluster $[Co_4S_4(PPr^i_3)_4]$ (**1**) undergoes high yielding, global ligand exchange in the presence of mono-NHC, 1,3-diisopropyl-4,5-dimethylimidazol-2-ylidene ($Pr^i_2NHCMe_2$).[119] This conversion can be completed in 12 hours with heating to yield the discrete cluster $Co_4S_4(Pr^i_2NHCMe_2)_4$. We prepared a benzo-bis-imidazolylidene (**4**) with isopropyl "wingtips" to match the steric profile of $Pr^i_2NHCMe_2$ using a modified prep reported by Bielawski.[120] The free biscarbene **4** is planar based on single-crystal X-ray diffraction (SCXRD) analysis (**Figure S1**). The flat, rigid nature of **4** coupled with the tetrahedral cluster core of **1** compelled us to combine the two building blocks and study their compatibility (**Figure 2.1**). Co_4S_4-MCOP is obtained as a purple solid when **1** and **4** are heated in solutions of benzene or toluene at 100 °C for 12 hours (**Figure S3**).

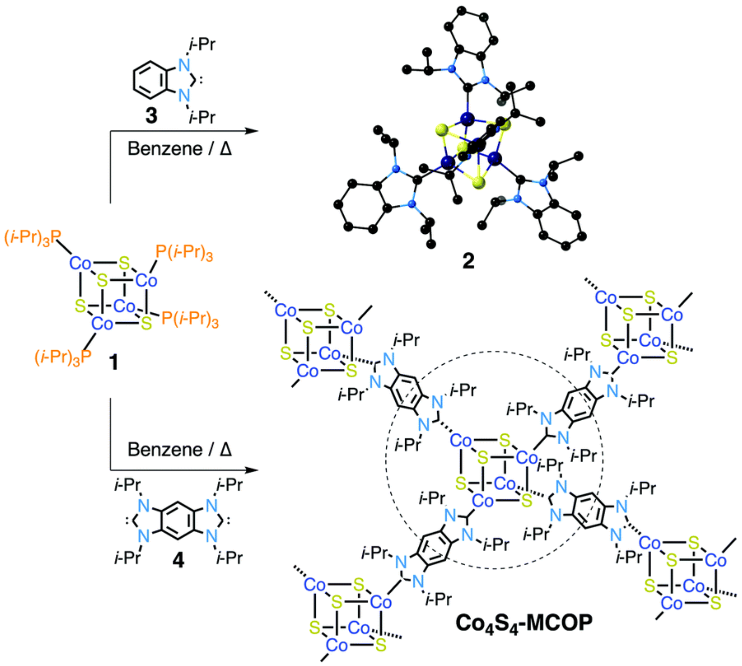

Figure 2.1 Synthesis of [$Co_4S_4(Pr^i{}_2NHCBz)_4$] (**2**) and Co_4S_4-MCOP. Single crystal X-ray structure of **2**. Hydrogen atoms omitted.

Scanning electron microscopy (SEM) and energy dispersive spectroscopy (EDS) were used to analyze Co_4S_4-MCOP. SEM micrographs of the dried polymer show the material to be non-uniform in size with an irregular, foam-like morphology (**Figure S3**). The EDS spectra confirm the distribution of Co, S, N, and C throughout the solid (**Figure S3**). Trace amounts of phosphorus were also observed in some scans at the margin of the detection limit. We ascribe this intermittent phosphorus signal to residual phosphine, which could either be trapped inside the solid or still bound to a fraction of the Co_4S_4 clusters.

A zero-dimensional, molecular analog to Co_4S_4-MCOP was also prepared from a comparable, benzoannulated mono-NHC ligand, $Pr^i{}_2$NHCBz (**3**) (**Figure 2.1**). SCXRD analysis of [$Co_4S_4(Pr^i{}_2NHCBz)_4$] (**2**) confirmed the tetrahedral nature of the Co_4 core and the coordination of four NHC ligands around the cubane unit. This nanocluster serves as a representative fragment of Co_4S_4-MCOP and was used for spectroscopic comparison to further characterize the polymeric material.

Evidence for the polymerization was first obtained via ^{1}H-nuclear magnetic resonance (NMR) spectroscopic studies. Specifically, when **1** and **4** were heated in C_6D_6 and monitored via NMR we observed a steady attenuation of the phosphine methine proton signal at 14.75 ppm. Concurrently, a new peak between 12 and 13.5 ppm emerged (**Figure S5**). This broad, new singlet matches closely to the position of the methyl protons on the discrete model cluster **2** and its appearance signifies that phosphine–NHC exchange is occurring. Full ligand substitution, however, cannot be monitored as the insoluble MCOP begins to form over time. ^{31}P-NMR spectroscopy confirmed the formation of free phosphine under the same conditions (**Figure S7**). This is in accord with the biscarbene **4** effectively displacing the phosphine ligands of **1**. Unfortunately, the paramagnetic nature of both **2** and Co_4S_4-MCOP precluded their analysis via solid-state ^{13}C-spectroscopy (**Figure S8**). Infrared (IR) spectroscopy was also performed to analyze the polymer (**Figure S9**). The IR spectrum of Co_4S_4-MCOP contains two signals of medium intensity at 1679 and 1704 cm^{-1}, respectively. We attribute the absorbances at these frequencies to C=N stretching, due to the presence of the biscarbene linkers.[121] The IR spectra of cluster **2** and free biscarbene **4** also contain distinct signals in this region at 1694 and 1668 cm^{-1}, respectively. The presence of two, different C=N stretches in the polymer may be due to a mixture of free and bound **4** or sites of monotopic coordination.

X-ray photoelectron spectroscopy (XPS) measurements were collected on Co_4S_4-MCOP, as well as clusters **1** and **2**, to compare their elemental composition and surface valence states (**Figure S11**). All three samples are air sensitive and display similar oxidized cobalt and sulfur profiles upon exposure to atmosphere with characteristic peaks for the Co2+ oxidation state, 802.5 and 786.1 eV, and an Sp2 peak at 161.9 eV that is indicative of a metal sulfide bond. A second sulfur peak is also observed at 166 eV, which we assign to an oxidized sulfur species (SO_x^{n-}), based on the XPS of related Co–S based solids.[122] The high-resolution XPS spectra of both Co_4S_4-MCOP and **2** show the nitrogen N1s peak at approximately 400 eV. The atomic proportion of Co : S : N in cluster **2** is 5.7 : 4.0 : 9.7, while Co_4S_4-MCOP has an atomic ratio of 4.6 : 3.8 : 10.7 for Co : S : N. Finally, we observed a minor quantity of phosphorus in the XPS spectrum of Co_4S_4-MCOP with a low signal to noise ratio. This residual phosphorus is consonant with the trace phosphorus periodically observed during EDS measurements.

The powder X-ray diffraction (PXRD) pattern of the polymer exhibits features centered around 2.25°, 5.7°, and 13.8° 2θ (**Figure 2.2a**). The broad diffraction peaks are in agreement with the morphology observed via SEM and are characteristic of a disordered solid with structural defects. Observation of diffraction peaks is particularly noteworthy, as all reported NHC-MCOPs are amorphous with no measurable PXRD patterns. The small number of peaks in the experimental PXRD, however, prevent assignment of an exact structure with high certainty. Nevertheless, a theoretical unit cell of Co_4S_4-MCOP assuming complete crosslinking was modeled and its PXRD pattern was simulated for comparison. The calculated pattern exhibits a number of sharp peaks clustered around 2.5° 2-theta. The center of this grouping is at a lower angle than the largest broad feature of the polymer pattern. Acknowledging the uncertainty in bond lengths of the modeled structure and potential distortions of the synthesized framework it is still possible that the Co_4S_4-MCOP may have a similar 3D, diamond structure.

The UV-visible absorption spectrum of Co_4S_4-MCOP has a broad peak centered at 503 nm (**Figure 2.2b**) and a strong absorbance below 350 nm. The optical band gap of Co_4S_4-MCOP was calculated from the low energy transition to be 1.68 eV. In comparison, the spectrum of cluster 1 is less well-defined and has only one peak below 300 nm (**Figure 2.2b**). The absorbance profile of the polymer more resembles that of **2** dissolved in THF, with two distinct absorbance peaks (**Figure 2.2b**).

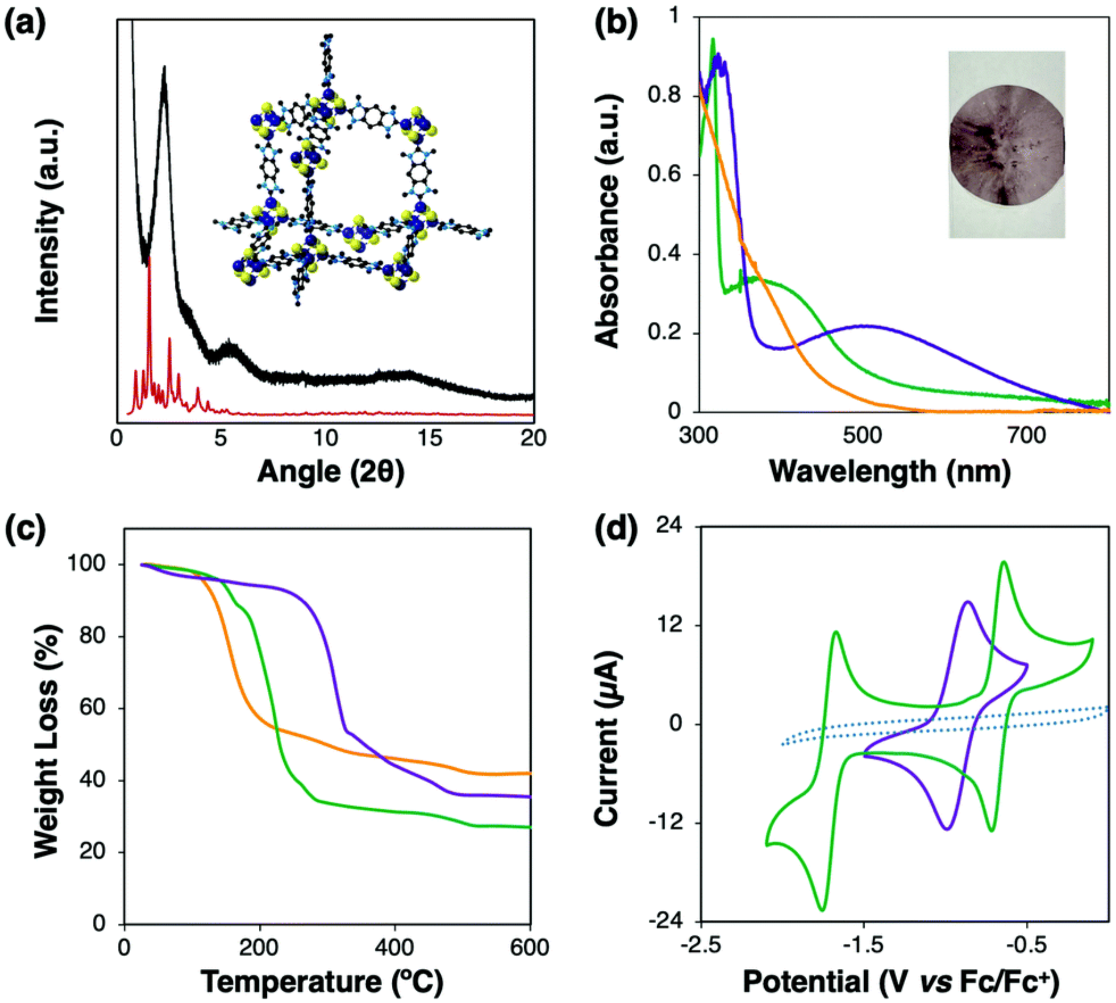

Figure 2.2 (a) Synchrotron powder X-ray diffraction pattern of Co_4S_4-MCOP (black) and simulated pattern (red) of model (inset), (b) normalized UV-vis absorption spectra (inset image of Co_4S_4-MCOP in epoxy) and (c) TGA traces of Co_4S_4-MCOP (purple), **2** (green), and **1** (orange), and (d) cyclic voltammograms of Co_4S_4-MCOP (purple; solid-state modified glassy carbon working electrode), **2** (green), and background (blue dashed). Recorded at 100 mV s^{-1} in MeCN with $TBAPF_6$.

The porosity of the polymer was analyzed using N_2 adsorption data at 77 K. Desolvated samples of Co_4S_4-MCOP exhibit a type II isotherm, with a rise in sorption at higher dinitrogen pressures (**Figure S13**). The Brunauer–Emmett–Teller (BET) surface area of Co_4S_4-MCOP was determined to be 22.2 $m^2\ g^{-1}$. The low porosity may arise from framework collapse during solvent removal or a highly interpenetrated structure.[123] Pore collapse is a common phenomenon observed when activating related MOF materials.[124] Co_4S_4-MCOP undergoes a significant volume change upon drying. Thus, we hypothesize that a structural change followed by pore occlusion occurs under vacuum.

Thermogravimetric analysis (TGA) was performed on samples of Co_4S_4-MCOP, discrete cluster **2**, and the precursor cluster **1** to compare their thermal stabilities (**Figure 2.2c**). All three samples undergo a similar, major weight loss below 300 °C that is likely a result of the dissociation of their organic ligands. The TGA traces reveal an increase in thermal stability as the phosphine ligands of 1 (≈110 °C) are substituted for NHC ligands in **2** (≈140 °C). Co_4S_4-MCOP is more stable than both molecular clusters **1** and **2**, exhibiting a degradation point at ≈240 °C. We posit that the crosslinked structure is responsible for the augmented thermal stability observed in the polymer.

Cobalt sulfide clusters are well known for their rich electrochemistry.[112] The cubane-type Co_4S_4 clusters are no exception and $Co_4S_4(Pr^i{}_2NHCMe_2)_4$ can be oxidized twice ($E^1_{1/2}$ = -1.4 and $E^2_{1/2}$ = -0.2 V vs. Fc/Fc^+) to form $[Co_4S_4]^{+1}$ and $[Co_4S_4]^{+2}$, respectively.[119] Accordingly, cluster **2** also undergoes two oxidations at similar potentials ($E^1_{1/2}$ = -1.7 and $E^2_{1/2}$ = -0.67 V) (**Figure 2.2d**). This prompted us to investigate the redox properties of the polymer. We prepared electrodes modified with the insoluble Co_4S_4-MCOP to study its electrochemistry in the solid state (**Figure 2.2d**). These electrodes were submerged in solutions of MeCN with tetrabutylammonium hexafluorophosphate ($TBAPF_6$) supporting electrolyte and subject to cyclic voltammetry (CV) scans. The Co_4S_4-MCOP solid exhibits a single reversible redox event at −0.9 V vs. Fc/Fc^+. This potential is in a similar voltage range to the corresponding, discrete cluster **2**. Therefore, we attribute this process to the reversible oxidation of the Co_4S_4 units in the solid. The lack of other features in the CV and relative uniformity of the redox wave indicates that all cluster entities in the framework are in the equivalent oxidation state with the same supporting ligands.

Some NHC-transition metal complexes and clusters have been shown to undergo exchange with different ligand types as well as other monomeric NHCs.[84, 125, 126]These reports encouraged us to mix the polymer with a monocarbene in an effort to extract a molecular species. Thus, suspensions of Co_4S_4-MCOP in C_6D_6 were heated with excess $Pr^i{}_2NHCMe_2$ (20 equivalents). After 24 hours, a trace amount of solid remained and the solution had changed from transparent to red-brown (**Figure S16**). A filtered aliquot of this solution was collected and studied via1H NMR spectroscopy (**Figure 2.3**). The spectrum of the digested sample contains diagnostic signals at 5.3 and 7.3 ppm, which correspond to the NMR spectrum of the discrete cluster $Co_4S_4(Pr^i{}_2NHCMe_2)_4$. [119] Specifically, these resonances are assigned to methyl protons on the isopropyl groups and methyl protons attached to the imidazolylidene ring, respectively. Additionally, a broad singlet was observed at −11.8 ppm. This unique resonance from the isopropyl methine protons is also consistent with the spectrum of the 0D cluster and confirms that the Co_4S_4 unit can be excised from the polymer. The NMR experiment further indicates that the

Co_4S_4 entity remains intact during polymerization and provides direct evidence for the dynamicity of the Co–CNHC bond in the polymer.

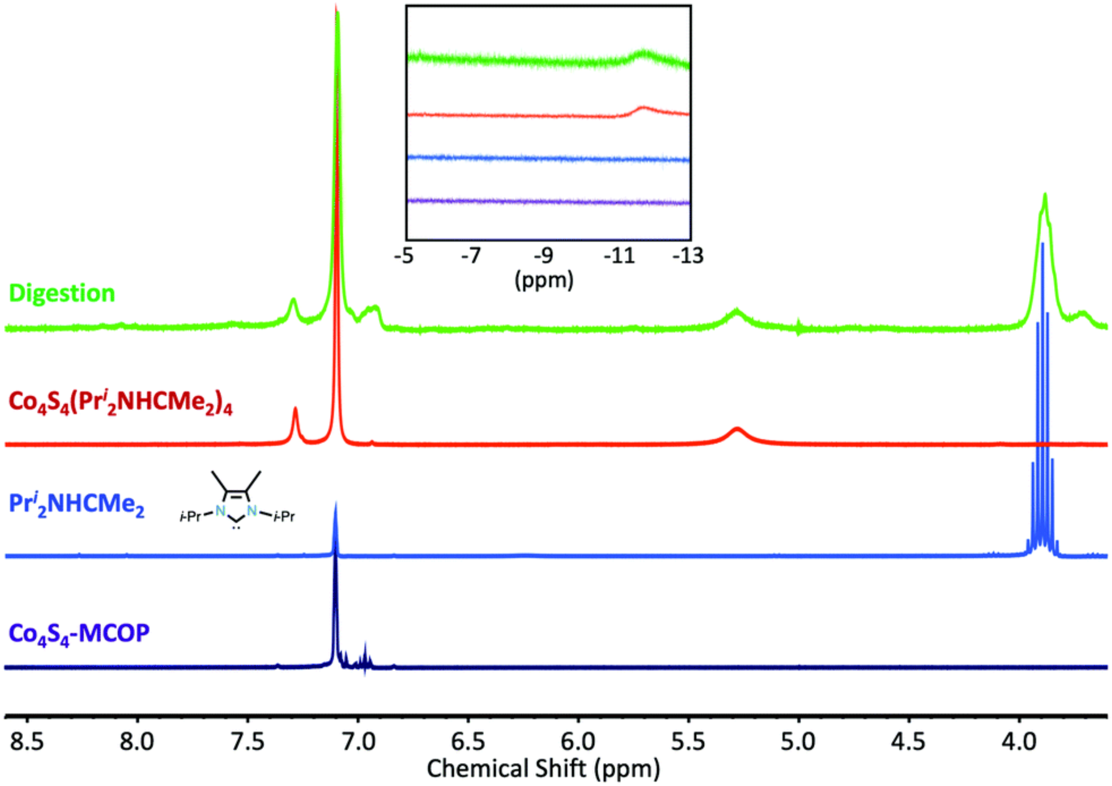

Figure 2.3 NMR spectra overlay of Co_4S_4-MCOP (purple); $Pr^i{}_2NHCMe_2$ (blue); discrete $Co_4S_4(Pr^i{}_2NHCMe_2)_4$ (red); and mixture of Co_4S_4-MCOP and $Pr^i{}_2NHCMe_2$ after digestion (green) in C_6D_6.

Finally, we sought to exploit the reversible nature of the Co–C_{NHC} bonding to regulate the nucleation rate during polymerization. We hypothesized that a mono-NHC could act as a competitive capping agent (modulator) and decrease the rate of nucleation prior to solid formation. To this end, a series of solvothermal polymerizations were run in the presence of increasing equivalents of **3**. We found that larger amounts (5–15 equivalents) of modulator led to a decrease in the rate of solid formation. Polymerization does not occur at an appreciable rate under conditions of high modulator concentration (≥20 equivalents), further corroborating our observations in the digestion experiments.

Precipitate isolated from reactions run in the presence of 10 equivalents of 3 also appeared markedly different via SEM (**Figure. S17**). These modulated syntheses yielded product that was uniform in size (645 ± 166 nm), less stringy, and more particle-like than material isolated from reactions run in the absence of capping agents.

2.4 Conclusions

In summary, we have designed and synthesized the first example of a MCOP consisting of poly-NHC linkers and molecular cluster nodes. The material is redox active and can be depolymerized to obtain discrete, soluble Co_4S_4 entities. The rate of polymerization was found to be tunable, which may provide a means to single-crystalline NHC-MCOPs in the future. Finally, this study paves the way for a new class of functional MCOPs comprising poly(NHC) ligands and clusters of different sizes, geometries, and compositions. We have only just begun to explore that vast field of metal-sulfide clusters and carbene linkers. Such (NHC)linkers have considerable steric and electronic tunability, not to mention the large number of mesoionic or ‘abnormal’ carbenes generally found to be more electron donating.[127]

2.5 Appendix A: Chapter 2 Supplementary Information

2.5.1 Single Crystal X-ray Diffraction Figures

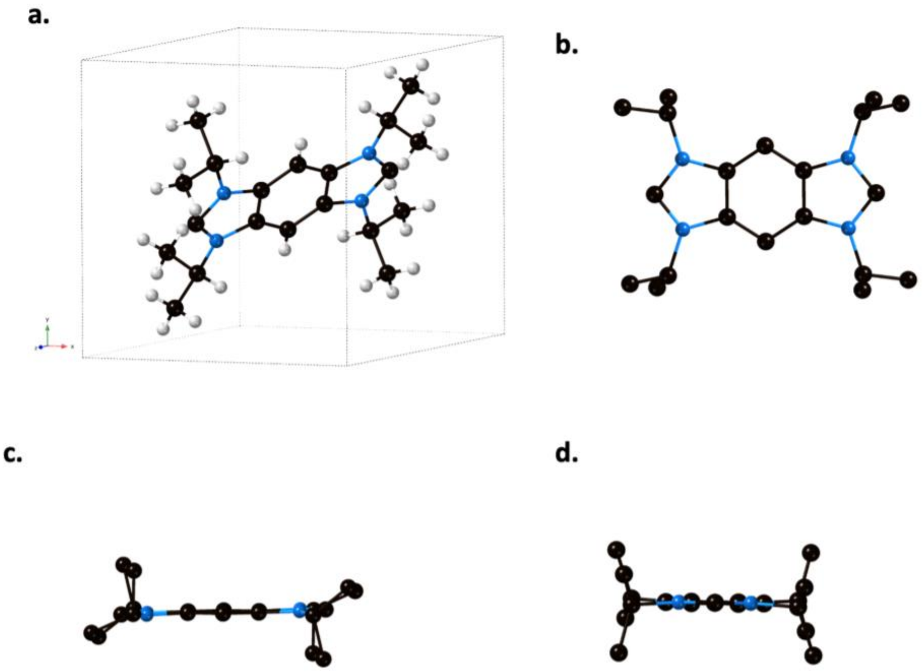

Figure S1. Single crystal X-ray structure of 4 depicted as ball-and-stick. (a) unit cell; (b) top view; (c) side view; (d) front view looking down CNHC. Nitrogen, light blue; carbon, black; hydrogen, white.

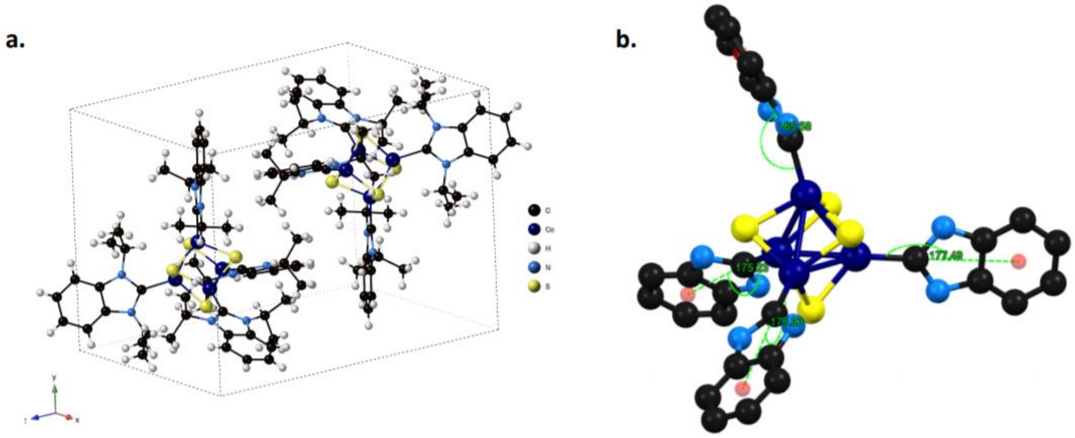

Figure S2. Single crystal X-ray structure of **2** depicted as ball-and-stick. (a) unit cell; (b) view depicting the bent, nonlinear (166º) connection of the top Co-CNHC bond with isopropyl groups and hydrogen atoms omitted. Cobalt, dark blue; sulfur, yellow; nitrogen, light blue; carbon, black; hydrogen, white.

2.5.2 Scanning Electron Micrographs & Energy Dispersive X-ray Spectroscopy

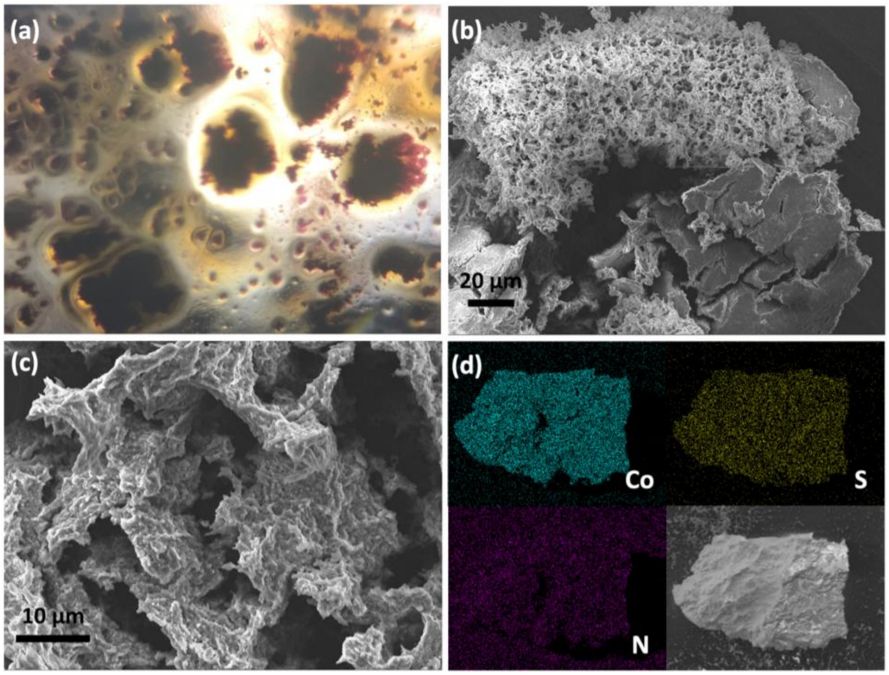

Figure S3. (a) Microscope image of Co_4S_4-MCOP at 30X magnification; (b) and (c) SEM micrographs of Co_4S_4-MCOP; and (d) EDS analysis mapping of Co_4S_4-MCOP (teal: cobalt; yellow: sulfur; purple: nitrogen).

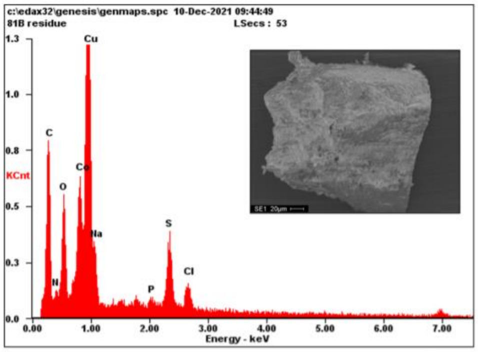

Element	Wt%	At%
CK	28.55	57.66
NK	02.22	03.85
OK	05.78	08.76
CoL	11.12	04.58
CuL	40.35	15.40
NaK	02.92	03.08
PK	00.70	00.55
SK	05.67	04.29
ClK	02.69	01.84
Matrix	Correction	ZAF

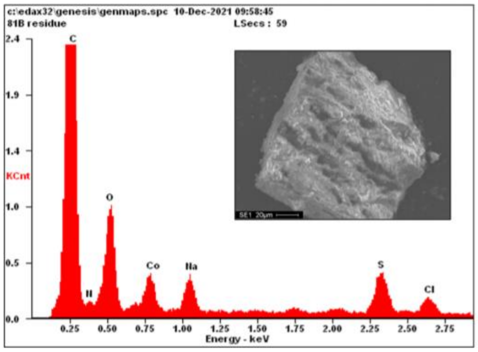

Element	Wt%	At%
CK	65.64	78.09
NK	04.76	04.86
OK	11.93	10.65
CoL	08.68	02.10
NaK	02.17	01.35
SK	04.59	02.05
ClK	02.23	00.90
Matrix	Correction	ZAF

Figure S4. EDS survey scans and elemental composition of Co_4S_4-MCOP. The top spectrum was collected using copper tape as a background and the bottom spectrum was run with the sample placed on carbon tape.

2.5.3 Nuclear Magnetic Resonance Spectroscopy

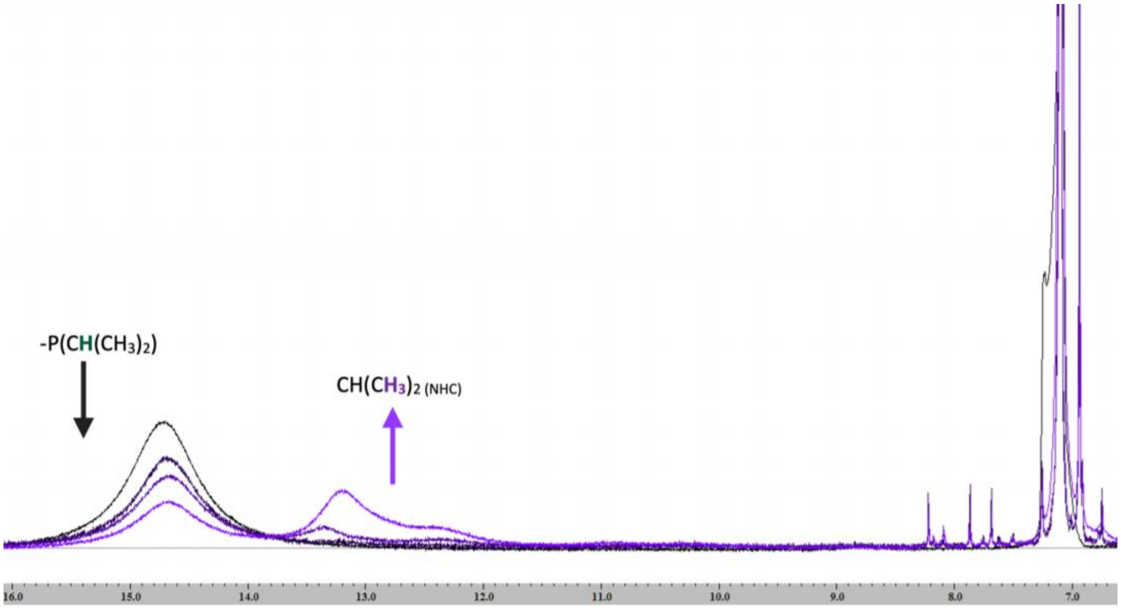

Figure S5. Polymerization reaction monitored via ^{1}H-NMR in C_6D_6. NMR was taken with cluster **1** only (black) then 2.5 equivalents of biscarbene **4** were added and the NMR was collected again after 1 hour, 18 hours, and 72 hours. The same experiment was also run while heating but proceeded too quickly to monitor.

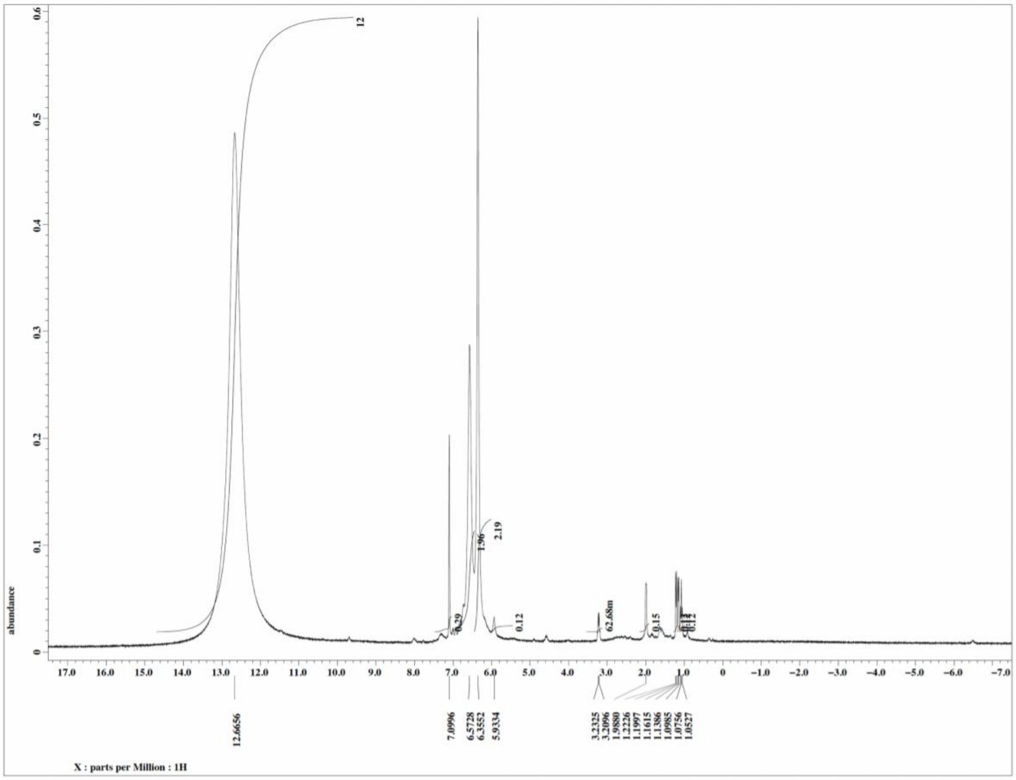

Figure S6. ^{1}H-NMR spectrum of **2** in C_6D_6.

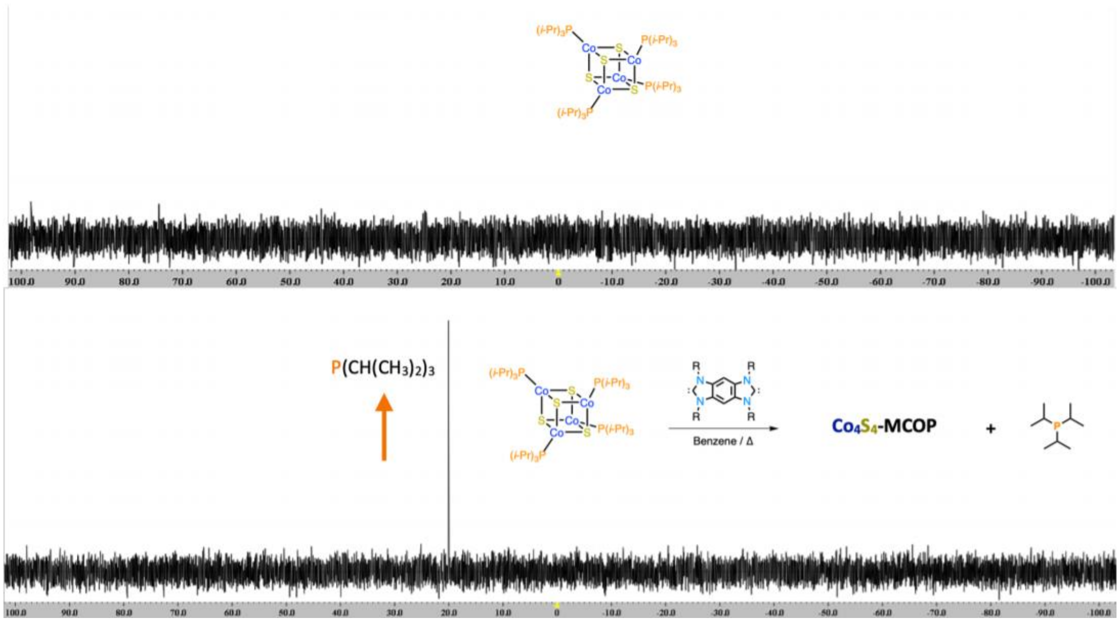

Figure S7. Polymerization reaction monitored via ^{31}P-NMR in C_6D_6. Cluster **1** (top spectrum) and Cluster **1** mixed with two equivalents of biscarbene **4** after heating for one hour (bottom spectrum).

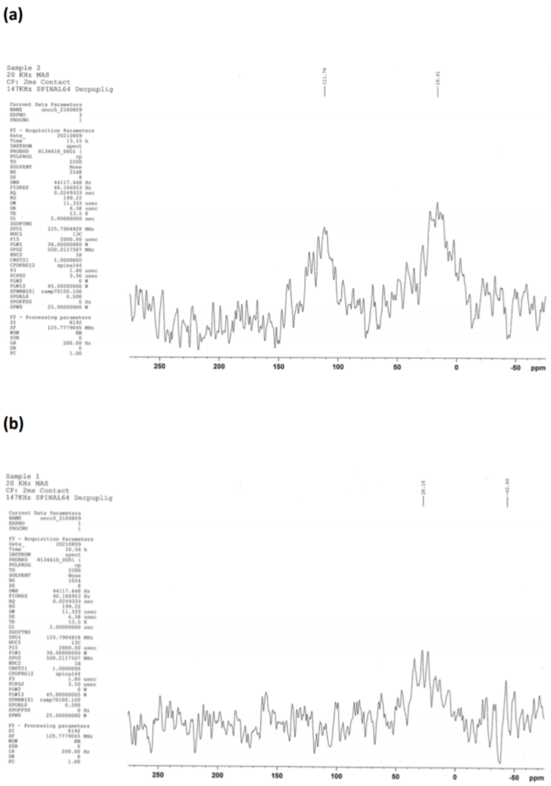

Figure S8. Solid State CP-MAS ^{13}C-NMR spectra of (a) **2** and (b) Co_4S_4-MCOP. The spectra are unable to be resolved due to the paramagnetic nature of the compounds.

2.5.4 Infrared Spectroscopy

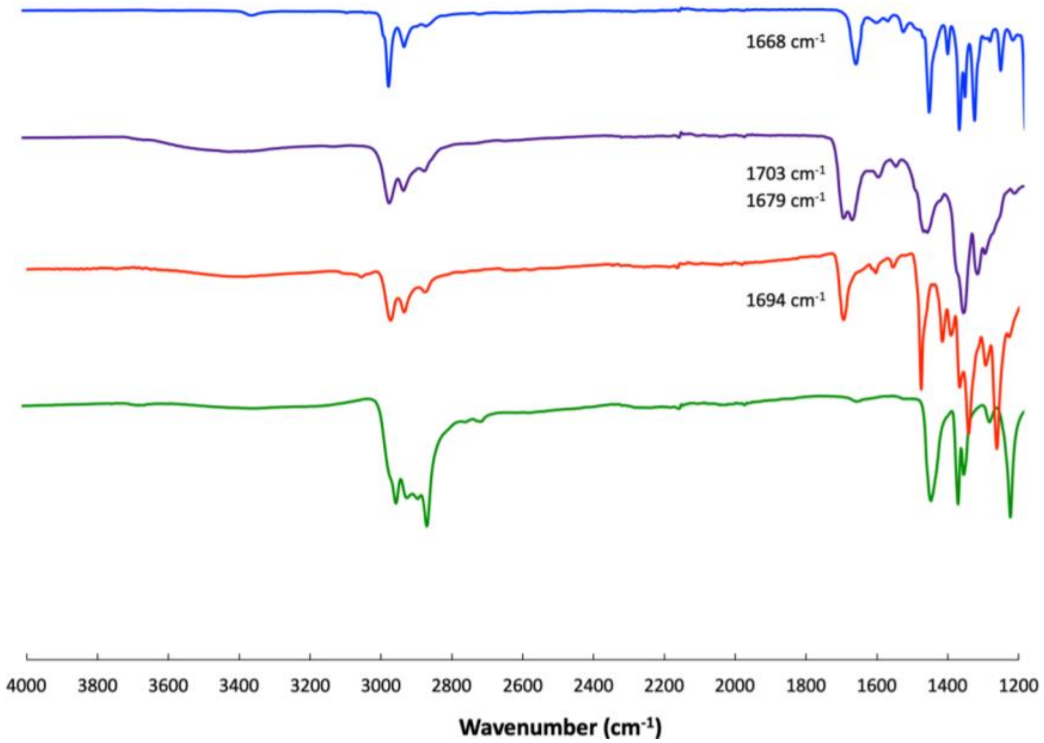

Figure S9. Infrared spectra of **4** (blue), Co_4S_4-MCOP (purple), **2** (red), and **1** (green).

2.5.5 X-ray photoelectron spectroscopy

Thermo Scientific Avantage Data System software was used for the acquisition and processing of the data. Using a smart background, atomic percentages were calculated from the absolute peak intensity signal of each element detected in the survey spectra of each sample. Elements detected in the survey spectra were studied at characteristic binding energies (BE) to assess the intensity (count/second) of each signal. Characteristic binding energies were compared with data from the Thermo Fisher XPS Knowledge Database. Sulphur spectra were collected in a binding energy range of 157-174 eV. Carbon spectra were collected in a binding energy range of 279-294 eV. Nitrogen spectra were collected in a binding energy range of 392-406 eV. Oxygen spectra were collected in a binding energy range of 525 - 534 eV. Cobalt spectra were collected in a binding energy range of 771 - 812 eV. XPS measurements were made at 3 discrete spots on each powdered sample. A slight increase in oxygen percent is expected due to oxidation during transfer, as well as background adventitious carbon is expected due to surface contamination (~285 eV). Reported atomic compositions are calculated from the average of the three spot measurements of each sample.

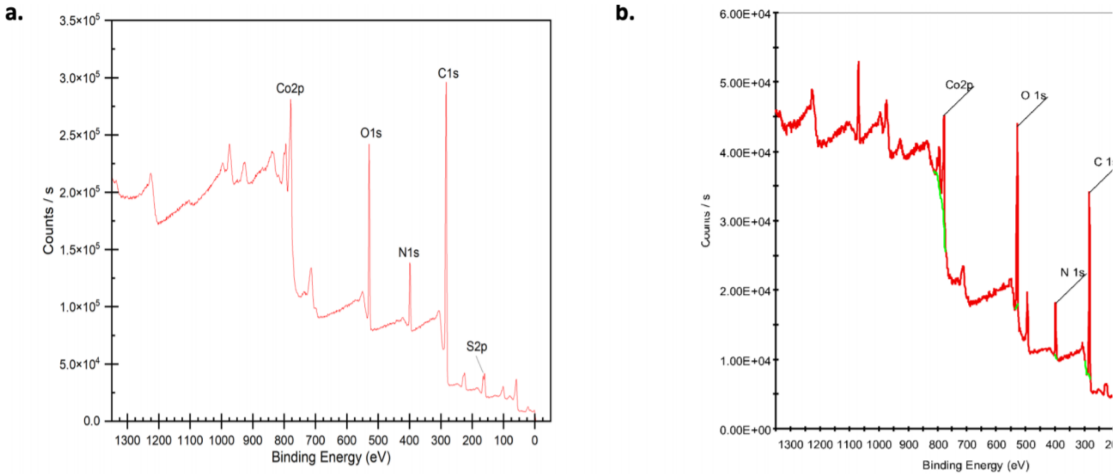

Figure S10. XPS survey spectra of (a) **2** and (b) Co_4S_4-MCOP.

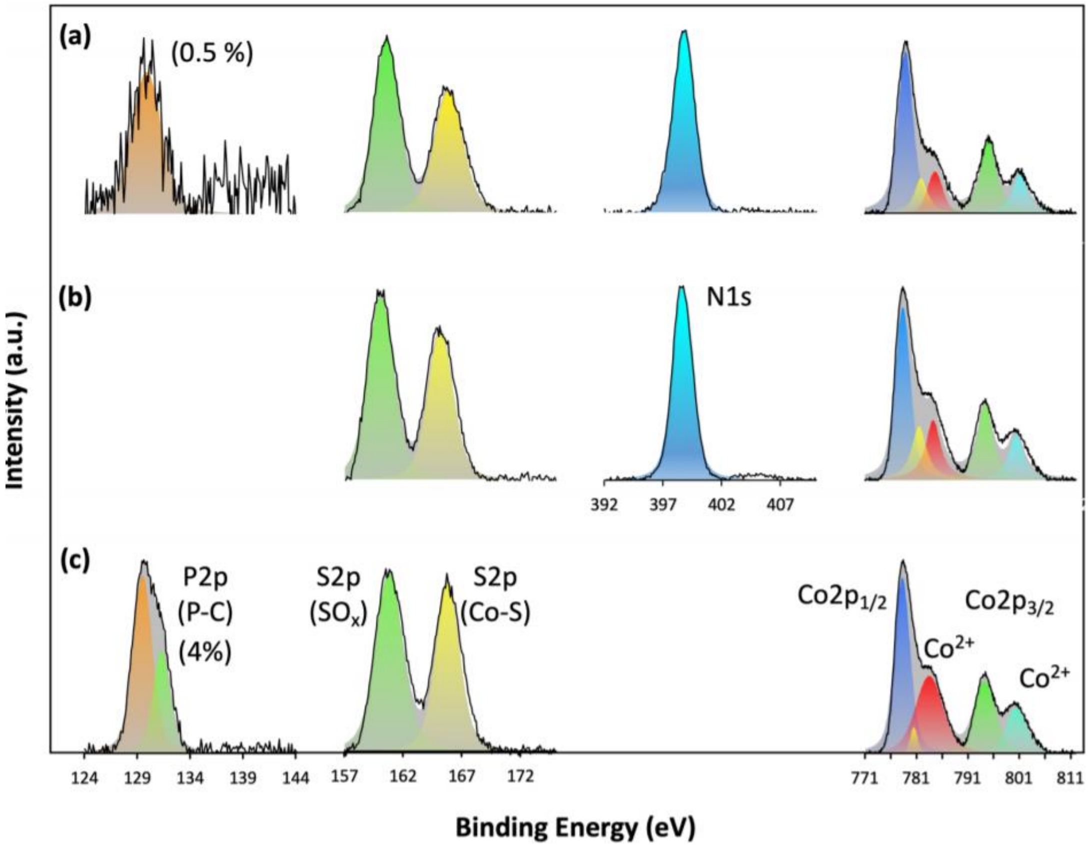

Figure S11. High Resolution X-ray photoelectron spectra of (a) Co_4S_4-MCOP, (b) [$Co_4S_4(Pr^i{}_2NHCBz)_4$] **2**, and (c) [$Co_4S_4(PPr^i{}_3)_4$] **1**.

2.5.6 UV-Vis Absorption Spectroscopy

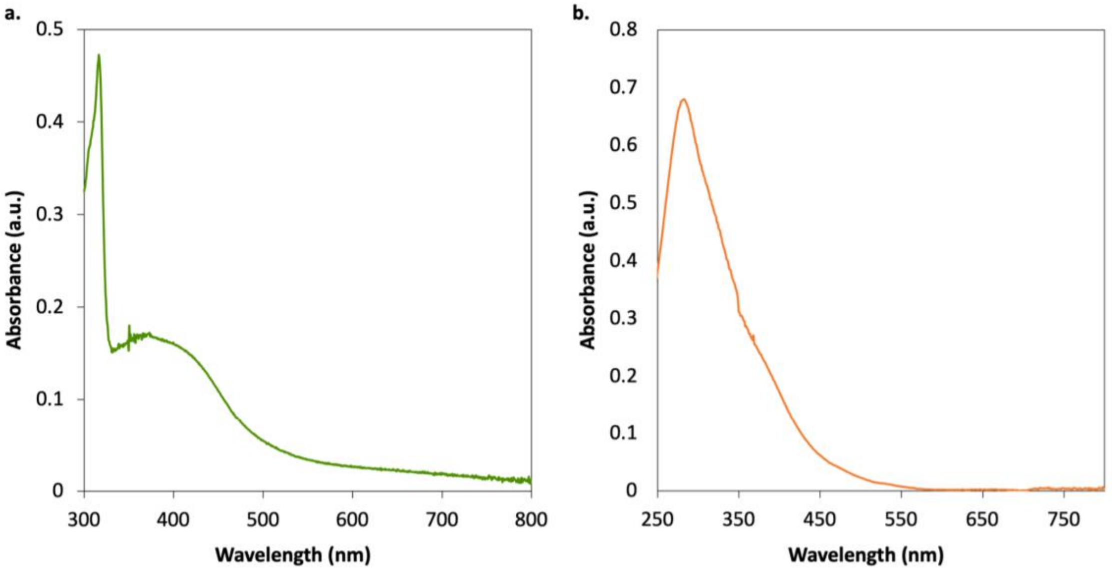

Figure S12. UV-vis absorption spectra of (a) **2** (0.1 mM in THF) and (b) **1** (0.1 mM in THF).

2.5.7 Surface Area Analysis

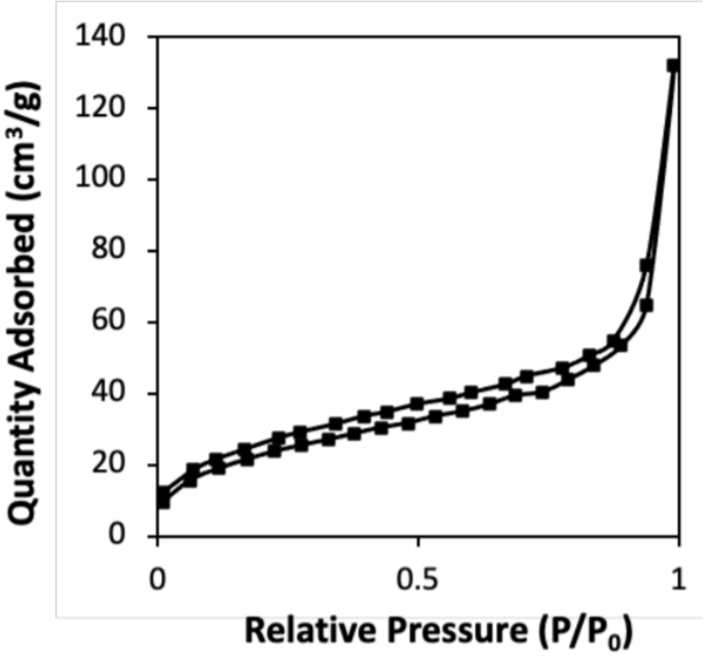

Figure S13. N_2 adsorption and desorption isotherms at 77K of Co_4S_4-MCOP.

2.5.8 Electrochemistry

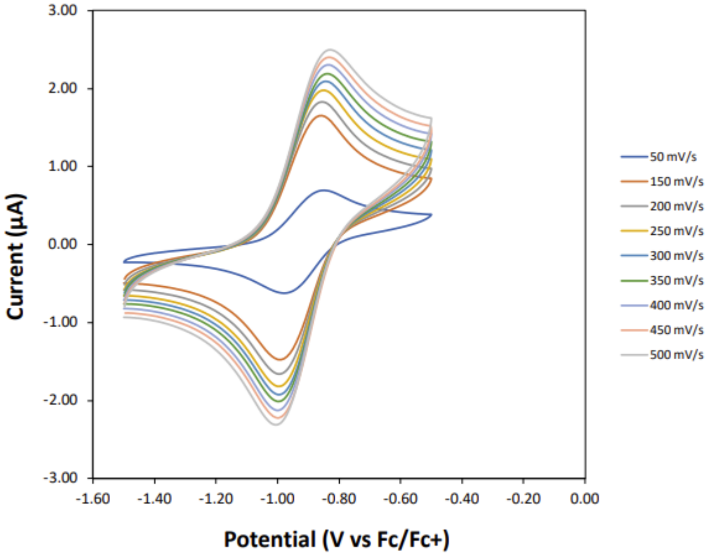

Figure S14. Cyclic voltammograms of Co_4S_4-MCOP modified glassy carbon working electrode at various scan rates. Recorded using a Pt wire counter electrode and Pt pseudo reference electrode in acetonitrile with $TBAPF_6$ as the supporting electrolyte and referenced vs Fc/Fc^+.

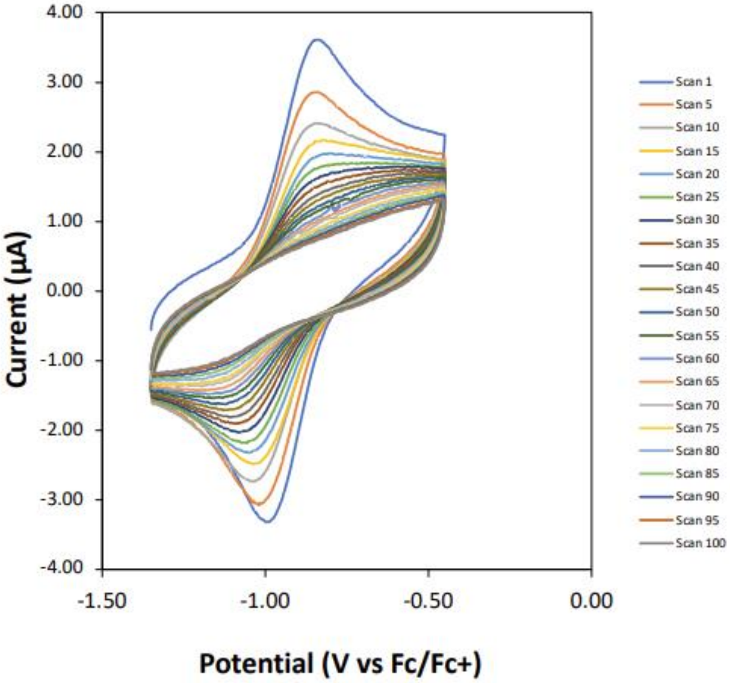

Figure S15. Cyclic voltammograms of Co_4S_4-MCOP modified glassy carbon working electrode scanned at 50 mV/s for 100 sequential scans. Recorded using a Pt wire counter electrode and Pt pseudo reference electrode in acetonitrile with $TBAPF_6$ as the supporting electrolyte and referenced vs Fc/Fc^+ .

2.5.9 Digestion/Excision Experiment

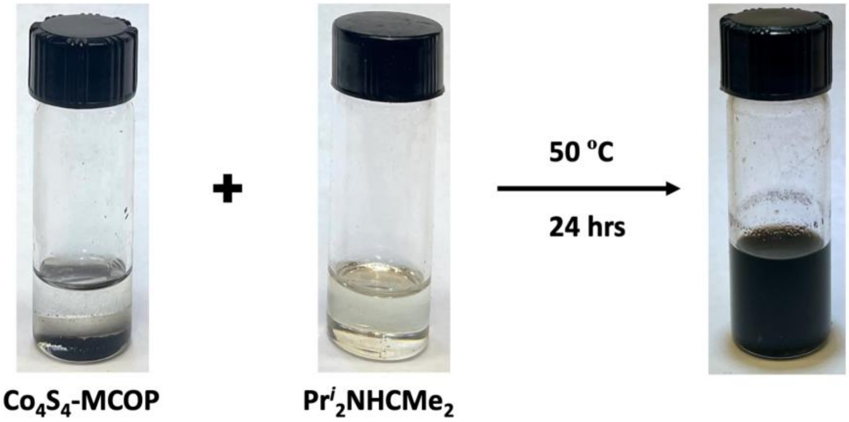

Figure S16. Images from digestion experiment. Suspension of Co_4S_4-MCOP and $Pr^i_2NHCMe_2$ (20 equivalents) in C_6D_6 were mixed and heated for 50 ºC for 24 hours.

2.5.10 SEM Micrographs of Modulated Polymerization

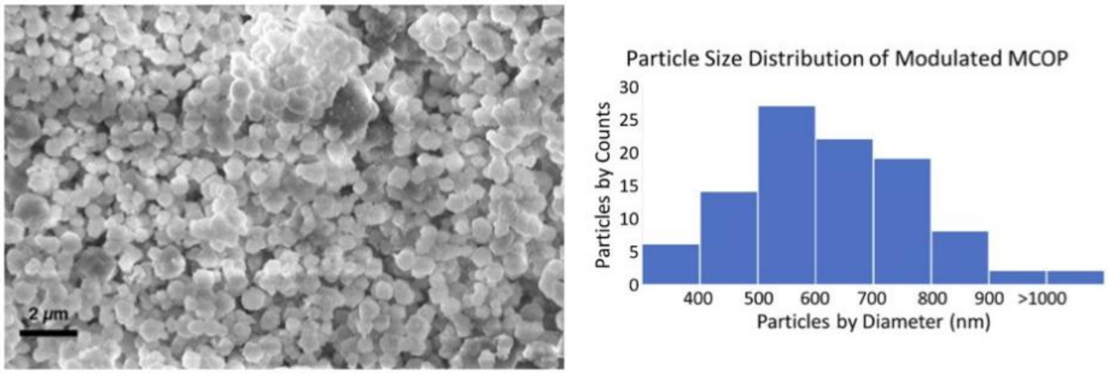

Figure S17. SEM micrograph from modulated synthesis of Co_4S_4-MCOP using 10 equivalents of $Pr^i_2NHCMe_2$ as a coordination modulator in toluene and particle size distribution histogram as calculated from a sample size of 100 using ImageJ.

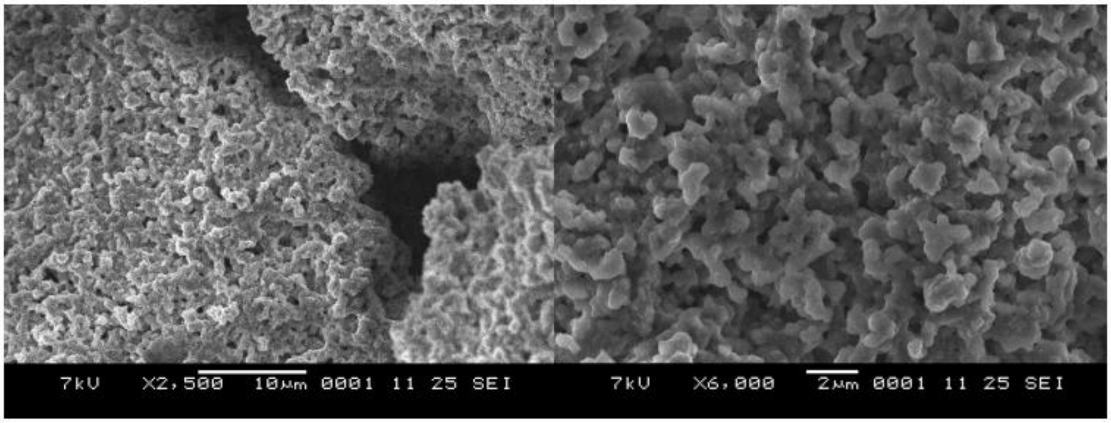

Figure S18. SEM micrographs from modulated synthesis of Co_4S_4-MCOP using 10 equivalents of $Pr^i_2NHCMe_2$ as a coordination modulator in dioxane.

2.5.11 Pre and Post Cyclic Voltammetry SEM/EDS Study

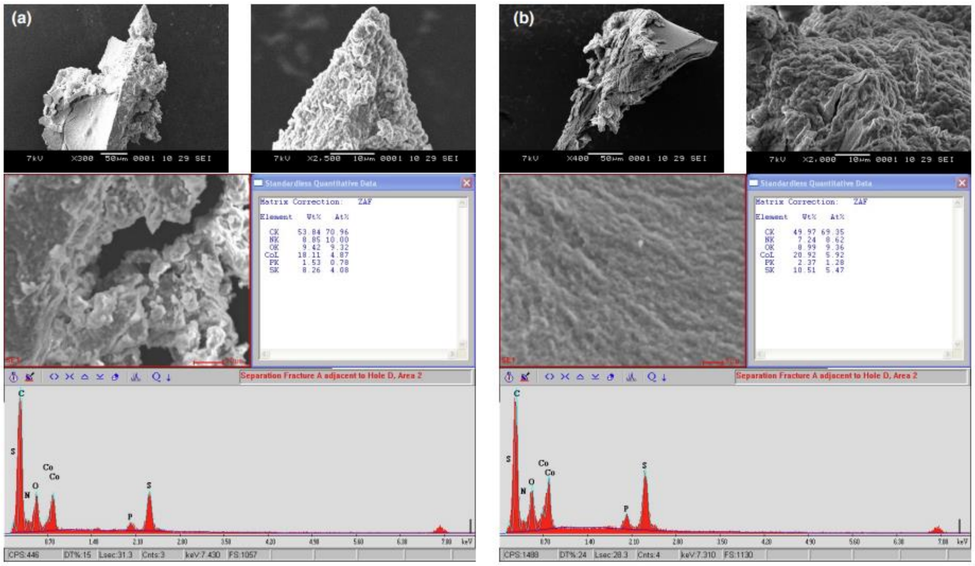

(a)

```
Matrix Correction:   ZAF

Element    Wt%   At%

  CK     53.84 70.96
  NK      8.85 10.00
  OK      9.42  9.32
 CoL     18.11  4.87
  PK      1.53  0.78
  SK      8.26  4.08
```

(b)

```
Matrix Correction:   ZAF

Element    Wt%   At%

  CK     49.97 69.35
  NK      7.24  8.62
  OK      8.99  9.36
 CoL     20.92  5.92
  PK      2.37  1.28
  SK     10.51  5.47
```

Figure S19. (a) SEM micrographs and EDS scans of Co_4S_4-MCOP before cyclic voltammetry

2.5.12 Characterization of Co_4S_4-MCOP-Et

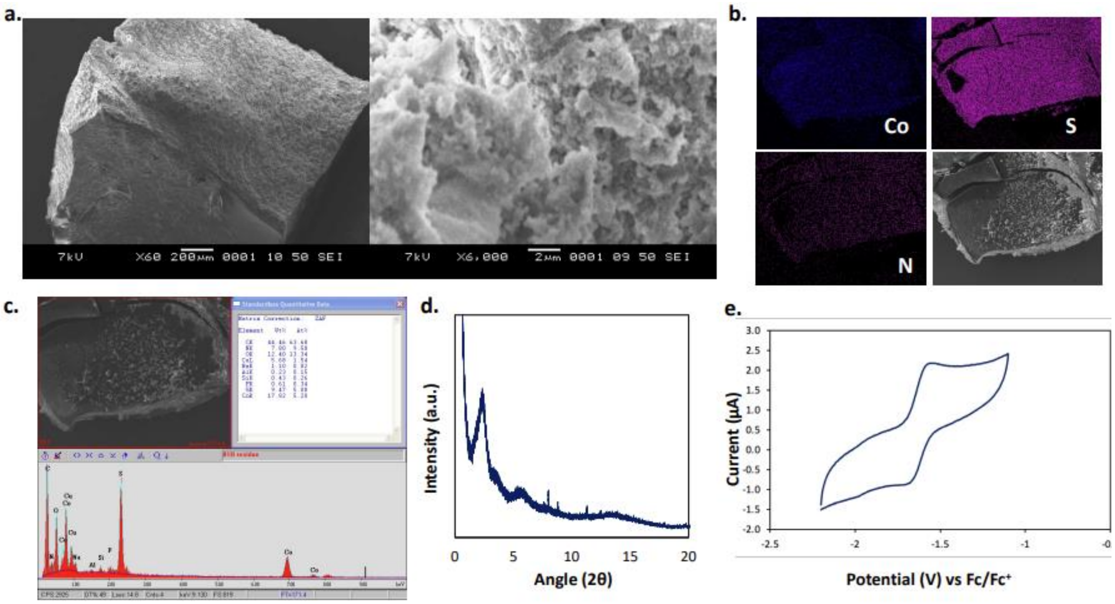

Figure S20. Characterization of Co_4S_4-MCOP-Et. SEM micrographs (a); EDS mapping (b); EDS scans and elemental composition (c); PXRD pattern (d); solid-state cyclic voltammetry of polymer-modified glassy carbon working electrode, Pt counter electrode, and Pt pseudo reference electrode at a scan rate of 100 mVs^{-1} in a solution of acetonitrile with $TBAPF_6$ as the supporting electrolyte and referenced vs Fc/Fc^{+} .

2.5.13 X-ray Diffraction Procedures and Tables

X-ray diffraction data were collected using an Agilent/Oxford Diffraction Gemini A Ultra diffractometer. The diffractometer was equipped with a sealed-tube Mo source with a graphite monochromator (λ=0.71073 Å) and a sealed-tube Cu source with graphite focusing optics (λ=1.54184 Å). In all cases data were collected to better than 0.8 Å resolution. The CrysAlisPro diffractometer software[128] provided intensity data corrected for Lorentz, polarization, and absorption effects. Preliminary structure solutions were found with the AutoChem software package.[128] Final structures were solved with SHELXT[129] (direct methods) and refined with SHELXL[130], using the Olex2 software package.[131] Anisotropic refinement for all nonhydrogen atoms was performed. Hydrogen atoms were placed in calculated positions. Compound [$Co_4S_4(Pr^i{}_2NHCBz)_4$] was refined using a solvent mask applied using BYPASS.[132] Using the solvent mask, 45 electrons were found in a volume of 445 Å4 in 2 voids per unit cell. This is consistent with the presence of 0.5[$C_4H_{10}O_1$] per Asymmetric Unit which account for 42 electrons per unit cell.

Publication tables and graphics were generated with the WinGX suite of programs.[133]

Table S1 Crystal data and structure refinement for biscarbene 4.

Identification code	ac_cb_c20h30n4_cu
Empirical formula	$C_{20}H_{30}N_4$
Formula weight	326.48
Temperature/K	101(2)
Crystal system	monoclinic
Space group	$P2_1/c$

a/Å	8.7820(3)
b/Å	9.2791(3)
c/Å	11.5020(5)
α/°	α/°
β/°	94.287(3)
γ/°	90
Volume/Å3	934.66(6)
Z	2
ρ_{calc}g/cm^3	1.160
μ/mm^{-1}	0.537
F(000)	356.0
Crystal size/mm^3	0.18 × 0.085 × 0.051
Radiation Cu Kα	(λ = 1.54184)
2Θ range for data collection/°	10.1 to 133.722
Index ranges	$-10 \leq h \leq 9$, $-10 \leq k \leq 11$, $-13 \leq l \leq 13$
Reflections collected	8721
Independent reflections	1655 [R_{int} = 0.0514, R_{sigma} = 0.0323]
Data/restraints/parameters	1655/0/113
Goodness-of-fit on F^2	1.052
Final R indexes [I>=2σ (I)]	R_1 = 0.0394, wR_2 = 0.0922
Final R indexes [all data]	R_1 = 0.0544, wR_2 = 0.1017
Largest diff. peak/hole / e Å^{-3}	0.14/-0.20

Table S2 Crystal data and structure refinement for [$Co_4S_4(Pr^i{}_2NHCBz)_4$]

Identification code	g2-50
Empirical formula	C52H72Co4N8S4
Formula weight	1173.13
Temperature/K	100.00(10)
Crystal system	triclinic
Space group	P-1
a/Å	12.9073(5)
b/Å	13.2862(5)
c/Å	17.5673(6)
α/°	94.342(3)
β/°	95.063(3)
γ/°	93.514(3)
Volume/$Å^3$	2985.22(19)
Z	2
ρcalcg/cm^3	1.305
μ/mm^{-1}	1.271
F(000)	1224.0
Crystal size/mm^3	0.481 × 0.318 × 0.145
Radiation Mo Kα	(λ = 0.71073)
2Θ range for data collection/°	6.74 to 57.264
Index ranges	$-16 \leq h \leq 16$, $-16 \leq k \leq 17$, $-22 \leq l \leq 22$
Reflections collected	59734

Independent reflections	13795 [Rint = 0.0580, Rsigma = 0.0620]
Data/restraints/parameters	13795/0/629
Goodness-of-fit on F^2	1.028
Final R indexes [I>=2σ (I)]	R_1 = 0.0416, wR_2 = 0.0813
Final R indexes [all data]	R_1 = 0.0695, wR_2 = 0.0958
Largest diff. peak/hole / e $Å^{-3}$	0.72/-0.40

CHAPTER 3: CONDUCTIVE ORGANOMETALLIC POLYMERS FROM SOLUBLE SUPERATOM IONS

Submitted - current embargo until publication

3.1 Introduction

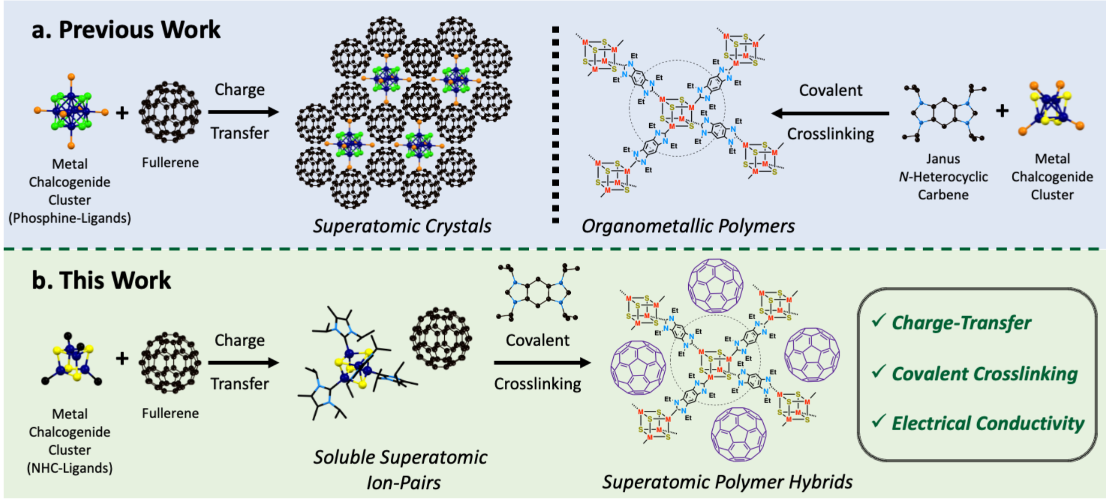

Figure 3.1 Schematic of (a) superatomic crystals formed from electron-donor metal-chalcogenide clusters and fullerene acceptors and main-chain organometallic polymers formed from phosphine stabilized metal chalcogenide cluster and Janus N-heterocyclic carbenes (NHCs). (b) New approach to main-chain organometallic polymers *via* soluble superatomic ions precursors and Janus NHCs.

Directing the assembly of superatomic clusters is an important goal in the field of materials chemistry.[16, 134, 135] A fruitful strategy for preparing extended structures of superatoms is assembly through charge-transfer.[38, 136-138] This technique requires electronically complementary cluster building blocks and results in the formation of ionic superlattices in which charged clusters are electrostatically paired.[139] Many functional, solid-state materials have been prepared using this methodology. In particular, a suite of superatomic crystals containing metal chalcogenide clusters and fullerides are a paragon of this compound class (**Figure 3.1a**).[136] The synthetic process is general and assorted metal-chalcogenide clusters of varying composition and geometry have been employed as electron-donors for this purpose, including Co_6Se_8,[136, 137] Cr_6Te_8,[136, 137] Ni_9Te_6,[136, 140] and

Ni_3Te_2[141] clusters. Multiple carbon-based nanoclusters, such as C_{60},[136, 140, 141] C_{70},[141, 142] and endohedral fullerenes[143] have also found use as the corresponding acceptor units for these superatomic crystals. The resulting hybrid materials exhibit electronic[136, 137, 141, 144] and thermal transport[145] as well as magnetic properties[140] based on the precursor clusters, degree of electron transfer, and packing arrangement. However, superatomic crystals are difficult to modify post-synthetically because they are insoluble and isolated as brittle crystals or polycrystalline powders. Thus, further transformation of such materials remains limited and necessitates the use of solid-state chemistry protocols, such as intercalation[144, 146] and exfoliation. [147, 148]

Superatomic clusters can also be assembled covalently (**Figure 3.1a**). Numerous coordination polymers have been prepared using polytopic, bridging ligands to crosslink metal chalcogenide clusters,[113-115, 149-152] metal halide clusters,[153-155] polyoxometalates,[156, 157] and others.[158, 159] These superatomic frameworks represent a significant achievement from a structural perspective. However, superatom-based materials constructed through the combination of crosslinking and charge-transfer are rare.[160, 161] This is in contrast to purely-organic charge-transfer complexes, which can be hierarchically organized into polymeric materials[162-166] and supramolecular assemblies.[167] New design protocols must be realized to unlock the full potential of superatoms as building blocks. Furthermore, a dual covalent-ionic approach may result in superatomic materials with enhanced stability and electronic coupling between cluster units.[168, 169]

3.2 Experimental

3.2.1 Chemicals

All manipulations were performed under an inert atmosphere of dry N_2 using a Schlenk line or MBraun UniLab Pro glovebox unless otherwise noted. Tetrahydrofuran (THF), toluene, dichloromethane (DCM), hexane, and diethyl ether used were dried and purged with N_2 on an MB-SPS solvent purification system from MBraun. Chlorobenzene anhydrous (99.8%, Aldrich), o-dichlorobenzene anhydrous (Drisolve), and acetonitrile (Drisolve) were freeze pump thawed 3-4x. NaH 60% in mineral oil (Aldrich) for imidazolium deprotonation was washed thoroughly over a medium filter with hexane under a N_2 atmosphere and pumped dry. All other chemicals were purchased from commercial sources and used as received, including N,N-dimethylformamide anhydrous/under argon (99.8%, Alfa Aesar), 1,2,4,5-benzenetetramine tetrahydrochloride (95%, Aldrich), formic acid (96%, Alfa Aesar), hydrochloric acid (Macron Fine Chemicals), bromoethane (98% Alfa Aesar), sodium carbonate monohydrate (99.5%, Alfa Aesar), anhydrous potassium carbonate (99%, EMD), benzimidazole (98%, Acros Organics), cobalt (II) chloride anhydrous (99.7%, Alfa Aesar), iron (II) chloride anhydrous (99.5%, Alfa Aesar), triisopropylphosphine (98%, Alfa Aesar), bis(trimethylsilyl)-sulfide (95%, Acros Organics), KOtBu (potassium tert-butoxide, 98%, Aldrich), and potassium chunks in mineral oil (98%, Alfa Aesar).

3.2.1 Synthesis

***$Fe_4S_4(Pr^i{}_2NHCMe_2)_4$* (1)**. Dichlorobis(triisopropylphosphine)iron(II) [$FeCl_2(PPr^i{}_3)_2$] was first prepared following a modified procedure.[1] Specifically, the mixture of $FeCl_2$, triisopropylphosphine, and benzene were stirred for three hours at 60 ºC in a sealed tube.

The tube was then transferred to an oven and heated to 100 ºC for 48 hours. The solution was then filtered hot inside a glovebox and dried in vacuo to yield a light-lavender colored solid. Then, $Fe_4S_4(Pr^i{}_2NHCMe_2)_4$ cluster was prepared following a modified procedure by Holm and coworkers.[2] A solution of $[FeCl_2(PPr^i{}_3)_2]$ (0.945 g, 2.11 mmol) in THF (21 mL) was added into a solution of $(Me_3Si)_2S$ (0.754 g, 4.22 mmol) in THF (21 mL). The reaction was stirred for 2 days. The resulting solution was pumped dry to give a brown oily residue, which was dissolved in 21 mL benzene and filtered. The solution was then treated with a solution of $Pr^i{}_2NHCMe_2$ (0.760 g, 4.64 mmol) in benzene (6 mL). The brown mixture was stirred for 4 days and subsequently filtered. The filtrate was vapor diffused with hexane for 3 weeks. Yield: 0.30 g, 70%. ^{1}H NMR (C_6D_6): δ 19.43 (1), 12.45 (br, 2). Methine proton signals were not observed.

$Co_4S_4(Pr^i{}_2NHCMe_2)_4$ (2). This cluster was synthesized according to Holm and coworkers from the $Co_4S_4(P^iPr_3)_4$.[3] The cluster is isolated as a dark-black crystalline solid and the purity is verified using ^{1}H-NMR spectroscopy.

Janus bis(NHC) **(3) .** The free Janus biscarbene was prepared following a modified procedure by Bielawski and coworkers.[4] The solid imidazolium dibromide (130 mg, 0.30 mmol), NaH (28.7 mg, 1.20 mmol), and KOtBu (2.5 mg, 22 μmol) were suspended in THF (5 mL) and stirred for 20 h. The resulting suspension was syringe filtered and dried in vacuo to get dark red solid product. Yields vary between 20-50%.

***1•C_{60}*.** Cluster **1** (16.7 mg, 0.0155 mmol) was first dissolved in toluene (5 mL). In a separate vial, a purple solution of C_{60} (11.2 mg, 0.0155 mmol) was prepared by stirring in toluene (5 mL). Then, the purple C_{60} solution was syringe filtered and added into a 40-dram vial. A 2.5 mL toluene intermediate layer was added on top of C_{60} solution. Next, the solution of **1** in toluene was syringe-filtered and slowly added as a top layer. The vial was left undisturbed for two days. As a result, long needle-crystals were formed at the bottom of the vial. These crystals were washed with toluene and dried in vacuo.

***2•C_{60}*.** Cluster **2** (26 mg,) was first dissolved in toluene (5 mL) and syringe filtered. In a separate vial, a purple solution of C_{60} (30 mg, 0.042 mmol) was prepared by stirring in toluene (10 mL) overnight. Then, the purple C_{60} solution was syringe filtered and added into a 4-dram vial. Next, the solution of **1** in toluene was slowly added as a top layer. The vial was left undisturbed for two days. Long needle-crystals were formed at the bottom of the vial. These crystals were washed with toluene and dried in vacuo. Single crystals can be prepared by dissolving both clusters in chlorobenzene in high concentration and allowing the solution to sit for 48 hours.

MCOP-1. Cluster **1** (59 mg, 0.0547 mmol) and Janus bis(NHC) **3** (37 mg, 0.137 mmol) were weighed into two, separate 20 mL vials, and each was dissolved in benzene (7 mL). The solutions were transferred and mixed into a Chemglass pressure vessel and sealed under a N_2 atmosphere. The vessel was placed in an oven at 100 °C. After 2 days, the resulting dark blue solid was separated by centrifugation and washed with THF inside the glovebox. Pumping dry under vacuum produced solid with substantially less volume. The reaction can also be carried out in toluene or dichlorobenzene.

Depolymerization of MCOP-1. A suspension of polymer in deuterated benzene (1.2 mL) was mixed with a solution of excess free carbene $Pr^i{}_2NHCMe_2$ (~20 equiv., 1.2 mL) in a 2-dram vial. The solution was stirred for two days inside the glovebox on a hotplate at 50 ºC. During this time, the majority of the solid dissolved and the solution turned dark, reddish brown. The solution was allowed to sit for several hours before an aliquot (1 mL) was taken from the top of the reaction mixture and analyzed by NMR. The ^1H NMR spectrum of the depolymerized polymer exhibits the peaks associated with discrete cluster **(1)** at δ 19.43 (1), 12.45 (br, 2) in C_6D_6.

MCOP-2. The polymer can be prepared from the phosphine- or NHC-ligated cluster ($Co_4S_4(P^iPr_3)_4$ or **2**). See previous report for full synthetic details.[5]

MCOP-1•C_{60} and MCOP-2•C_{60}. Both polymers were prepared in the same fashion. A synthetic prep for **MCOP-1•C_{60}** is as follows: Cocrystal 2•C_{60} (29 mg 0.016 mmol) was dissolved in dichlorobenzene (7 mL) and syringe filtered into a solution of **3** (10 mg, 0.035 mmol) in dichlorobenzene (7 mL). The mixture was heated to 100 ºC for 3 days. The solution turns clear after this time and a dark precipitate is isolated via centrifugation. The solid is washed repeatedly with dichlorobenzene and toluene and then dried in vacuo.

Post Synthetic MCOP Doping. A saturated solution of C_{60} in toluene is prepared and syringe filtered. This solution is added to **MCOP-1** or **MCOP-2** and allowed to sit overnight. The suspension is centrifuged, washed with toluene, and dried in vacuo.

***MCOP-2•BF$_4$*.** The oxidized cluster was first prepared according to a literature prep from $Co_4S_4(P^iPr_3)_4$ and $[Cp_2Fe](BF_4)$.[3] The MCOP was synthesized in the same manner as **MCOP-1•C_{60} and MCOP-2•C_{60}**: **2•BF_4** was dissolved in dichlorobenzene, syringe filtered, and added to 2.5 equivalents of **3** dissolved in dichlorobenzene. The mixture was placed inside of a Chemglass pressure vessel and heated to 100 ºC overnight. The dark precipitate was collected and washed with dichlorobenzene and toluene and then dried overnight under reduced pressure.

3.2.1 Characterization

Nuclear Magnetic Resonance (NMR) Spectroscopy

NMR spectra were obtained on a Jeol ECA-500 NMR for ^1H (500 MHz) and ^{13}C (125 MHz). NMR tubes were prepared using deuterated solvents purchased from Cambridge Isotope Laboratories >95% and sealed by parafilm or using a J-Young needle valve.

Electrochemistry

All electrochemical measurements were obtained on a Gamry 1000E potentiostat and were recorded on Gamry Framework Software (Version 7.02). Analysis of the data was done using Gamry Echem Analyst (Version 7.02). Cyclic voltammetry was performed with a three-electrode setup with a working glassy carbon electrode (3.0 mm), a platinum counter electrode, and a platinum wire as a pseudo-reference electrode.

Electrical Conductivity

Conductivity measurements were taken under inert atmosphere using a homemade device comprised of a thick-walled glass capillary (3 mm inner diameter, 9 mm outer diameter, 36 mm length) with two metal rods (3 mm diameter) compressed with a small trigger clamp.[6] Pellet width measurements were taken with a Mitutoyo 293342-30 Digimatic Outside Micrometer (50.8-76.2 mm) with 0.001 mm resolution. Pellet thicknesses are as follows: **1**, 0.576 mm; **1•C$_{60}$**, 0.706 mm.

Electronic Absorption Spectroscopy

A Cary 300 Bio UV-Visible Spectrometer running Scan v1.00(6) was used to collect the UV-vis spectra with solutions of THF inside of sealed quartz cuvettes to maintain an air free atmosphere. The dried MCOPs with and without C_{60} were run as powdered solids, sealed between two slides, and suspended in bSi-201 quick cure epoxy to prevent oxidation. Backgrounds were taken on a reference sample of epoxy between two slides.

Scanning Electron Microscopy and Energy Dispersive X-ray Spectroscopy

Scanning electron micrographs were obtained on a JEOL JSM-6460LV SEM instrument using a 515kV accelerating voltage while collecting data through the SEM Control User Interface (Version 6.21). Energy dispersive X-ray spectrographs were taken using the built in EDAX and worked up using the APEX software. SEM samples were pumped down and placed on a copper or carbon tape background with a 60 second air exposure while being loaded. During this exposure, samples of **MCOP-1** and **MCOP-2** would occasionally produce smoke from an exothermic reaction. **MCOP1•C_{60}** and **MCOP-2•C_{60}** did not undergo rapid reactions in air to produce smoke.

Single Crystal X-ray Diffraction

Single Crystal X-ray diffraction was performed using an Oxford Diffraction Gemini A Ultra SCXRD. Samples were dried for 30 min by vacuum and suspended in Nujol mineral oil before being transferred to the sampling stage and mounted on loops in a stream of N_2.

Powder X-ray Diffraction

Powder X-ray diffraction patterns were obtained from 11-BM APS Synchrotron Beamline (Bending Magnet Source) at the Argonne National Laboratory (Lemont, Il, USA). X-ray samples were pumped dry, ground by mortar and pestle, and packed into a 1.105 mm outer diameter, 0.1 mm wall Kapton capillary inside a nitrogen glovebox. The capillary ends were then sealed with bSi-201 quick cure epoxy and allowed to cure for at least 24 hours. High resolution synchrotron powder diffraction data were collected using beamline 11- BM at the Advanced Photon Source (APS), Argonne National Laboratory using an average wavelength of $\lambda = 0.4581$ Å. Discrete detectors covering an angular range from 0.5 to 50° 2θ, with data points collected every 0.001º 2θ and scan speed of 0.01º/s.

The powders were rotated during the measurement at ∼50 Hz. The powder patterns were measured at 295 K at beamline 11-BM of the Advanced Photon Source at Argonne National Laboratory using a wavelength of λ = 0.4581 Å, from 0.5 to 50° 2θ with a step size of 0.001° and a counting time of 0.1 s/step.

Here, we show that we can prepare multicomponent assemblies of superatoms through synchronized charge transfer and covalent crosslinking (**Figure 3.1b**). This is facilitated by the serendipitous realization of soluble, superatomic ion-pair precursors that can be dissolved and further manipulated in solution. Specifically, we find that neutral, M_4S_4 (M = Fe, Co) clusters with *N*-heterocyclic carbene (NHC) ligands undergo electron transfer with C_{60} fullerene. The cocrystals can be redissolved and polymerized in the presence of Janus biscarbenes that bridge the M_4S_4 cores. We also demonstrate that neutral M_4S_4 polymers undergo charge-transfer when treated with fullerenes. Both pathways lead to new materials with electrical conductivities greater than the sum of their parts.

Metal-sulfur, cubane-like clusters remain unexplored as precursors for superatomic crystals, despite their natural occurrence[170] and the extensive investigation of their synthetic counterparts. [140] The archetypal Fe_4S_4 clusters, which are analogues of protein-bound redox centers, are particularly appealing donors for this purpose due to their propensity to electron transfer and ability to be prepared with various ligand types.[47, 50, 171-173] For instance, certain all-ferrous $[Fe_4S_4]^0$ cubanes are electron rich and reversibly ionize at potentials suitable for reducing fullerene.[50] We initially selected two, known isostructural $[M_4S_4]^0$ clusters (M = Fe (**1**), Co (**2**) as electron donors, both of which were first reported by Holm and coworkers.[50, 119] These nanoclusters are synthesized in two steps and are isolated with the NHC supporting ligands 1,3-diisopropyl-4,5-dimethylimidazol-2-ylidene ($Pr^i_2NHCMe_2$). It is worth noting that the metal chalcogenide clusters found in superatomic crystals are traditionally passivated with phosphine ligands.[16] We found that M_4S_4 clusters with trialkylphosphine ligands lack the ionization strength to reduce C_{60}. In contrast, NHC-capped Co_4S_4 and Fe_4S_4 clusters spontaneously transfer electrons to fullerene when mixed in solution.

3.3 Results and Discussion

Binary superatomic crystals can be grown by layering saturated toluene solutions of C_{60} fullerene with equimolar mixtures of **1** or **2** in toluene. After 24 hours, long black rods are isolated and washed with toluene (**Figure S1**). Crystals of **2•C$_{60}$** grown from chlorobenzene are suitable for single crystal X-ray diffraction and crystallize in the tetragonal space group $P\tilde{4}n2$. The structure of **2•C$_{60}$** consists of each cluster in a 1:1 ratio with one accompanying molecule of chlorobenzene. The Co_4S_4 and C_{60} units are arranged in segregated columns down the *c*-axis (**Figure 3.2a**). These columns alternate across both the *a* and *b*-axes, respectively (**Figure 3.2b**). Solvent molecules fill the void space around each cluster and alternate in a head-to-tail manner. The fullerides form C_{120} dimers in the solid state, with a single C-C bond between neighboring fullerenes down the stacks. **2•C$_{60}$** crystals obtained from chlorobenzene cannot be redissolved in organic solvents. This is presumably due to the presence of fulleride dimers.

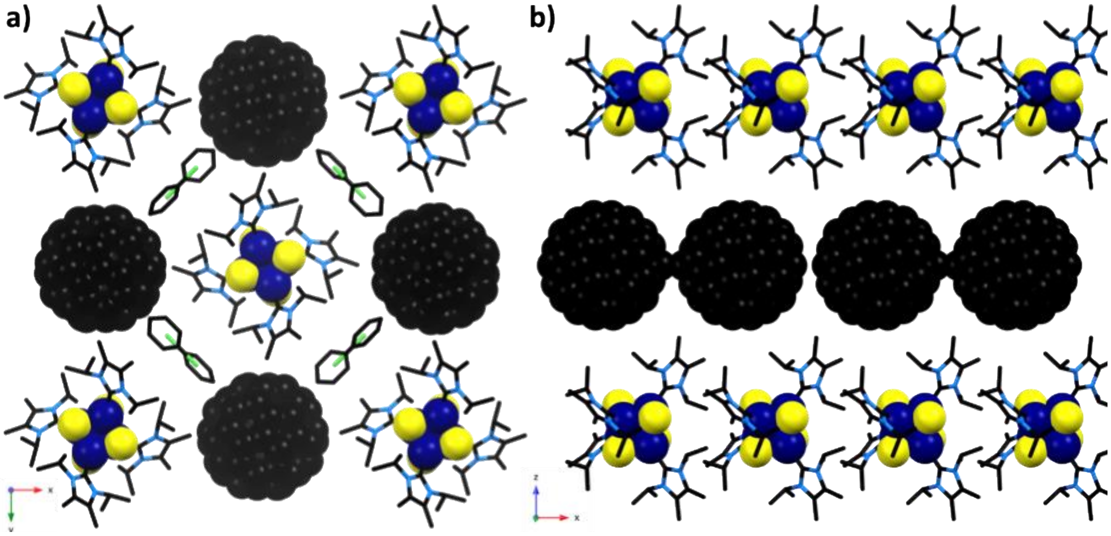

Figure 3.2 Structure of **2•C$_{60}$** showing the crystal packing looking down the *c*-axis (a) and a single layer view down the *b*-axis (b). Hydrogen atoms are removed for clarity. Solvent atoms are omitted in (b). Carbon, black; cobalt, dark-blue; chlorine, green; nitrogen, light-blue; sulfur, yellow.

Charge-transfer between the M_4S_4 nanoclusters and fullerene also occurs in other solvents. For example, mixtures of **1** or **2** in toluene with C$_{60}$ yield long black needles overnight. SEM micrographs of **1•C$_{60}$** show rod-like crystals of 50-75 µm length (**Figure S2**). Single crystal X-ray data for **1•C$_{60}$** was not obtained, but powder X-ray diffraction studies confirm that the material is crystalline (**Figure S3**). The elemental composition of the cocrystals was also determined using EDS (**Figure S4**). The spectra of **1•C$_{60}$** contain C, N, Fe, and S throughout the crystals with the expected equivalent ratio of metal to sulfur.

Remarkably, cocrystals of **1•C$_{60}$** and **2•C$_{60}$** prepared from toluene can be redissolved in several organic solvents, including, dimethyl sulfoxide, *o*-dichlorobenzene (*o*-DCB), tetrahydrofuran (THF), and 1-methylnaphthalene (**Figures 3.3b** and **S5**). Thus, the superatomic ion pairs can be characterized in solution using electrochemical analysis and common spectroscopic methods. The solubility of these materials is unique for

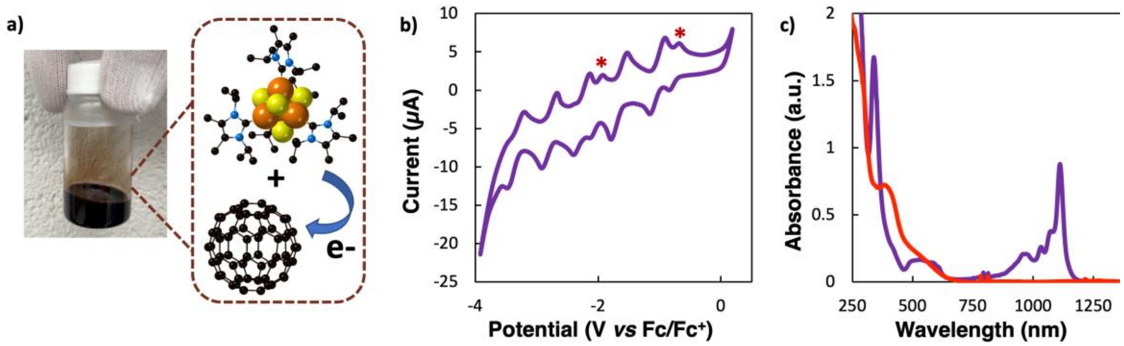

Figure 3.3 Characterization of **$1 \bullet C_{60}$**. (a) Photograph of **$1 \bullet C_{60}$** in *o*-DCB and graphical depiction of cluster electron transfer. (b) Cyclic voltammogram of **$1 \bullet C_{60}$** recorded at 100 mV s^{-1} in THF with $TBAPF_6$ using a glassy carbon working electrode. (c) UV-Vis-NIR spectra of **1** (red) and **$1 \bullet C_{60}$** (purple) in THF.

fulleride-cluster superatomic crystals. In fact, we are aware of only one other related example of a soluble cluster-fulleride superatomic compound: a binary material of [6,6]-phenyl-C_{61}-butyric acid methyl ester (PCBM) and $Co_6Te_8(PPr_3)_6$.[174]

The electrochemical properties of **$1 \bullet C_{60}$** and **$2 \bullet C_{60}$** were investigated using cyclic voltammetry (CV) (**Figure 3.3c**). Solutions of **$1 \bullet C_{60}$** in THF undergo seven reversible redox events across a range of three-volts. Five of these waves correspond to fullerene-based reductions.[175] We are unable to detect the sixth C_{60} reduction in our solvent system at room-temperature. The two additional waves in the voltammogram of **$1 \bullet C_{60}$** at $E_{1/2}$ = -0.74 V and -2.0 V *vs.* Fc/Fc^+ are assigned to the oxidation of the Fe_4S_4 core. [50] These values are consistent with the measured oxidations of the neutral Fe_4S_4 cluster **1**, which occur at $E_{1/2}$ = -0.80 V and -2.0 V (**Figure S6**). The CV of **$2 \bullet C_{60}$** in THF also exhibits redox events for both the fullerene and cluster **2** (**Figure S7**). The M_4S_4 oxidation peaks of **$2 \bullet C_{60}$** occur at higher potentials ($E_{1/2}$ = -0.38 V and -1.63 V) than **$1 \bullet C_{60}$**. This is expected, as Fe congener **1** is more electron-rich than the Co analogue **2**. [119] Such rich electrochemistry confirms the presence and structural integrity of both the metal-sulfur cluster and C_{60} in these soluble ionic cluster pairs.

The degree of charge transfer between clusters in **1•C_{60}** and **2•C_{60}** was obtained spectroscopically. Electronic absorption spectroscopy was first used to probe the oxidation state of the fullerenes. Each fullerene redox state is known to have signature absorbance features in the near-infrared (NIR) region that are cation and solvent independent.[176] The UV-vis-NIR spectrum of **1•C_{60}** in THF has a strong NIR transition at *ca*. 1115 nm with two additional overlapping, higher energy bands and a fourth feature at 973 nm (**Figure 3.3c**). The shape of the absorbances in the NIR region and the values of the two main peaks are consistent with a C_{60}^{-1} oxidation state. Specifically, reported spectra of fulleride anions exhibit a dominant peak around 1100 nm and a higher energy transition between 930 and 995 nm.[176] We measured a near-identical UV-vis-NIR spectrum for **2•C_{60}** in THF with the fulleride features blue-shifted to 1103 nm and 953 nm, respectively **(Figure S8**).

Nuclear magnetic resonance (NMR) spectroscopic studies of the dissolved superatomic crystals were performed to further probe oxidations states of the constituent clusters in solution. The neutral and oxidized forms of parent cluster **2** have distinctive ^{1}H-NMR spectra.[119] Thus, NMR experiments were carried out on solutions of **2•C_{60}**. The ^{1}H-NMR spectrum of **2•C_{60}** in chlorobenzene-d_5 includes a broad singlet at 10.5 and second peak at 8.58 ppm (**Figure 3.4a**). These two peaks correspond to methyl protons attached to the imidazolylidene and the methyl protons of the isopropyl groups, respectively. We observe that both peaks are noticeably shifted downfield from the NMR spectrum of the neutral cluster **2** (**Figure 3.4b**). Furthermore, the chemical shifts of these

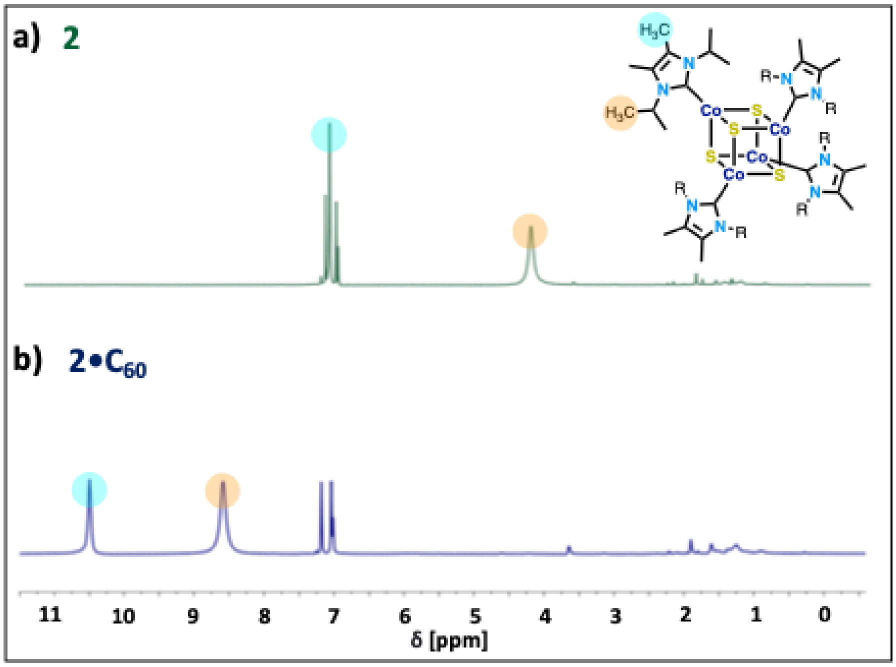

Figure 3.4 NMR spectroscopy studies of **2•C$_{60}$**. (a) ^{1}H NMR spectra of **2** and (b) **2•C$_{60}$** in chlorobenzene-*d*$_5$. All spectra recorded at 500 MHz.

resonances move toward those observed in the NMR spectrum of the oxidized cluster **2•PF$_6$** in CD$_3$CN (δ 11.75 and 9.53). [119] We therefore conclude that the oxidation state of the M$_4$S$_4$ entity is +1 in **2•C$_{60}$**. In accordance, the ^{13}C-NMR of **2•C$_{60}$** also has a broad peak centered at 183 ppm, which reflects the presence of C$_{60}^{-1}$ (**Figure S9**). [176] A comparable broad peak at 185 ppm was also observed in the ^{13}C-NMR spectrum of **1•C$_{60}$** (**Figure S10**). Notably, the carbon-NMR experiments were run for 24 hours, underscoring the stability of the ionic species in solution.

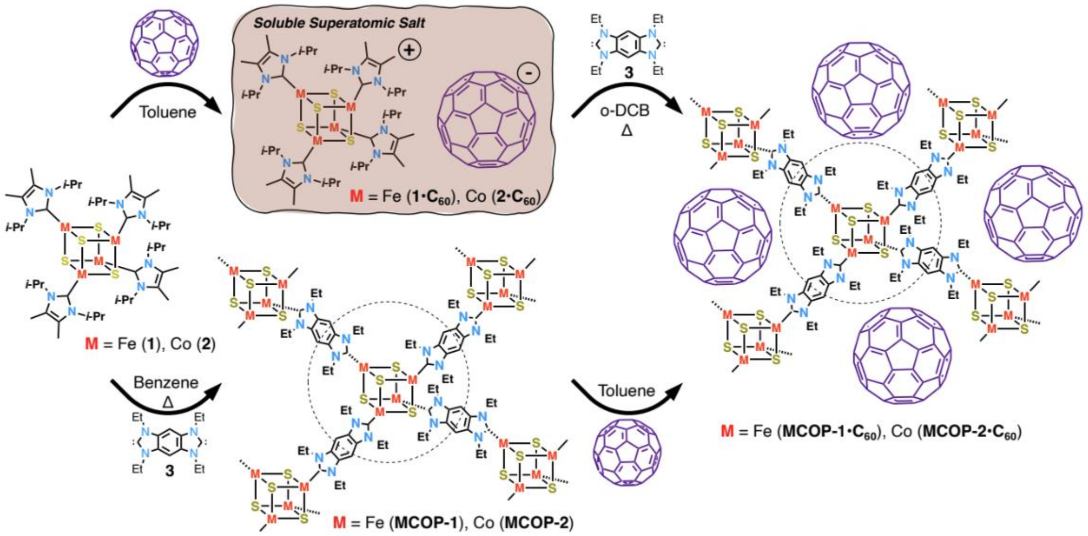

Figure 3.5 Synthesis of M_4S_4•C_{60} superatomic crystals, organometallic polymers, and superatomic organometallic polymers.

The inherent solubility of the M_4S_4•C_{60} superatomic crystals prompted us to investigate their use as reactants for further synthetic transformations (**Figure 3.5**). Our group recently reported that parent Co_4S_4 clusters can be crosslinked with Janus-biscarbenes to generate multidimensional, main-chain organometallic polymers (MCOPs).[149] Thus, we anticipated that the M_4S_4 entities in **1•C_{60}** and **2•C_{60}** could also be assembled under similar reaction conditions to yield MCOPs with accompanying fulleride units. We first investigated the polymerization of **2•C_{60}**, adapting our synthetical protocol for **MCOP-2**. Solutions of **2•C_{60}** in *o*-DCB were mixed with benzo-bis-imidazolylidene **3** and heated in a sealed tube at 100º C (**Figure 3.5**). After 48 hours, the solution was clear, and a dark-colored precipitate was isolated by centrifugation inside a nitrogen-filled glovebox. SEM micrographs reveal that **MCOP-2•C_{60}** exhibits a similar morphology as **MCOP-2** (**Figure S11**). The solid-state UV-Vis-NIR absorption spectrum of **MCOP-2•C_{60}** includes features of the Co_4S_4-MCOP at *ca.* 500 nm and the fulleride between 900 and 1100 nm (**Figure S12**).

The successful co-polymerization of **2•C_{60}** and **3** motivated us to explore the synthesis of the iron-sulfur analogue. However, the polymer absent-fulleride (**MCOP-1**) was not reported in our previous manuscript. Here, details are provided for its preparation and characterization. (See Supporting Information). **MCOP-1** is a deep-blue solid. This polymer was subject to the same characterization methods as for **MCOP-2 (Figures S13-16**). We note that the solid-state UV-vis spectrum of **MCOP-1** is red-shifted compared to **1**. The shift of the λ_{max} to lower energy is ascribed to the increase in conjugation of the biscarbene-linked polymer compared to the discrete cluster. A similar shift of the λ_{max} to lower energy is also observed when **2** is covalently crosslinked by **3**. [149] Finally, we chemically disassembled the polymer to verify the presence of the Fe_4S_4 cluster in **MCOP-1**. Formation of **MCOP-1** is reversible and depolymerization occurs upon addition of excess monocarbene ($Pr^i{}_2NHCMe_2$) in a similar fashion to **MCOP-2**. [149] Likewise, NMR studies corroborate that the intact, neutral Fe_4S_4 cluster **1** can be chemically extruded from the solid (**Figure S16**).

Formation of **MCOP-1•C_{60}** was accomplished using the protocol for **MCOP-2•C_{60}**. A dark black solid forms rapidly when **1•C_{60}** is heated in *o*-DCB with **3**. Presence of fulleride in **MCOP-1•C_{60}** was again corroborated via absorbance spectroscopy (**Figure S17**). Fullerene incorporation can also be achieved post-synthetically by treating suspensions of neutral **MCOP-1** or **MCOP-2** in toluene with solutions of C_{60} fullerene (**Figure S18**). Charge-transfer can be monitored visually with the naked-eye. Dark, purple-colored solutions of fullerene in toluene are clear after 24 hours of exposure to the solid MCOPs (**Figure S19**).

We measured the electrical conductivity on pressed pellets of the individual clusters, superatomic crystals, and MCOPs with and without fulleride. Measurements were carried out using a two-point probe apparatus under nitrogen.[177] We observe that MCOP materials are more conductive than the precursor clusters by several orders of magnitude (**Figure 5** and **Table 1**). A similar trend was also shown by Brozek and coworkers, who recently reported large increases in conductivity through the linear polymerization of $Fe_4S_4^{2+}$ clusters and bis(NHCs). [31] In addition, cocrystals **1•C$_{60}$** and **2•C$_{60}$** are also considerably more conductive than the precursor clusters. Similar gains in conductivity have been observed in related superatomic solids comprising fullerides. [38, 136, 141] The incorporation of fulleride results in further conductivity enhancements for both the cobalt and iron MCOPs. Specifically, the polymers prepared from **1•C$_{60}$** and **2•C$_{60}$** are 40 and 1,500 times more conductive, respectively than the parent MCOPs (**Table 1**). MCOPs soaked in fullerene solutions also exhibit conductivities approaching that of the polymers prepared from superatomic ion pairs (**Figures 3.6** and **S20**). We surmise that fulleride is more thoroughly integrated into the polymers when the binary cocrystals are used as precursors. Both cobalt and iron materials in this series exhibit similar trends in conductivity. Superior electrical conductivities in both cases arise from the synergistic effects of covalent crosslinking and fulleride doping. We cannot rule out that the lower conductivities of the iron based MCOPs may arise from defects due to the well-known cluster aggregation of the Fe_4S_4 cubane which is easily reversed in the presence of excess NHC ligands as is present in the depolymerization experiment used to confirm the presence of the cubane.

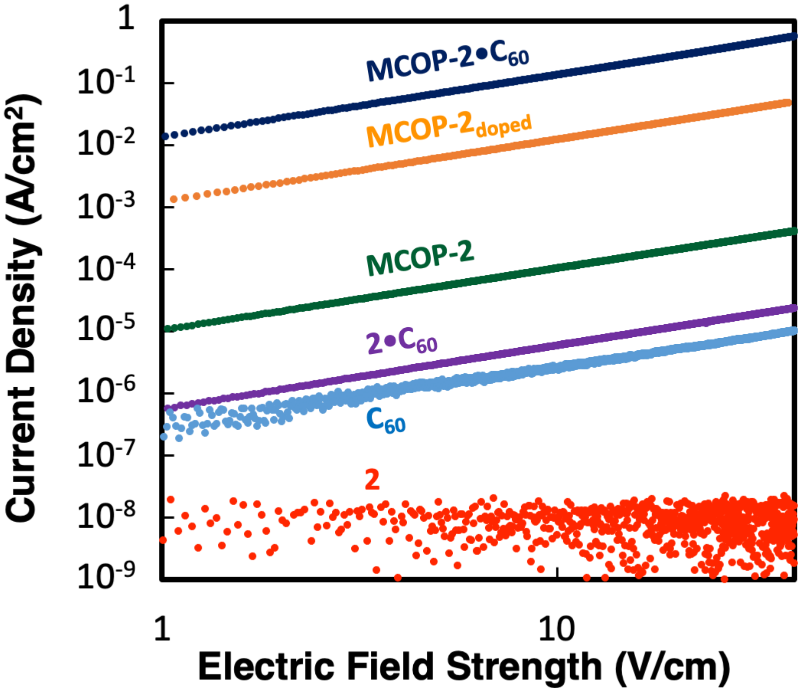

Figure 3.6 Electrical properties of pressed pellets. Plots of current density versus electric field strength (*J*–*E*) curves at 297 K.

Table 1. Electrical Conductivities of Clusters, Cocrystals, and MCOPs in (mS/cm).

Material	***1*** *M=Fe*	***2*** *M=Co*
$M_4S_4(NHC)_4$[a]	6.01×10^{-7}	1.94×10^{-7}
$M_4S_4(NHC)_4$ •C60	2.28×10^{-4}	5.93×10^{-4}
MCOP	3.10×10^{-5}	1.04×10^{-2}
MCOP•C60 (doped)	7.47×10^{-4}	1.24
MCOP•C60	1.24×10^{-3}	16.1

[a] The high electrical resistivities of 1 and 2 inhibited the accurate determination of conductivities with certainty.

Finally, we prepared **MCOP-2•BF$_4$** to decouple the oxidation state of the cluster from the impact of fullerene on the electrical properties of the polymer. Pressed pellets of **MCOP-2•BF$_4$** are approximately 15 times more resistive (7×10^{-4} mS/cm) than that of **MCOP-2** (**Figure S21**). Thus, we conclude that oxidation of the cluster does not independently improve conductivity in the MCOPs and that the presence of fulleride is critical for effective charge-transport in these materials. Charge transfer with fullerene alone, however, is insufficient for achieving high conductivities. This is corroborated by the mediocre performance of cocrystals **1•C$_{60}$** and **2•C$_{60}$**, which contain fulleride but are not crosslinked.

3.4 Conclusions

In summary, all-ferrous Fe_4S_4 clusters and their cobalt-analogues were found to spontaneously reduce C_{60} fullerene to yield solution processible superatomic ions. The unprecedented solubility of these cluster ion pairs allows us to characterize them in both the solution and the solid state. Furthermore, the superatomic solutes can be covalently polymerized when treated with rigid, bis(NHC) ligands. The resulting ternary materials comprise cluster units that are covalently and ionically coupled. This gives rise to electrical conductivity properties that far surpass those of the discrete building blocks and of the materials assembled from only through-bond or charge-transfer interactions. We envision that this dual-assembly approach may be applied to other superatomic materials to enhance electronic coupling between clusters.

The investigation of different cluster linkers, as well as various metal-chalcogenide and fullerene precursors, are currently being studied in our laboratory. Recent isolation of an isocyanide stabilized Co_4S_2 with multiple reversible oxidations states (**Figure 3.7**) is being investigated for polymerization of a 3D network based on the precedent of our collaborators in the Pedersen group. [159] To date our main-chain organometallic polymers have struggled to obtain high crystallinity like many of the early MOFs assembled from single-metal ions and neutral donating linkers. In the realm of single metal ions, single crystals have been achieved using ZIFs with negatively charged imidazolate linkers and tetrahedrally coordinating M^{+2} ions through solvothermal chemistry. The tetrahedrally coordinating $Fe_4S_4^{+2}$ cubane cluster can be isolated and is currently under investigation using similar synthetic techniques.

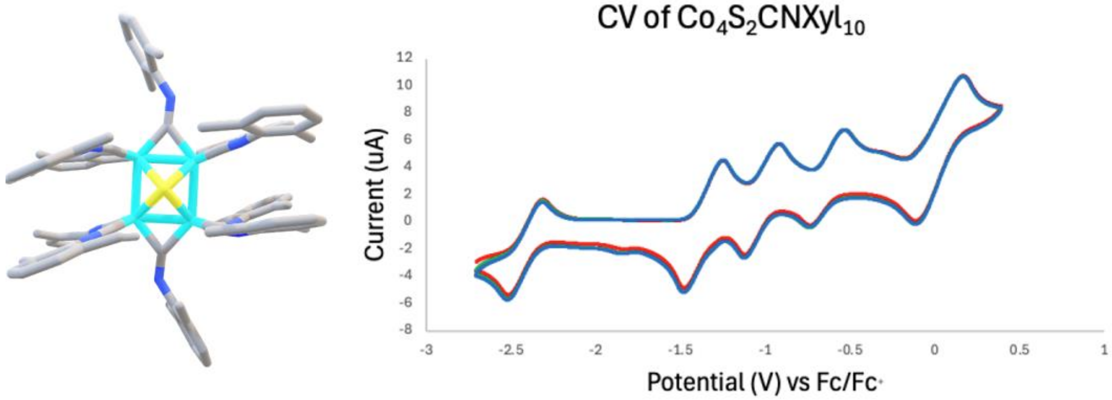

Figure 3.7 Single crystal x-ray structure of Co_4S_2(2,6-dimethylphenyl isocyanide)$_{10}$ with hydrogens omitted along with its CV measurements.

3.5 Appendix B: Chapter 3 Supplementary Information

3.5.1 SEM Micrographs of $\mathbf{1 \bullet C_{60}}$ and $\mathbf{2 \bullet C_{60}}$

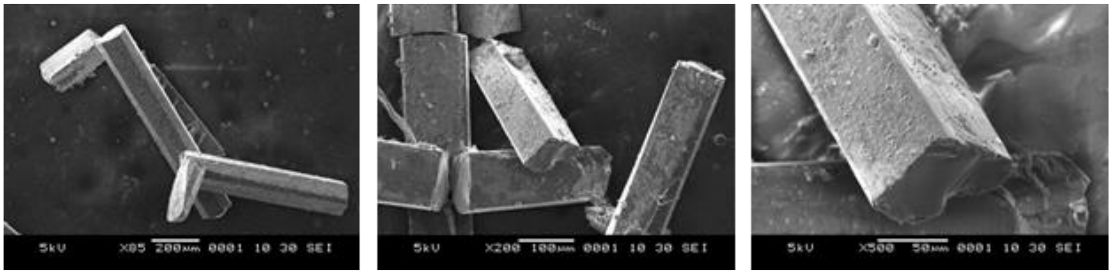

Figure S1. SEM micrographs of single crystals of $\mathbf{2 \bullet C_{60}}$ grown from chlorobenzene.

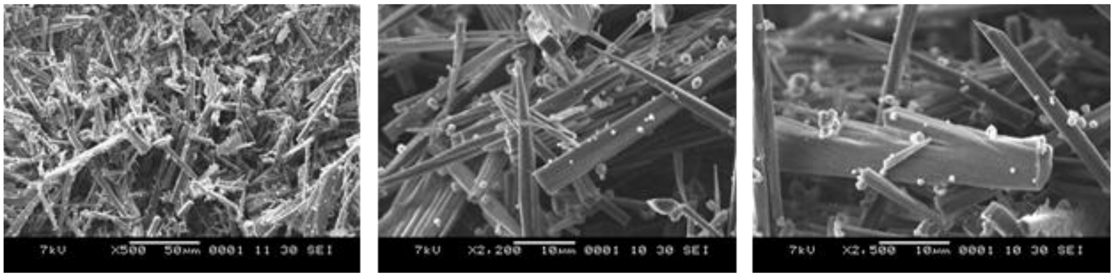

Figure S1. SEM micrographs of single crystals of $\mathbf{2 \bullet C_{60}}$ grown from chlorobenzene.

3.5.2 Powder X-ray Diffraction

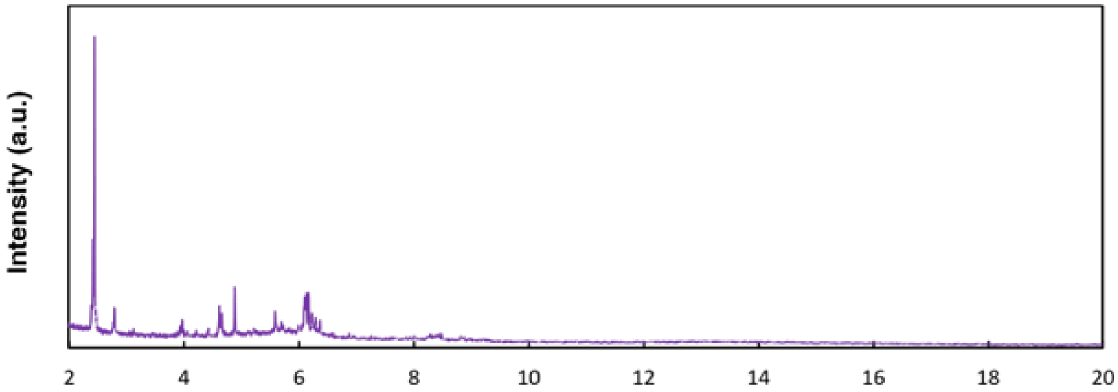

Figure S3. Synchrotron powder X-ray diffraction pattern of $1 \bullet C_{60}$

3.5.3 Energy dispersive X-ray spectrograph of 1•C_{60}

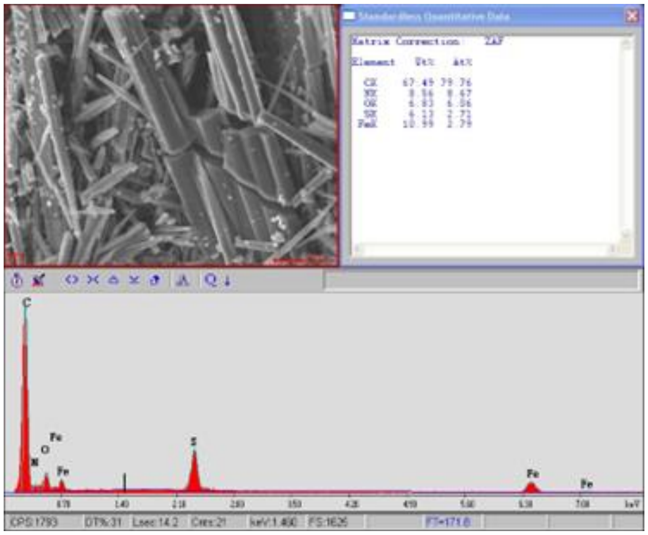

```
Matrix Correction    ZAF

Element    Wt%    At%

  CK     67.49  79.76
  NK      8.56   8.67
  OK      6.83   6.06
  SK      6.13   2.71
 FeK     10.99   2.79
```

Figure S4. EDS survey scan and elemental composition of 1•C_{60}. The spectrum was collected using carbon tape as a background.

3.5.4 Photographs of Dissolved Superatomic Crystals 1•C_{60}

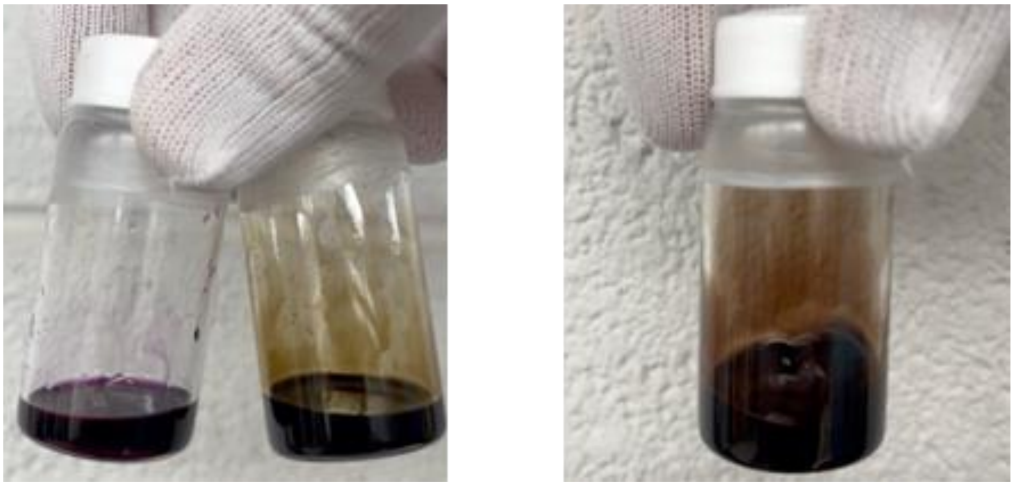

Figure S5. Images of C_{60} and 1 dissolved in *o*-dichlorobenzene before mixing (left) and one hour after mixing (right).

3.5.5 Electrochemical analysis of 1•C$_{60}$ and 2•C$_{60}$

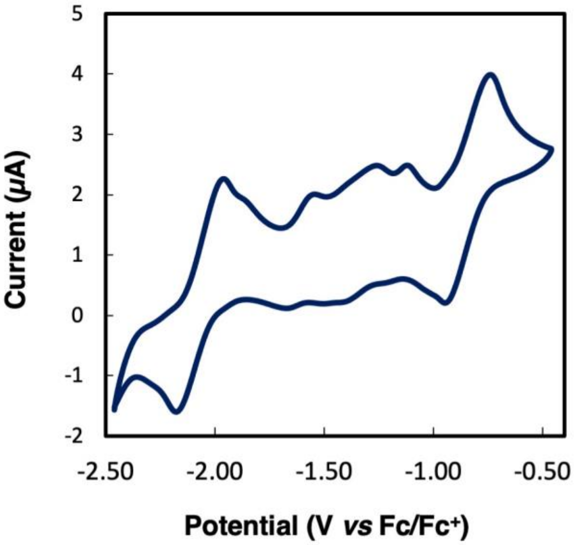

Figure S6. Cyclic voltammogram of **1** (5 mM) in THF measured with a glassy carbon working electrode, Pt counter electrode, and Pt-wire pseudo-reference electrode. Measured at 100 mV/s with TBA-PF$_6$ as the supporting electrolyte.

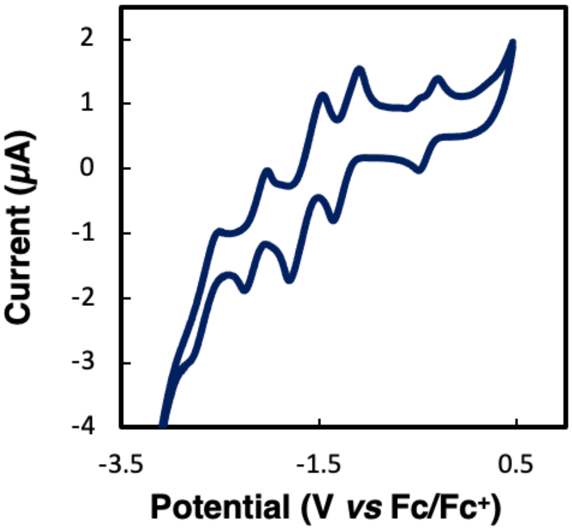

Figure S7. Cyclic voltammogram of **2•C$_{60}$** recorded at 25 mV s^{-1} in THF with TBAPF$_6$ using a glassy carbon working electrode, Pt counter electrode, and Pt-wire pseudo-reference electrode.

3.5.6 UV-Vis-NIR Absorption Spectroscopy of 2•C_{60}

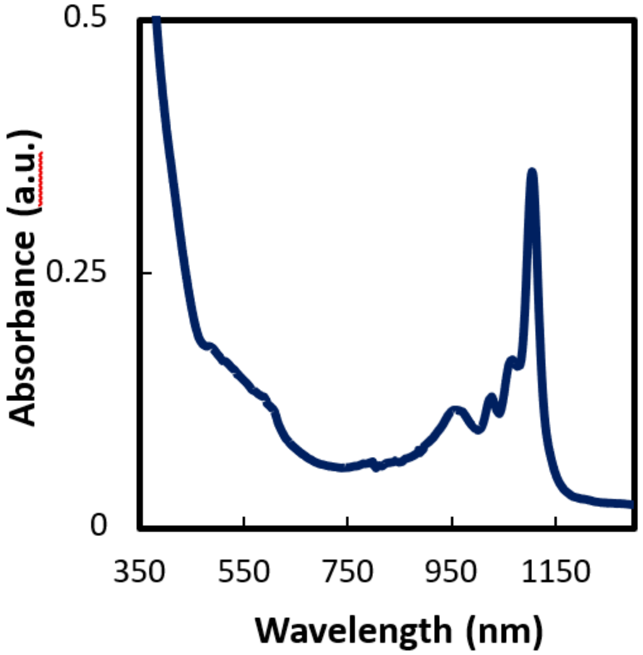

Figure S8. UV-vis absorption spectra of **2•C_{60}** in *o*-dichlorobenzene**.**

3.5.7 NMR Spectroscopy of Dissolved Superatomic Crystals.

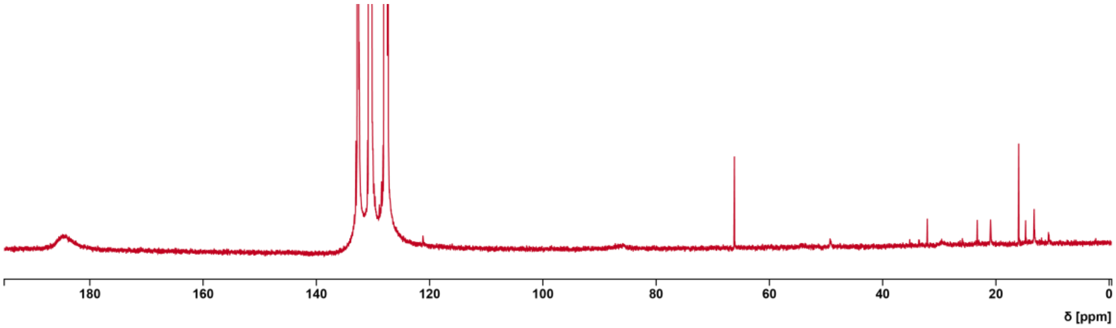

Figure S9. ^{13}C NMR spectrum of **2•C_{60}** in chlorobenzene-d_5 recorded at 500 MHz.

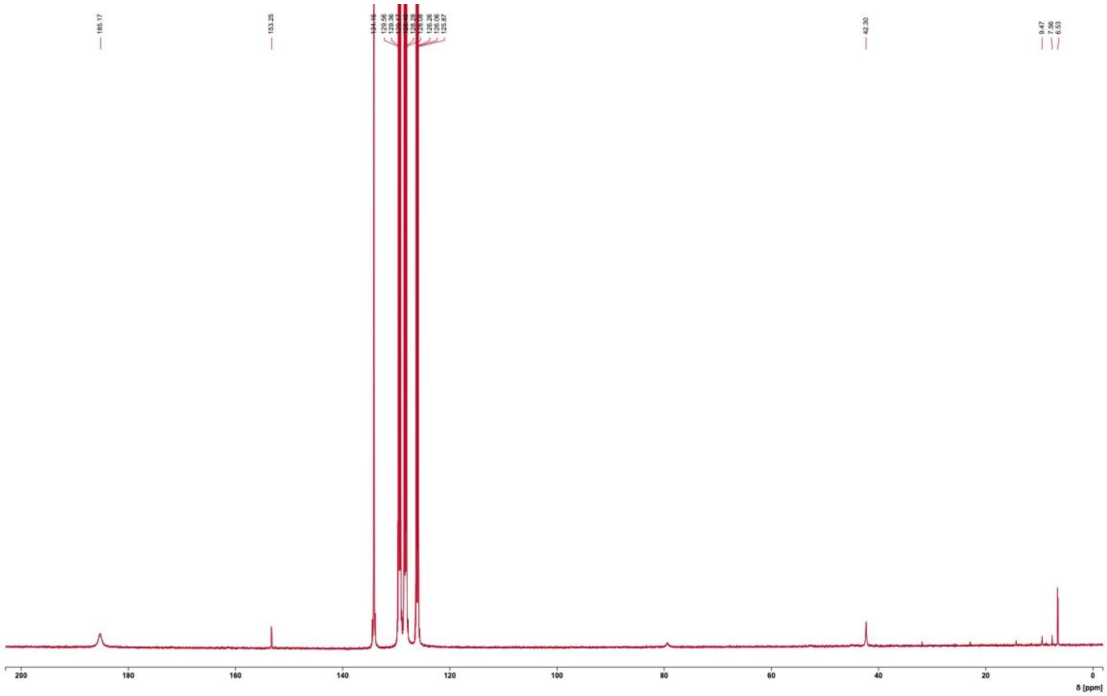

Figure S10. ^{13}C NMR spectrum of **1•C$_{60}$** in chlorobenzene-*d*$_5$ recorded at 500 MHz.

3.5.8 Scanning Electron Micrograph and EDS Survey of MCOP-2•C$_{60}$

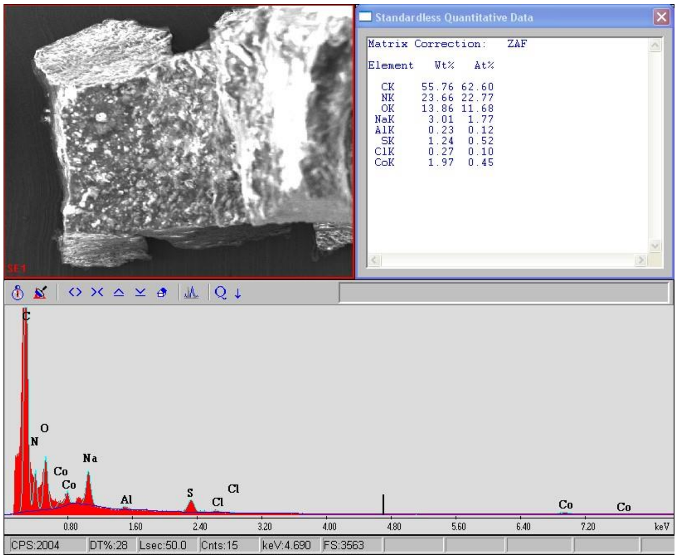

```
Matrix Correction:    ZAF

Element    Wt%    At%

   CK     55.76 62.60
   NK     23.66 22.77
   OK     13.86 11.68
  NaK      3.01  1.77
  AlK      0.23  0.12
   SK      1.24  0.52
  ClK      0.27  0.10
  CoK      1.97  0.45
```

```
CPS:2004  DT%:28  Lsec:50.0  Cnts:15  keV:4.690  FS:3563
```

Figure S11. SEM micrographs of MCOP-2•C$_{60}$.

3.5.9 UV-Vis Absorption Spectroscopy of MCOP-2•C_{60}

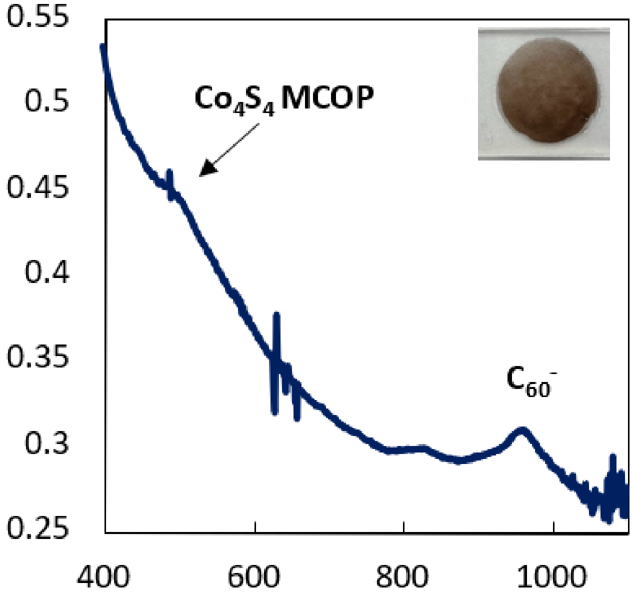

Figure S12. UV-vis absorption spectrum of **MCOP-2•C_{60}** (inset image **MCOP-2•C_{60}** in epoxy).

3.5.10 Characterization of MCOP-1

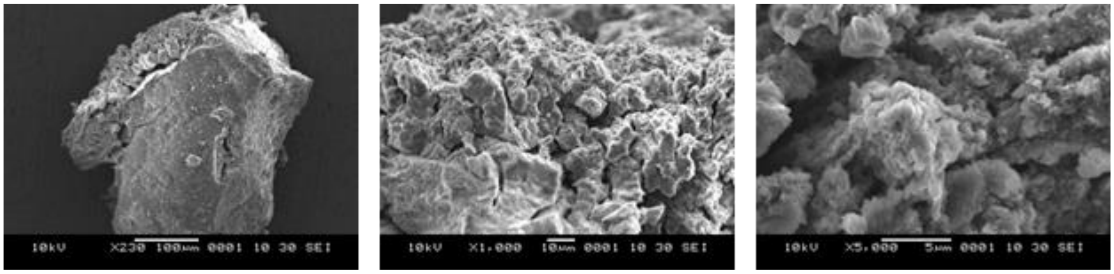

Figure S13. SEM micrographs of **MCOP-1**.

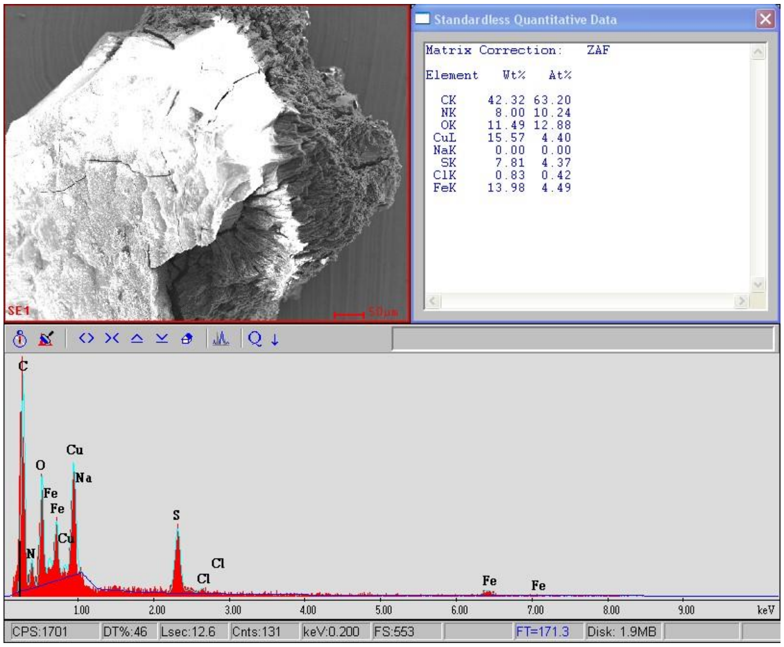

```
Matrix Correction:   ZAF

Element    Wt%    At%

  CK     42.32 63.20
  NK      8.00 10.24
  OK     11.49 12.88
 CuL     15.57  4.40
 NaK      0.00  0.00
  SK      7.81  4.37
 ClK      0.83  0.42
 FeK     13.98  4.49
```

Figure S14. EDS survey scan and elemental composition of **MCOP-1** collected using copper tape as a background.

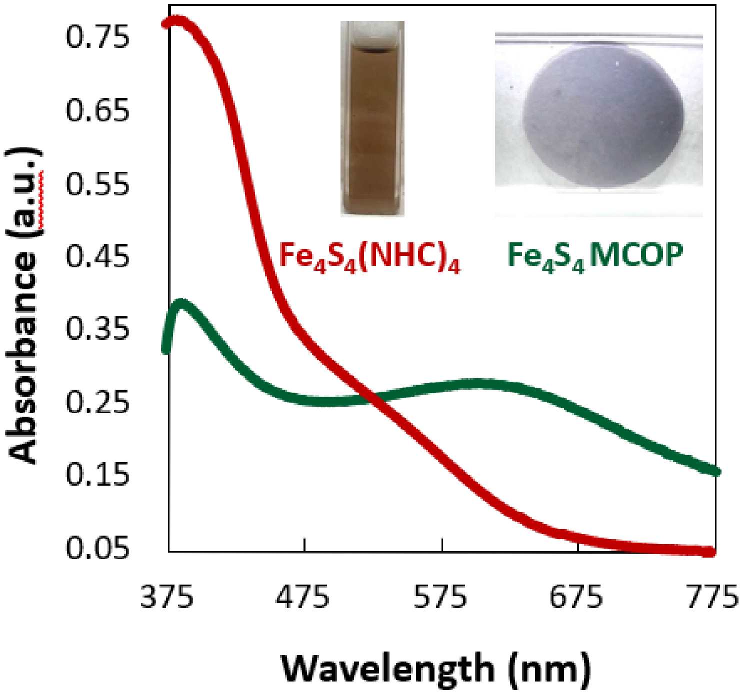

Figure S15. Normalized UV-vis absorption spectra of **1** and **MCOP-1** (inset images of a solution of **1** in THF and **MCOP-1** in epoxy).

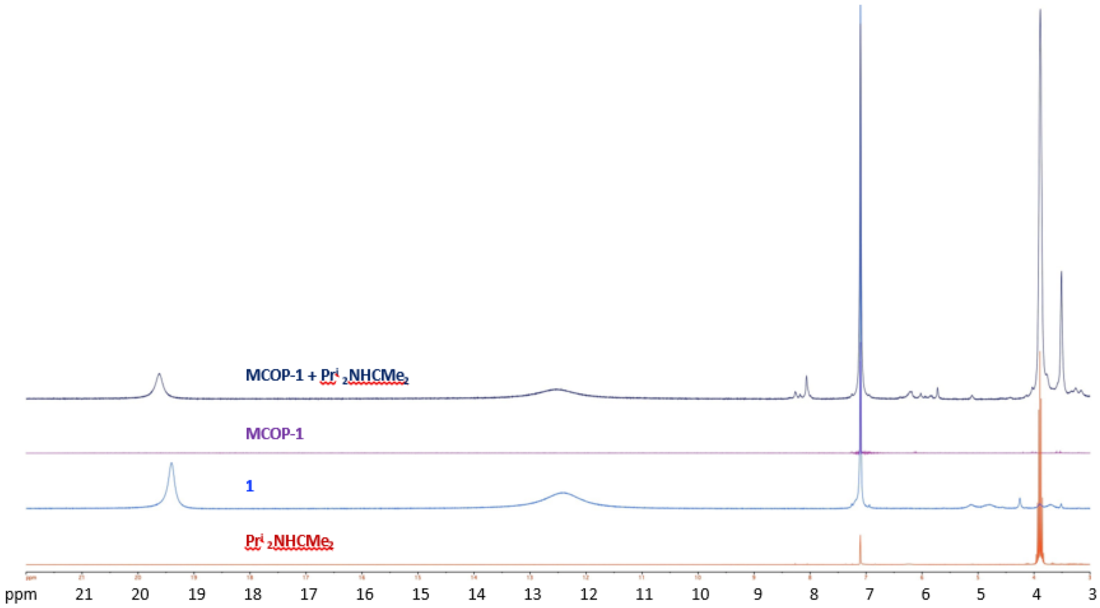

Figure S16. Digestion Studies of **MCOP-1**: NMR spectra overlay of **MCOP-1** (purple); cluster **1** (light blue); ligand $\mathrm{Pr^{i}{}_{2}NHCMe_{2}}$ (red); and mixture of **MCOP-1** and $\mathrm{Pr^{i}{}_{2}NHCMe_{2}}$ after digestion (dark blue) in C_6D_6.

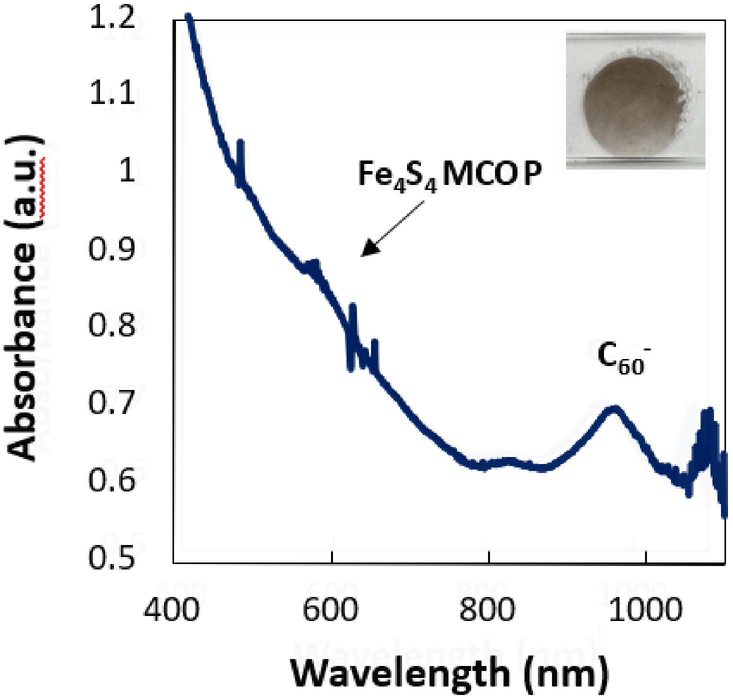

Figure S17. UV-vis absorption spectrum of **MCOP-1•C$_{60}$** (inset image **MCOP-1•C$_{60}$** in epoxy).

3.5.11 UV-vis-NIR studies of MCOPs Postsynthetically Doped with Fullerene.

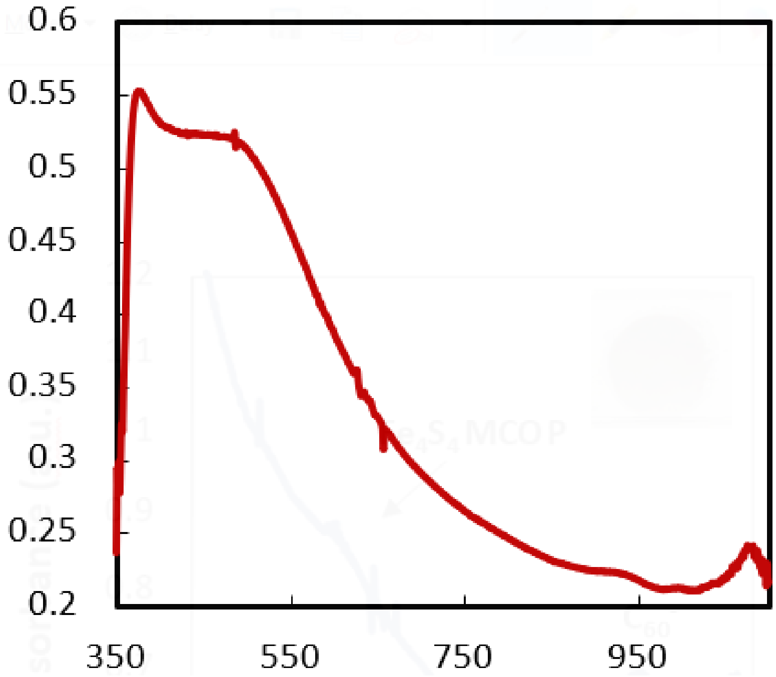

Figure S18. UV-vis-NIR spectrum of **MCOP-2** after soaking in a saturated solution of C_{60} for 24 hours. The spectrum was collected on the polymer, which is sealed in epoxy between two glass slides to protect the sample from air exposure. Inset shows an image of the sample.

3.5.12 Images of MCOP Postsynthetically Doped with Fullerene.

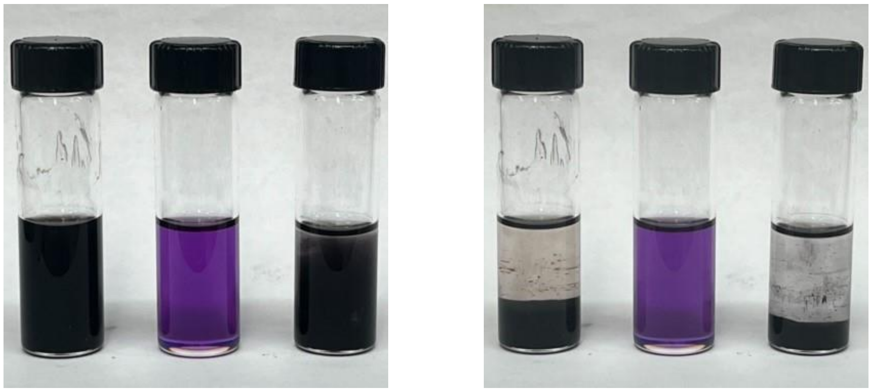

Figure S19. (Left photo) Initial photographs of **MCOP-2** suspended in a solution of toluene with C_{60} (left), C_{60} in toluene (middle), and **MCOP-2** in toluene (right). (Right photo) Photograph of the same solutions 24 hours later.

3.5.13 Electrical Conductivity Measurements

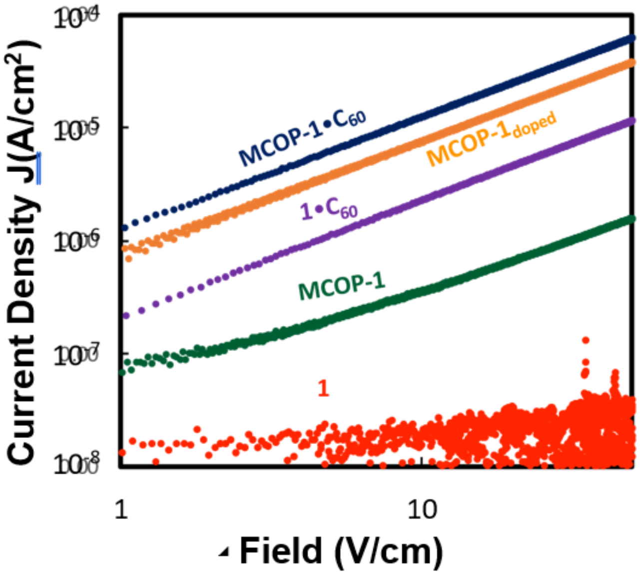

Figure S20. Electrical properties of pressed pellets of Fe-based materials. Plots of current density versus electric field strength (*J*–*E*) curves at 297 K.

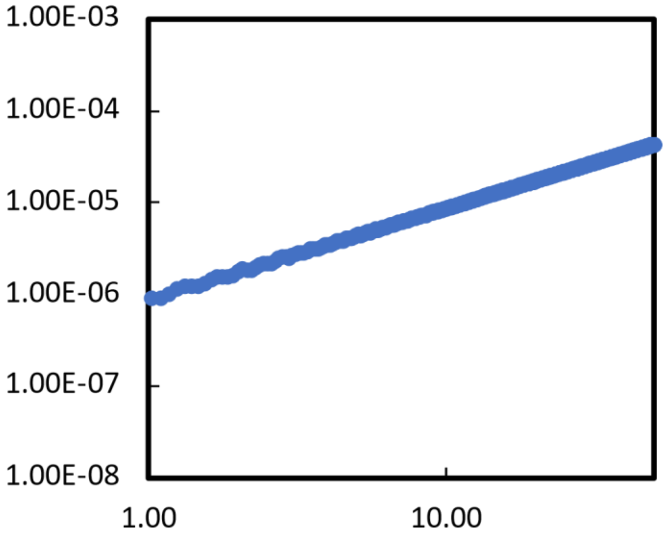

Figure S21. Electrical properties of pressed pellets of **MCOP-2•BF$_4$**. Plots of current density versus electric field strength (*J*–*E*) curves at 297 K.

3.5.14 X-ray Diffraction Procedures and Tables

X-ray diffraction data were collected using an Agilent/Oxford Diffraction Gemini A Ultra diffractometer. The diffractometer was equipped with a sealed-tube Mo source with a graphite monochromator (λ=0.71073 Å) and a sealed-tube Cu source with graphite focusing optics (λ=1.54184 Å). In all cases data were collected to better than 0.8 Å resolution.

The CrysAlisPro diffractometer software[7] provided intensity data corrected for Lorentz, polarization, and absorption effects. Preliminary structure solutions were found with the AutoChem software package[7]. Final structures were solved with SHELXT[8] (direct methods) and refined with SHELXL[9], using the Olex2 software package[10]. Anisotropic refinement for all nonhydrogen atoms was performed except where noted. Hydrogen atoms were placed in calculated positions.

The crystal structure refinement for **2•C_{60}** was complex because the fullerene is disordered over a fourfold symmetry element. Refinement details are given in the cif file (_refine_special_details). Briefly, the geometry for the disordered C_{60} fragment was introduced from a reference structure and the orientation was identified by a Monte Carlo search. Subsequently the geometry was relaxed with the aid of DFIX restraints on all 1,2- and 1,3- distances.

Publication tables and graphics were generated with the WinGX[11] suite of programs.

Table S1 Crystal data and structure refinement for 2•C_{60}.

Compound	**2·C_{60}**
Formula	$C_{128}H_{100}Cl_4Co_4N_8S_4$
MW	2255.91
Space group	*P*-4*n*2
a **(Å)**	23.2168(7)
b **(Å)**	23.2168(7)
α **(°)**	90
β **(°)**	90
γ **(°)**	90
V **(Å^3)**	5173.9(3)
Z	2
ρ_{calc} (g cm^{-3})	1.448
λ (Å)	0.71073
T **(K)**	108
d_{min} (Å)	0.72
μ(mm^{-1})	0.872
Data	6442
Restraints	415
Parameters	510
R_1(obs) (%)	5.09
R_1(all) (%)	6.29
S	1.065
Peak, hole (e$^-$ Å^{-3})	.52, -.38

CHAPTER 4: COMPUTATIONAL SCREENING OF [3]RADIALENES FOR REDOX FLOW BATTERIES

4.1 Introduction

We applied DFT calculations to the series of asymmetric, ester-substituted, [3]radialenes and their theoretical dimers.[178] The ground state of these dimers are inherently difficult to elucidate since they have many unique dimer conformations with which they readily converge on local minima. Further these minima are highly solvent, concentration, counterion, and temperature dependent. Dimerization is a known occurrence for many carbon-centered radicals.[179] [3]Radialene radical anions have been shown to undergo both σ- and π-dimerization with the former introducing solubility problems and electrochemical irreversibility.[178] For these radical anions, dimers seem to be especially common at high concentration in aqueous environments, which is a necessary condition for an aqueous redox flow battery (RFB).[32] If a molecule is to be stored as a carbon-centered radical in an RFB than it is critical to avoid σ-dimers by synthetically or environmentally disfavoring their formation. Convention dictates planar radicals that are electronically delocalized favor pimer formation. Steric hindrance is often used to prevent dimerization altogether, but in systems such as radical dimers with elongated bonds the effect of London dispersion effects are often underestimated and sterics may unintentionally promote dimerization.[65-67] For RFB applications, σ-dimer formation prevents stable charge–discharge cycling. However, strong σ-dimers are of interest for unrelated applications, such as reversible bond formation in polymers. Therefore, it was important to try to elucidate the driving force of these dimerization modes to design [3]radialenes for specific applications. This initial computational dimer investigation inspired the ongoing development of computational screening criteria of [3]radialene derivatives for RFBs.

Solubility, redox potential, and stability make up the three-legged stool of an effective active RFB species for energy storage. Solubility and redox potential directly control the available energy density for a redox flow cell while stability is critical to longevity and cyclability. Any one of these three properties being insufficient can invalidate a candidate as a suitable active electrolyte (**Figure 4.1**).[180] Due to the complex nature of both electrochemical and chemical stability, computational screening of stability is a difficult and time-consuming prospect, but nonetheless a critical one. Since all three legs of the stool are necessary, identifying any one property as sufficiently lacking provides an effective screening method for removing molecules from the pool of potential candidates. By calculating computationally less expensive properties first, such as redox potential, the pool of candidates can be narrowed down substantially before further computational investigation of electrochemical and chemical stability with only the best candidates being proposed for synthesis. [3]Radialenes are absent from the molecular databases often used in machine learning. The unique electronics of these molecules makes it unlikely machine learning could make accurate predictions of them since they are notably different from redox active molecules in the current training sets. This is another reason the synthetic and computational research of these molecules is necessary. To screen hundreds of potential candidates manually with limited resources it was necessary to find accurate, but computationally inexpensive, methods to elucidate key markers for stability and redox potential. This investigation is ongoing, but this section will cover the principles that have been found to be constructive.

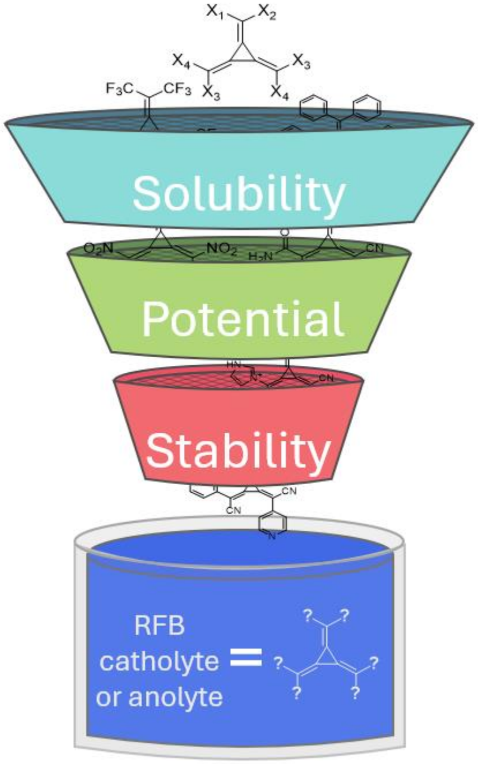

Figure 4.1 Visual representation of the multi-step screening process in which [3]radialene candidates for aqueous redox flow battery may be removed from a larger pool with successively more computationally intensive filters.

4.2 Experimental

We performed a geometry optimization and subsequent frequency calculation using (ωB97DX/6-311+G(d,p), SMD) in gas and with implicit water solvation to better understand the dimerization modes of the -ester series of [3]radialene derivatives.[178] The same optimization parameters were used for other stability calculations including other solvent parameters as necessary. We investigated the energies of possible π-dimers and σ-dimers to help predict radical dimerization, largely based on the computational precedent of Winter.[181] The current functional has been shown to reproduce binding energies within 3 kcal/mol for aryl dicyanomethyl radicals, but has not always reproduced the sigma-dimer-pimer equilibrium.[68] Single-point energy computations were compared on the lowest energy optimized σ and π dimers using both B97D24/6-31+G(d,p)[69] (dispersion included) and B9825/6-31+G(d,p)[70] (without dispersion forces) (**Table S1**).[71] This was done to determine the influence of dispersion energy on σ-dimer and π-dimer optimized geometries.

To screen radical monomers for future investigation, we used a radical stability score (RSS) based on thermodynamic stabilization via electron delocalization and kinetic persistence ascribed to steric hinderance as described by Paton.[62] The largest (Mulliken) spin density can be obtained from DFT calculations of the radical and then normalized by summing all the absolute contribution of all non-hydrogen atoms and dividing the largest spin density values by the total. The extent at which adjacent functional groups occupy the space around the radical-centers, based off the Mulliken spin values, was measured by the occupied volumetric percent of a predefined sphere. We used a sphere with a 3.5 Å radius, based on the findings of Paton. This concept of buried volume was originally developed by Cavallo and Nolan for coordinating NHC ligands[63] and was readily calculated using ChimeraX[182] with the SEQCROW plugin.[183] This works by breaking the sphere up into voxels of 0.05 Å and checking if each voxel is within an unscaled Bondi radii of any other atom. These two values were used as developed by Paton, to produce a quantitative radical stability score (RSS), RSS = V_{bur} + 50 × (1 – normalized max Mulliken spin) (**Figure 4.2**). For [3]radialenes there are often three near equivalent radical-centers and the carbon with the worst RSS score may not necessarily have the maximum spin density due to buried-volume contributions. To account for this the RSS for each carbon-center was calculated with the lowest RSS being assigned to that derivative. Since these are carbon-centered radicals, conventionally less stable than alternative heteroatoms, it was presumed that increasing buried volume would be critical to improving kinetic stability.

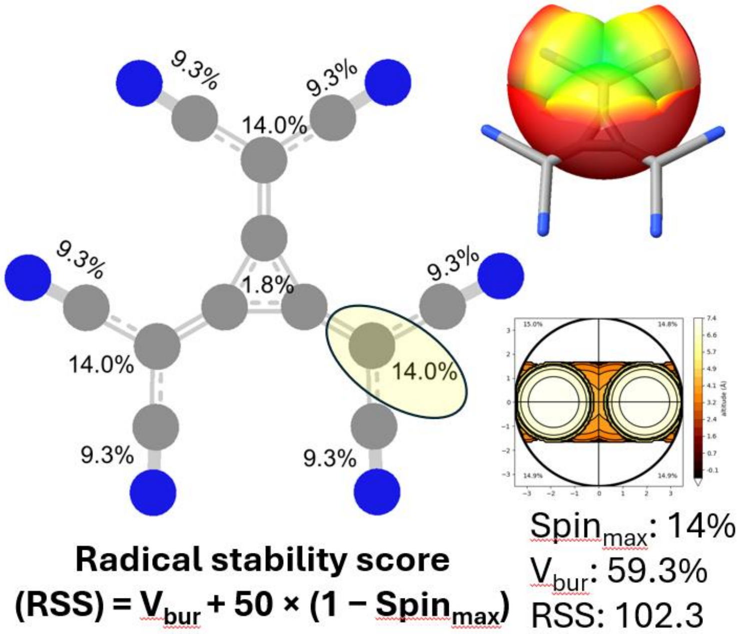

Figure 4.2 Radical stability score calculation on hexa-cyano [3]radialene using Paton's method. Showing a maximum normalized Mulliken spin density at three alpha carbons of 14.0%, a buried volume of 59.3% around atomic site of maximum spin density, and a resultant radical stability score of 102.3.

The most fundamental property of any electroactive material is the standard reduction potential, which is proportional to the Gibb's free energy of the redox half reaction, $\Delta G_{solv}^{\circ,redox}$. Using the Born-Haber cycle, this consists of the free energy change in the gas phase and the solvation free energies of the oxidized and reduced species, $\Delta G_{solv}^{\circ,redox} = \Delta G_{g}^{\circ,redox} + \Delta G_{solv}^{\circ}(Red) - \Delta G_{s}^{\circ}(Ox)$. Redox potentials are classically calculated using high-level *ab initio* calculations in the gas phase with the solvation energy being added at a lower-level of theory through single-point energy calculations for which the solvation models are typically parameterized. The standard Gibbs free energy can then be used with the Nernst equation, $\Delta G_{solv}^{\circ,redox} = -FE_{calc}^{\circ},$ to calculate the standard one-electron redox potential. Though direct calculations of reaction free energies within the SMD solvation model have been shown to produce reliable approximations of thermodynamic cycles and even improve approximation for molecules that undergo significant structural changes during solvation.[184] We took the latter approach after determining it produced results with suitable accuracy, detailed in section 4.3.2, when taking into consideration the flexibility of the aqueous solvent window.

4.3 Results and Discussion

4.3.1 [3]Radialene Dimerization Investigation

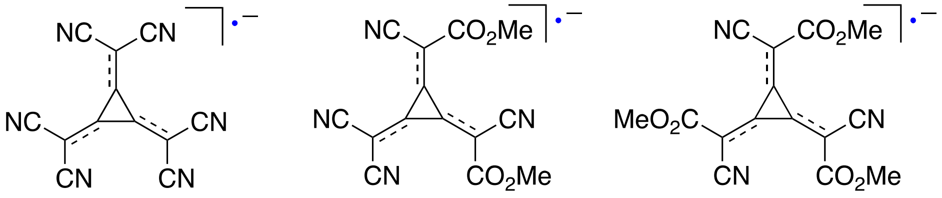

	1	**2**	**3**
MeCN	**free radical**	**free radical**	**free radical**
H_2O	**free radical**	**π-dimer**	**σ-dimer**
Aq. NaCl	**free radical**	**π-dimer**	**π-dimer**

Figure 4.3 Hexa-substituted [3]radialene radical anions and their dimerization behavior in different solvents. *Adapted from [178] with permission John Wiley and Sons.*

Low interaction energies (ΔE) in gas support that **1**–**3** (**Figure 4.3**) are radical anions in nonpolar media (**Table 2**), with **1** maintaining unfavorable dimer energies even in water. Conversely, **2** and **3** form dimers that are stabilized in water. Calculations reveal that **3** has the largest energy of interaction (E_{int}) as a σ-dimer by about 10 kcal mol^{-1} (**Table 2**). This is in agreement with the electrochemical and optical spectroscopic data.[178] The preference for dimerization in aqueous may arise from the enhanced solvation of the dimer due to its larger electrostatic field. Influence of this charge distribution could be investigated using methods such as the Voroni deformation density to quantify this charge separation.[185] Additionally, **2** and **3** form more hydrogen bonds than **1**, which can overcome the long-range Columbic repulsions that inhibit dimerization.

Table 2. DFT calculated interaction energies and max Mulliken spin densities of the σ- and π-dimers of **1-3.**

[3]radialene	$\Delta E_{\sigma,gas}$ kcal mol^{-1}	$\Delta E_{\pi,gas}$ kcal mol^{-1}	$\Delta\Delta E_{\sigma,water}$ kcal mol^{-1}	$\Delta\Delta E_{\pi,water}$ kcal mol^{-1}	$Spin_{max}$
Hexa-cyano (1)	54.6	59.8	6.7	7.4	14%
Di-ester (2)	39.5	52.7	-6.6	-0.1	16%
Tri-ester (3)	42.8	57.1	-10.1	-1.9	17%

ΔE values in kcal/mol; $\Delta E_{\sigma/\pi}$ (calcd)= $\Delta E_{\sigma/\pi} - 2E_{\text{radical-anion}}$ at the ω-B97XD/6-311+G(d,p), SMD level of theory. *Adapted from [178] with permission John Wiley and Sons.*

We used DFT calculations to investigate the differences in spin density, London dispersion forces, and polarizability to explain the observed dimer equilibria.[181] The highest aqueous normalized Mulliken spin density values of **1**–**3** increase with the number of ester units (**Table 2**). Higher spin localization tends to promote the formation of stable σ-dimers as is observed tri-ester **3** (**Figure S1**). In contrast, pimer dispersion force values across the series are near equivalent (**Table S1**). A correlation can be drawn between the dimer interaction energies and the isotropic polarizability which all increase with additional esters. Finally, observable difference in dimerization mode between **2** and **3** may be rationalized by the monomer planarity (**Figure 4.4**). Radical **3** deviates the most from planarity due to the steric constraints of three ester groups that hinders the π-accepting cyano-groups which better withdraw the SOMO electron through the π-system in more planar molecules.[186] This reduces the strain energy that weakens the C-C bond formed during σ-dimerization due to the pyramidalization of the dimerizing radicals.[187]

Generation of the new σ-bond also relieves strain in **3** (**Figure 4.4**), which gains planarity away from the site of dimerization. Radialene **2** is relatively planar compared to **3** and does not similarly benefit from σ-dimerization (**Figure 4.4**). These subtle structural features conceivably lead to the different dimer equilibria behaviors of **2** and **3**. This feature could be better quantified with the pyramidalization energy of these dimerizing radicals by comparing the gas-phase bonding energy of dimerization, dictated by the interaction energy. But it is well known that cyano groups prefer planar radicals which enhance withdrawing the electron of the SOMO through the π-system.[186, 188]

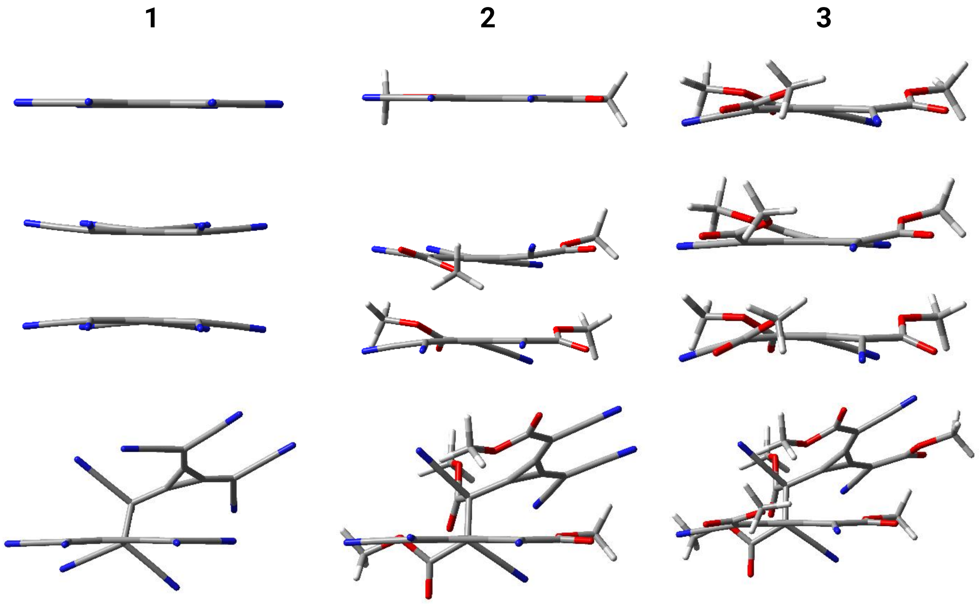

Figure 4.4 Gas optimized structures of hexa-cyano (1), di-ester (2), and tri-ester (3). Free radical (top), π-dimer (middle), and sigma-dimer (bottom). *Adapted from [178] with permission John Wiley and Sons.*

4.3.2 Screening of [3]Radialene Derivatives

Derivatives with high solubility are a prerequisite for an efficient RFB. However, solubility can largely be altered by factors that have little influence on the core electronic structure of the molecule. Such factors include distant functionalization, dimerization, or counterion substitution. It is also difficult to ascertain any meaningful measurement of solubility without considering the dissociation energy from the solid. Properties such dipole moment are still taken into consideration when selecting molecules for aqueous RFB synthesis, but we largely ignored solubility as a screening parameter for our early investigation. Redox potential is likely the most accurate value to screen by in the development of RFB electrolytes. Since [3]radialenes have two potentially stable redox pairs either or both could be used as a catholyte assuming they are between 0.5V – 1.0V vs. SHE. In a neutral pH an ideal oxidation is going to be around 0.817 V vs SHE, but with the sluggish kinetics of oxygen evolution especially in more acidic environments there is flexibility to tune the RFB for the specific molecule.[74] The [3]radialene hexa-cyano derivative's oxidation couples are about typically about 0.9-1.0 V apart and highly influenced by the withdrawing strength of the substituents. If they can be brought further apart (~1.2V) and properly centered within the water window, they could be considered for a symmetric flow cell, removing crossover capacity fade. If they can be brought closer together, they may be considered as a two electron catholyte. The first oxidation potentials to our earliest synthesized [3]radialene derivatives can be seen in (**Table 3**), demonstrating an acceptable level of accuracy with the experimental values deviating less than 70 mV from those measured. We attempted to apply these screening principles to over a hundred [3]radialene derivatives by taking the calculated oxidation potentials and RSS scores into consideration.

Table 3. DFT calculated $E^{1/2}$ experimental redox potentials vs those measured aqueously by CV vs a saturated Ag/AgCl reference.

[3]Radialene Derivatives	**Exp (satAg/AgCl) $Ox^{-2/-1}$ (mV)**	**Calc(satAg/AgCl) $Ox^{-2/-1}$ (mV)**
Hexa-cyano	510	470
Mono-ester	430	397
Di-ester	380	386
Tri-ester	300	369
Mono-methylsulfone	510	450
Di-methylsulfone	550	500

DFT calculated $E^{1/2}$ using ω-B97XD/6-311+G(d,p), SMD_{water} level of theory optimized for all [3]radialene oxidation states with frequency calculations to ensure minimum. Differences between oxidized and reduced energies were referenced to SHE using a 4.28 V reference correction followed by 0.197 V to convert to Ag/AgCl.

These computations led our group to synthetically prepare and crystalize a series of methylsulfone asymmetric [3]radialenes including the mono, di, and tri along with mono versions of an amide and 4-benzonitrile. As seen in **Figure 4.5**, each derivative was predicted to have improved stability, based on RSS, over the hexa-cyano. Enhanced solubility is due to increased buried volume contributions at the sites of increased spin density and conversely lower spin density at the unmodified alpha carbons. This was a common trend in polar solvent calculations predicting that spin density would be localized toward the less withdrawing substituents. These derivatives were synthesized and isolated through crystallization as confirmed by SCXRD. All were found to be reversible in CV studies except that of the tri methylsulfone, mono amide, and mono 4-benzonitrile. Higher RSS scores should correlate with increased radical stability, but this did not match the CV findings. It was noticed that decreasing the weighting of the buried volumes contributions in RSS score improved the predictive results. So much so that looking at the inverse of maximum spin density alone was actually an accurate predictor of stability in the synthesized systems (**Figure 4.5**).

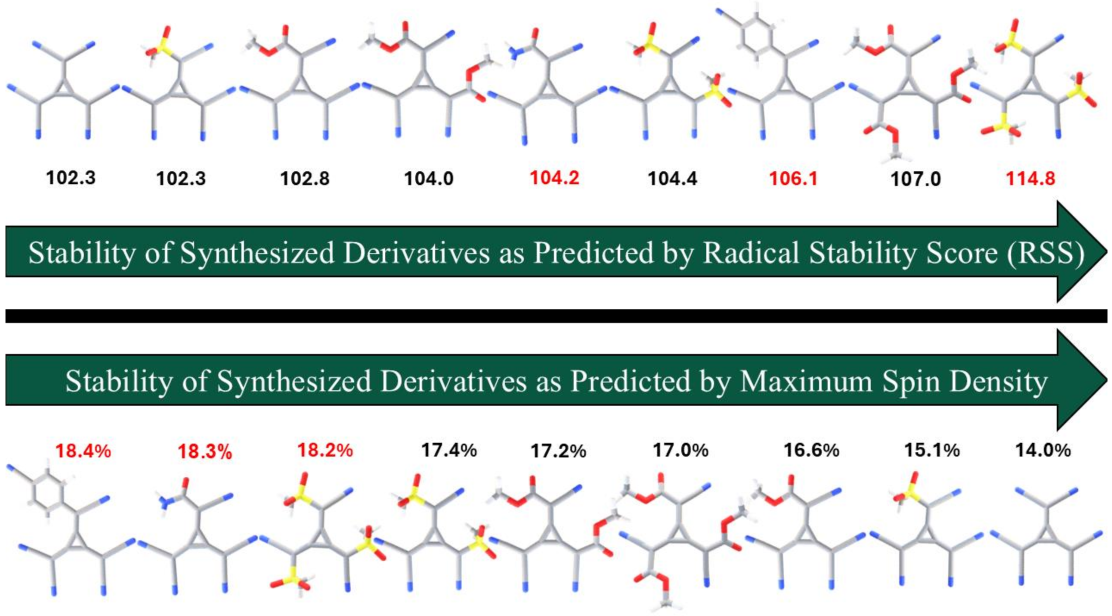

Figure 4.5 Stability analysis of [3]radialene hexa-cyano derivatives (methyl ester series, methyl sulfone series, mono 4-benzonitrile, and mono amide). Green arrows show predicted increase in stability based off the derivatives ordered by radical stability score (top) or isolated maximum spin density metric (bottom). Red numbers indicate irreversible CV measurements. (note: tri methyl sulfone showed partial reversibility)

Based on this simple observation we have continued computationally investigating [3]radialene monomers with a specific focus on lowering spin density. To date, only one derivate has been predicted with a lower maximum spin density than hexa-cyano while having an oxidation potential sufficient for an aqueous RFB catholyte. This is the tri-pyridinium, with the lowest energy optimized structure shown in **Figure 4.6**. It has a predicted spin density maximum of 13.1%, well below the 14.0% of the hexa-cyano, and an RSS score of 110.3. The first two oxidation states are predicted to be 0.69 and 1.03 V vs SHE. This redox pair gap of only 0.34V is the lowest predicted of any [3]radialene derivate and provides the possibility of two electron transfers both within the workable aqueous catholyte window. This molecule is currently being synthesized and our computational investigation is ongoing.

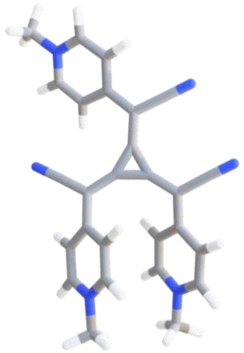

Figure 4.6 Optimized structure of tri-pyridinium^{-1} in the lowest energy confirmation. Neighboring pyridiniums as shown are also the lowest energy confirmation for the dianion.

It is not entirely surprising that the mild and asymmetric steric protection afforded by these substituents is insufficient to prevent attack of these trigonal carbon-based radicals. It would be worth synthetic effort to investigate whether much more extreme steric protection is beneficial. If the influence of sterics on the reaction kinetics is inconsequential we could focus on more direct thermodynamic calculations of stability. Radical stabilization energy, calculated through isodesmic H-atom transfer reactions, could provide a more reliable thermodynamic analysis by comparing bond dissociation energies between the carbon-centered radical and methane.[189] Unfortunately this calculation may have to be performed for all three potential radical centers if they are asymmetric.

4.4 Conclusions

We have used DFT calculations to begin to ascertain the driving forces behind dimerization in [3]radialene radicals. Spin density and solvent stabilization of the dimers were found to both play significant roles. Solvent significantly stabilizes both σ and π-dimers of these anionic [3]radialene radicals. Furthermore, we need to quantitatively consider the strain energy necessary for pyramidalization. The interaction energies we have calculated can be broken down into electrostatic, Pauli repulsion, and orbital interactions. Using molecular orbital theory to quantify these contributions would increase our understanding of the dimer equilibria. We are looking into charge distribution descriptors using the Voronoi deformation density, due to the significant stabilizing impact of polar solvents on these anionic dimers.[190] This may help explain the flow of charge as a result of dimer interactions.

The DFT methods within have been adequate predictors of redox potential for all synthesized [3]radialenes. It has been identified that RSS scores alone are inadequate for predicting the stability of [3]radialene radicals. We ascribe this to an overestimation of thermodynamic stability for the unusually high radical delocalization. The current overlap of the synthetic and computation data sets has directed us toward the exploration of hexa-cyano [3]radialene derivatives with particularly low normalized spin densities with redox couples in the necessary aqueous potential window. For which, the tri-pyridinium derivative shows promise. Kinetic stabilization could still play an important role, as such derivatives with exceptionally high buried volume are still under investigation. Spin density alone has been a promising descriptor of the stability of synthesized [3]radialene radicals with buried volumes below 75%, but as our synthetic database expands it would worth comparing thermodynamic calculations of stability. Radical stabilization energy, calculated through isodesmic H-atom transfer reactions, may provide a more reliable thermodynamic analysis by comparing bond dissociation energies between the carbon-centered radical and methane. [189] This calculation is not as efficient since asymmetric [3]radialenes need up to three separate calculations to be fully described, where the current spin density analysis gives a metric for each site with a single calculation.

The computational prediction of dimerization was used in conjunction with the computational database to predict a [3]radialene derivative that would form a particularly strong σ dimer. These are of particular interest in the field of polymers as controllable and reversible bonds. By computationally replacing both cyanos at a single site with dimethyl malonate we achieve a simultaneous reduction in strain energy for σ dimerization along with an increase in maximum spin density of 19.8%. Upon synthetic formation and oxidation of this predicted dianion to a radical the normal blue color was unobservable due to the rapid formation of sigma dimer. This radical could be freeze dried upon which mechanical grinding in a mortar reveals a brilliant blue for the presumable breaking of σ-dimer (**Figure 4.7**). We were recently able to crystalize this structure as a di-tetrabutylammonium salt showing the first SCXRD structure of a [3]radialene sigma dimer.

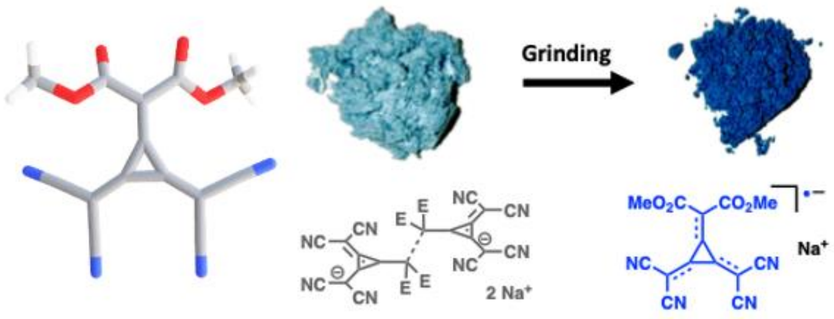

Figure 4.7 Synthesis of a predicted hexa-cyano [3]radialene di-ester derivative using dimethyl malonate showing a σ-dimer that can be broken with mechanical force.

4.5 Appendix C: Chapter 4 Supplementary Information

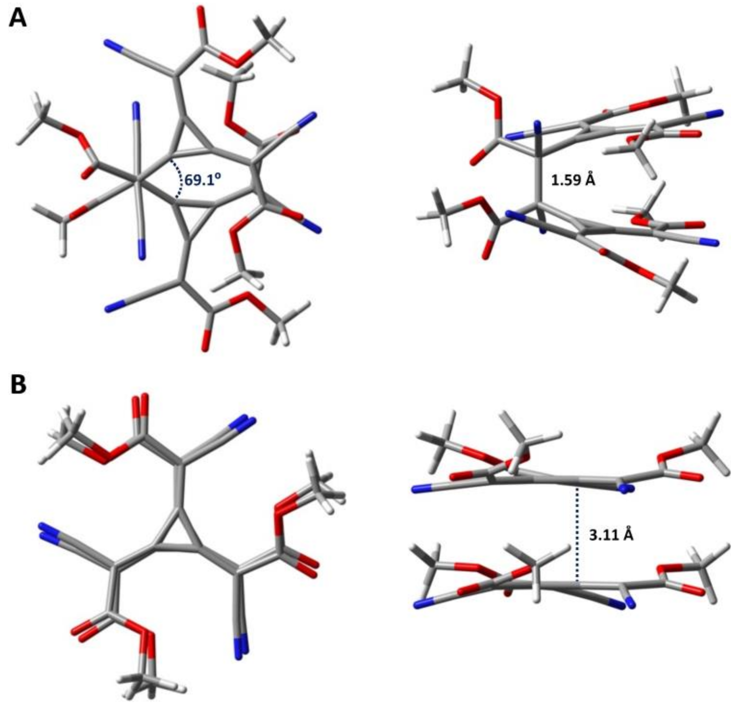

Figure S1 DFT-calculated global-minimum structures of the a) σ- and b) π-dimers of tri-ester [3]radialene$^-$ with select dihedral angles and bond lengths (ω-B97XD/6-311+G(d,p)). *Adapted from [178] with permission John Wiley and Sons.*

Table S1. Calculated dispersion forces of π-dimer & σ-dimer of 1-3 in SMD water.

Water	**UB97D Pimer** (Hartree)	**UB97D Sigma** (Hartree)	**UB98 Pimer** (Hartree)	**UB98 Sigma** (Hartree)	**Pimer Dispersion (kcal)**
1	-1570.809219	-1570.809219	-1570.809219	-1570.809219	**12.2**
2	-2113.260175	-2113.260175	-2113.260175	-2113.260175	**12.1**
3	-2384.468721	-2384.468721	-2384.468721	-2384.468721	**14.1**

Absolute dispersion forces are calculated by taking optimized structures (wb97XD,SMD$_{water}$) and running single point energy calculations using dispersion corrected functional (UB97D) and uncorrected functional (UB98). The difference between the functionals provides an absolute dispersion parameter. *Adapted from [178] with permission John Wiley and Sons.*

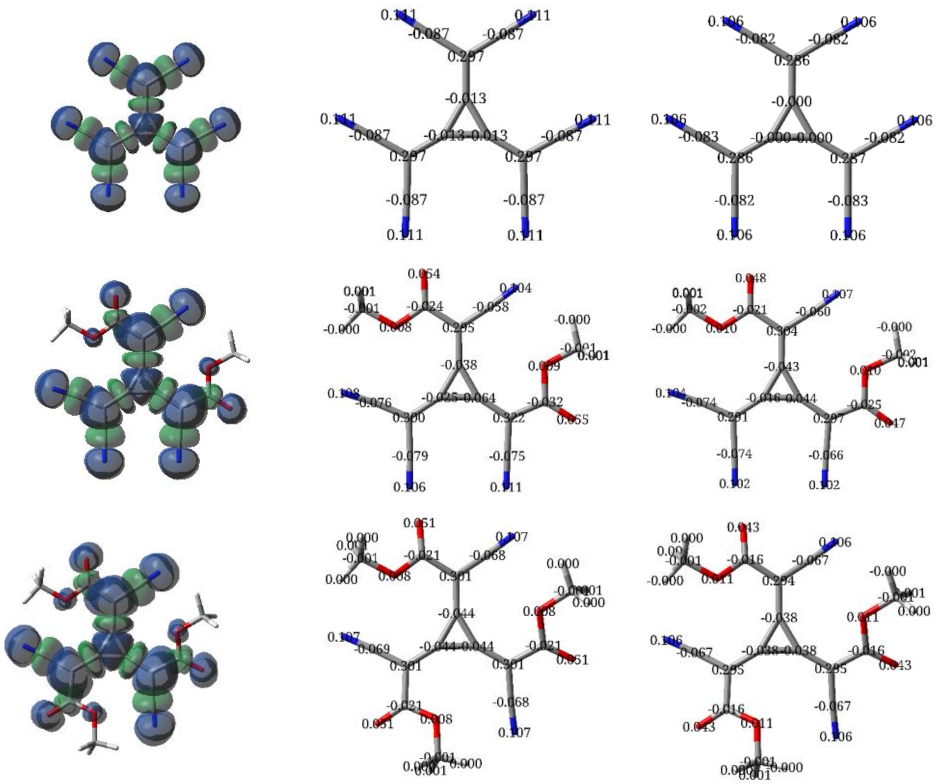

Figure S2 Spin density of 1-3. Calculated molecular orbitals with alpha (blue) and beta (green) depicted at isovalue 0.0004. Unnormalized Mulliken spin densities calculated in gas (center) and water (right). *Adapted from [178] with permission John Wiley and Sons.*

XYZ coordinates of calculated global minima for radicals and dimers. *Adapted from [178] with permission John Wiley and Sons.*

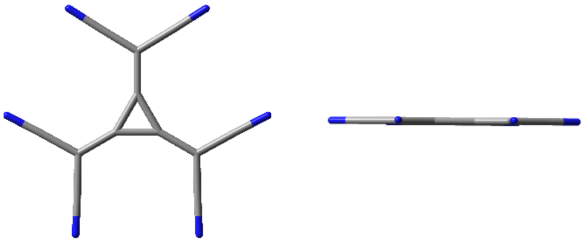

Hexa-cyano_Radical Anion (1)

EE + G_{corr} (UwB97XD) = -785.546623 Ha

N	1.9697	-0.0002	4.4737
C	-0.7007	0.0002	-1.2125
C	0	0	0
N	2.1883	0.0002	2.7306
C	0.6997	0.0002	-1.213
C	0	0	1.3734
N	-2.1879	0.0001	2.7309
C	1.919	0.0003	-3.3205
C	1.889	0.0001	-1.9001
C	3.1343	-0.0003	-1.2164
C	1.2149	0	2.1099
C	-1.2149	0	2.1098
C	-1.9211	0.0007	-3.3192
C	-1.8903	0.0004	-1.8988
N	-4.1598	0.0001	-0.6824
C	-3.1354	0.0002	-1.2146
N	4.1589	-0.0006	-0.6844
N	-1.9732	0.001	-4.4724

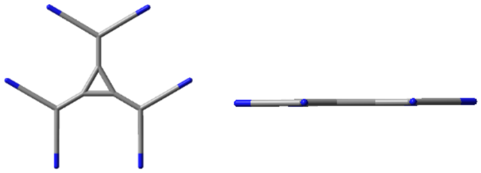

Hexa-cyano_Radical Anion (1) SMD(water)

EE + G_{corr} (UwB97XD) = -785.598594 Ha

N	-1.5125	1.625	2.6702
C	-0.4752	0.5097	-1.2082
C	0.4762	-0.5106	-1.2075
N	2.806	-3.013	-0.613
C	0	0	0
C	1.2866	-1.3799	-1.893
N	1.2959	-1.3901	-4.4645
C	-0.8317	0.892	2.0906
C	0	0	1.3721
C	0.8321	-0.8923	2.0895
C	2.1257	-2.2799	-1.1928
C	1.2951	-1.3891	-3.3084
C	-2.1243	2.2784	-1.1941
C	-1.2854	1.3788	-1.8942
N	-1.2939	1.3884	-4.4659
C	-1.2942	1.3884	-3.3098
N	1.516	-1.6255	2.6652
N	-2.8074	3.011	-0.6169

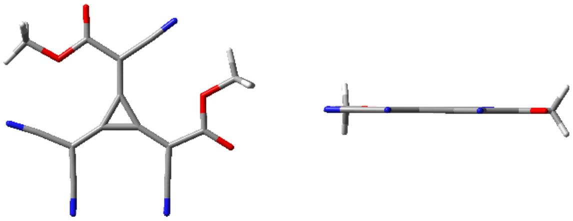

Diester Radical Anion (2)

EE + G_{corr} (UwB97XD) = -1056.753859 Ha

O	-1.1775	0.4459	3.3883
O	3.9291	-1.4882	-2.0714
O	2.9592	-1.1201	-0.0803
O	-2.1855	0.8277	1.4211
N	1.9929	-0.7551	2.8183

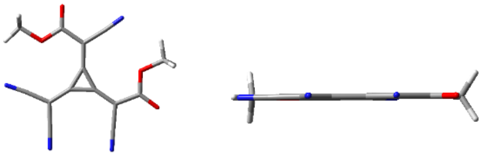

Diester Radical Anion (2) SMD(water)

EE + G_{corr} (UwB97XD) = -1056.817773 Ha

O	-1.1185	0.4604	3.4053
O	3.8672	-1.5992	-2.156
O	2.9826	-1.231	-0.1251
O	-2.162	0.879	1.4637
N	1.9744	-0.8107	2.8056

C	0.6368	-0.2413	-1.2307	C	0.6326	-0.2632	-1.2242
C	-0.6737	0.2552	-1.2045	C	-0.6588	0.2722	-1.2041
N	-4.009	1.5183	-1.0145	N	-3.9405	1.6536	-1.0378
C	0	0	0	C	0	0	0
C	-1.7632	0.6679	-1.9376	C	-1.727	0.7166	-1.9467
N	-1.7654	0.6688	-4.5145	N	-1.6548	0.6749	-4.5194
C	1.1214	-0.4249	2.1369	C	1.1107	-0.4561	2.1236
C	0	0	1.3759	C	0	0	1.3735
C	-1.1526	0.4367	2.1794	C	-1.1322	0.463	2.1869
C	-2.9821	1.1297	-1.3734	C	-2.9283	1.225	-1.3958
C	-1.7333	0.6566	-3.3605	C	-1.671	0.6868	-3.3632
C	2.978	-1.1282	-1.4177	C	2.9498	-1.2198	-1.4491
C	1.71	-0.6479	-1.9867	C	1.6881	-0.7002	-1.9855
N	1.5922	-0.6037	-4.5586	N	1.5399	-0.6419	-4.5532
C	4.1475	-1.5695	0.566	C	4.1863	-1.7256	0.4838
H	4.994	-0.9398	0.2841	H	5.0363	-1.1085	0.1909
H	4.3647	-2.6021	0.2851	H	4.3548	-2.7633	0.1944
H	3.9387	-1.4899	1.6299	H	4.0155	-1.6531	1.5544
C	-3.3427	1.2658	2.1306	C	-3.3064	1.3454	2.1984
H	-4.0627	1.5384	1.3633	H	-4.0324	1.6367	1.4445
H	-3.0988	2.1235	2.7606	H	-3.0322	2.202	2.8147
H	-3.728	0.4616	2.7606	H	-3.704	0.5432	2.8208
C	1.635	-0.6197	-3.4052	C	1.5949	-0.6634	-3.3981

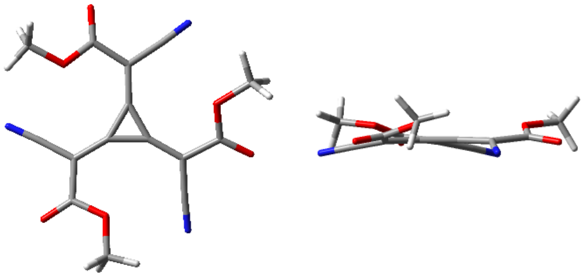

Triester Radical Anion (3)

EE + G_{corr} (UwB97XD) = -1192.357696 Ha

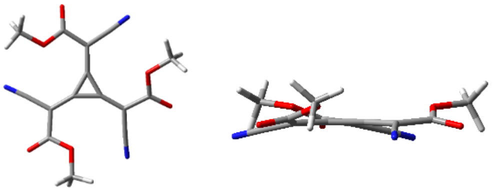

Triester Radical Anion (3) SMD(water)

EE + G_{corr} (UwB97XD) = -1192.421654 Ha

O	-2.3999	3.5102	-1.7907	O	2.4415	-3.4742	-1.8008
O	0.7233	-1.0708	3.3726	O	-0.6764	1.073	3.3762
O	0.8011	-0.4767	-3.8955	O	-0.8049	0.5208	-3.9028
O	1.7028	-1.5908	1.4215	O	-1.7219	1.5624	1.45
O	1.4724	-2.6154	-4.0064	O	-1.3603	2.6952	-3.98
O	-1.2122	2.8566	-0.002	O	1.1778	-2.8997	-0.0357
N	1.8619	-3.7836	-0.7582	N	-1.7356	3.8253	-0.7402
N	-1.4688	1.5627	2.7992	N	1.5049	-1.5354	2.7831
N	-1.6015	1.3999	-4.4323	N	1.6976	-1.3267	-4.3992
C	-0.3995	0.5564	-1.2263	C	0.407	-0.5529	-1.2207
C	0.3617	-0.6239	-1.2054	C	-0.343	0.6299	-1.2032
C	0	0	0	C	0	0	0
C	0	0	1.3768	C	0	0	1.3742

C	1.46	-2.8112	-1.2347	C	-1.373	2.8379	-1.2215
C	0.8144	-0.9301	2.1748	C	-0.8097	0.9274	2.1734
C	-0.812	0.8856	2.1326	C	0.8272	-0.8737	2.1189
C	-1.0935	1.5272	-1.9128	C	1.1107	-1.5154	-1.9039
C	0.9588	-1.6571	-1.8919	C	-0.9117	1.6775	-1.887
C	-1.345	1.434	-3.3067	C	1.3987	-1.3885	-3.2833
C	1.1016	-1.6652	-3.3565	C	-1.0406	1.7025	-3.3491
C	-1.653	2.7211	-1.2593	C	1.6576	-2.7148	-1.2583
C	0.8729	-0.4016	-5.3166	C	-0.8982	0.4481	-5.334
H	1.8988	-0.5687	-5.6525	H	-1.8923	0.7539	-5.6611
H	0.5274	0.5968	-5.5707	H	-0.7215	-0.5947	-5.5823
H	0.2201	-1.1484	-5.7715	H	-0.1377	1.0807	-5.7933
C	2.5104	-2.5456	2.1044	C	-2.557	2.5027	2.1437
H	3.1406	-2.0472	2.8444	H	-3.0889	2.0046	2.9549
H	3.1053	-3.0256	1.332	H	-3.258	2.8698	1.3994
H	1.8845	-3.2855	2.6057	H	-1.9548	3.3237	2.5344
C	-1.7336	3.966	0.7244	C	1.6638	-4.0442	0.6829
H	-1.4248	4.9033	0.256	H	1.4513	-4.9562	0.1243
H	-1.3293	3.8693	1.7284	H	1.1244	-4.043	1.6259
H	-2.8235	3.9226	0.7564	H	2.7359	-3.9501	0.8598

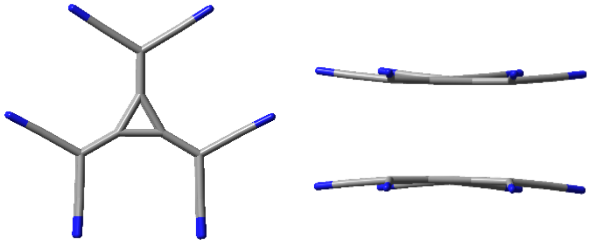

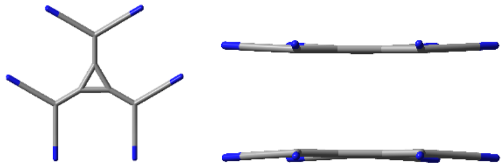

1 Pimer

EE + G_{corr} (UwB97XD) = -1570.998421 Ha

1 Pimer SMD(water)

EE + G_{corr} (UwB97XD) = -1571.184671 Ha

N	-1.8725	-3.7072	0.8757	N	3.896	-1.5144	1.5808
C	0.7161	-0.3941	0.542	C	0.4063	0.7463	-1.5647
C	-0.0159	0.8024	0.5395	C	-0.7292	-0.0653	-1.6079
N	-2.2568	3.4773	0.808	N	-3.1493	-2.535	-1.8393
C	-0.6858	-0.4296	0.5647	C	0.5413	-0.6437	-1.5682
C	-0.0506	2.1727	0.5492	C	-2.0918	-0.198	-1.6508
N	2.0938	3.5889	0.7299	N	-3.5808	1.892	-1.8225
C	-1.846	-2.5615	0.7398	C	2.7465	-1.6312	-1.5555
C	-1.8545	-1.1444	0.6135	C	1.3358	-1.7588	-1.5389
C	-3.1124	-0.4917	0.7382	C	0.7585	-3.0495	-1.6289
C	-1.2802	2.8773	0.6738	C	-2.6808	-1.4825	-1.748
C	1.145	2.9393	0.6313	C	-2.918	0.9491	-1.7387
C	1.9878	-2.4643	0.681	C	2.3806	2.1397	-1.5463
C	1.9204	-1.0489	0.5536	C	0.9717	1.9933	-1.5282
N	4.1566	0.2167	0.7389	N	-0.5182	4.0839	-1.6879
C	3.1469	-0.333	0.6377	C	0.1564	3.1488	-1.6095

N	-4.1449	0.0059	0.8733
N	2.0771	-3.6068	0.8173
N	-2.2911	3.4498	-2.8434
N	2.0595	3.5373	-2.9201
C	-1.3137	2.847	-2.7283
C	1.1118	2.8959	-2.7708
C	-0.0841	2.1384	-2.6285
C	-0.0558	0.7685	-2.5882
N	-4.1967	-0.0129	-2.7701
N	4.1056	0.1556	-2.9084
C	-3.1629	-0.5134	-2.6582
C	-0.7319	-0.4601	-2.5637
C	0.6702	-0.4316	-2.5872
C	3.0971	-0.3858	-2.7616
C	-1.9047	-1.17	-2.56
C	1.8705	-1.0928	-2.6215
C	-1.9068	-2.5893	-2.6574
C	1.9273	-2.5111	-2.7176
N	-1.9433	-3.7373	-2.7689
N	2.0069	-3.657	-2.8295

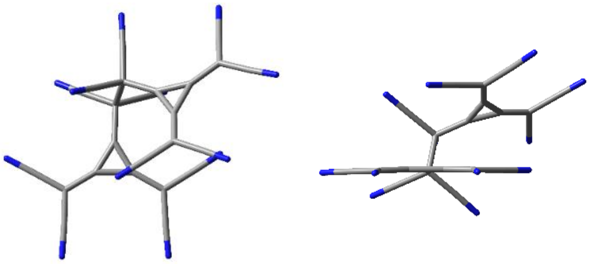

1 sigma dimer-a

EE + G_{corr} (RwB97XD) = -1571.006475 Ha

N	2.3522	-3.936	1.9988
N	4.9603	2.0731	-1.2319
N	-0.7862	2.0748	2.6453
C	1.3986	0.5929	0.4601
C	1.5241	-0.6944	0.9159
C	2.6131	-0.0166	0.2705
C	3.9193	-0.0142	-0.1377
C	1.7629	-2.968	1.7782
C	4.7661	-1.1406	0.0432
C	4.4819	1.1406	-0.7453
C	0.5563	1.8157	0.4071
C	1.0063	-1.7869	1.5548
C	-0.2119	1.951	1.659
C	-0.3341	-1.7355	2.0254
C	1.3933	3.0201	0.2555
N	0.8461	1.5919	-3.0696

N	0.2785	-4.0973	-1.7132
N	3.531	2.2467	-1.5731
C	2.6009	-1.652	1.7234
C	2.2307	2.1166	1.7323
C	0.0051	3.1224	1.6628
C	0.8266	1.9694	1.6167
C	0.262	0.7216	1.5938
C	0.3982	-0.6683	1.5911
C	1.195	-1.7822	1.6079
C	-0.8725	-0.0912	1.549
C	0.6141	-3.0736	1.6483
C	-2.2343	-0.2243	1.4917
C	-3.066	0.9215	1.534
C	-2.8291	-1.5096	1.5285
N	-3.3048	-2.5619	1.5695
N	3.3766	2.2241	1.8376
N	-0.676	4.0546	1.7133
N	-3.7354	1.8623	1.5804
N	0.1283	-4.1212	1.6933
N	3.7455	-1.5323	1.8289

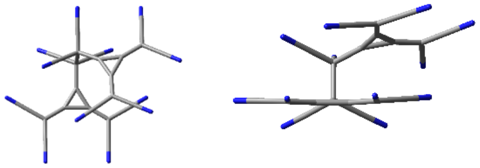

1 sigma dimer-a SMD(water)

EE + G_{corr} (RwB97XD) = -1571.186585 Ha

N	2.0776	-3.98	1.4219
N	4.6723	2.0356	-1.3452
N	-1.3346	2.0699	2.4161
C	1.2595	0.702	0.6538
C	1.3282	-0.6126	1.0122
C	2.4107	0.0358	0.3494
C	3.66	-0.0382	-0.212
C	1.4962	-2.9804	1.4716
C	4.3786	-1.2549	-0.2007
C	4.2203	1.0985	-0.8381
C	0.4338	1.9253	0.4899
C	0.7826	-1.762	1.5258
C	-0.5546	2.0204	1.5752
C	-0.5485	-1.7555	2.0032
C	1.2993	3.1143	0.4921
N	1.3922	1.5931	-2.843

N	-4.877	2.4749	0.7363	N	-4.5982	2.4448	0.8411
C	0.2705	1.6498	-2.078	C	0.614	1.715	-2.0078
C	-4.4484	1.4555	0.401	C	-4.1939	1.4174	0.4941
C	-0.4985	1.7472	-0.8231	C	-0.3744	1.8394	-0.9253
C	-1.274	3.0007	-0.8615	C	-1.1734	3.0606	-1.1067
C	-1.401	0.5744	-0.6909	C	-1.2642	0.6499	-0.9084
C	-3.9471	0.194	-0.0191	C	-3.6909	0.1696	0.0602
C	-2.644	0.0629	-0.4158	C	-2.4439	0.0948	-0.5057
C	-1.5924	-0.7596	-0.9447	C	-1.3976	-0.6997	-1.0589
N	-2.5828	-4.0841	-1.5232	N	-2.3019	-4.0511	-0.9429
C	-1.9457	-3.1239	-1.4503	C	-1.6743	-3.0997	-1.1445
C	-1.1312	-1.9612	-1.4066	C	-0.9061	-1.9386	-1.3846
C	0.2088	-2.0478	-1.8731	C	0.4228	-2.0688	-1.8503
C	-4.8507	-0.9025	-0.029	C	-4.4635	-0.9987	0.246
N	-5.6298	-1.755	-0.0405	N	-5.0951	-1.9564	0.3992
N	1.3012	-2.0918	-2.2463	N	1.515	-2.1617	-2.2212
N	-1.4255	-1.6687	2.3982	N	-1.6423	-1.7352	2.3804
N	2.0164	3.9776	0.1416	N	1.9874	4.0332	0.4627
N	5.5013	-2.0195	0.1879	N	4.9662	-2.252	-0.1915
N	-1.8483	3.994	-0.8982	N	-1.8092	4.0108	-1.2142

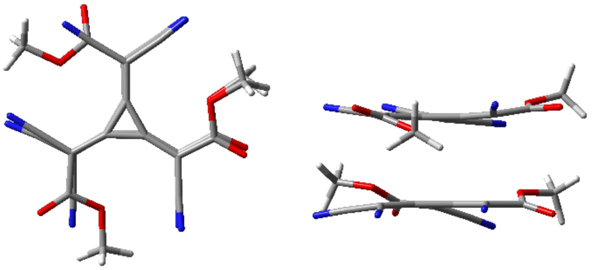

2 pimer

EE + G_{corr} (UwB97XD) = -2113.424098 Ha

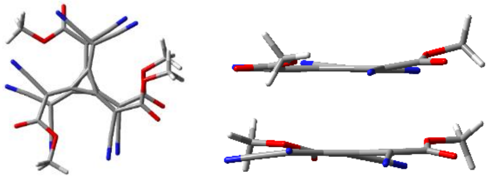

2 pimer SMD(water)

EE + G_{corr} (UwB97XD) =-2113.635662 Ha

O	-1.8947	-3.5961	-0.9465	O	-1.492	-3.7891	-0.6286
O	4.2062	0.8317	-0.9412	O	4.2941	1.2863	-0.6645
O	2.8697	-0.8068	-0.1702	O	3.1257	-0.6205	-0.8659
O	-2.6675	-1.4921	-0.9707	O	-2.4262	-1.7593	-0.8442
N	1.5447	-3.4481	-1.1393	N	1.9031	-3.4309	-0.3845
C	0.6405	0.6964	-0.5091	C	0.7309	0.6888	-0.5046
C	-0.7537	0.8431	-0.4388	C	-0.6689	0.7598	-0.4463
N	-4.2935	0.9708	-0.0831	N	-4.2167	0.768	-0.1946
C	-0.1945	-0.4375	-0.5334	C	-0.0348	-0.4896	-0.469
C	-1.8332	1.6895	-0.3212	C	-1.7781	1.5654	-0.3696
N	-1.6196	4.234	-0.665	N	-1.5799	4.1235	-0.5982
C	0.7201	-2.6804	-0.8884	C	1.0192	-2.6889	-0.4151
C	-0.3681	-1.7937	-0.6606	C	-0.1295	-1.8577	-0.4474
C	-1.6928	-2.4078	-0.8525	C	-1.4018	-2.5801	-0.6337
C	-3.1762	1.2438	-0.1914	C	-3.1074	1.0765	-0.2765
C	-1.6805	3.0944	-0.4885	C	-1.6489	2.9762	-0.4888

C	3.1169	0.4349	-0.5955	C	3.2379	0.6896	-0.689
C	1.8925	1.2544	-0.568	C	1.9295	1.3489	-0.5431
N	2.1717	3.8035	-0.788	N	2.015	3.9194	-0.6161
C	3.9675	-1.7228	-0.1698	C	4.3507	-1.3496	-1.0232
H	4.8164	-1.2863	0.3546	H	4.9785	-1.2202	-0.1421
H	4.2384	-1.9737	-1.1977	H	4.8773	-1.0071	-1.9146
H	3.6027	-2.6043	0.3504	H	4.0502	-2.3883	-1.1254
C	-3.9653	-2.0007	-1.2521	C	-3.6879	-2.3738	-1.1358
H	-4.6339	-1.1479	-1.1615	H	-4.4208	-1.5755	-1.0618
H	-4.2385	-2.7822	-0.542	H	-3.9042	-3.1664	-0.4205
H	-3.9936	-2.4187	-2.2622	H	-3.6693	-2.7897	-2.1444
C	2.043	2.6603	-0.6837	C	1.9565	2.7674	-0.5704
H	-0.5276	5.3655	1.4485	H	-0.1376	5.4005	1.4669
H	0.4522	5.3087	2.9503	H	0.37	5.3842	3.1822
H	1.1972	4.8932	1.3741	H	1.5186	4.883	1.9003
C	0.2877	4.8625	1.9674	C	0.4792	4.8983	2.2118
N	2.9887	3.5819	3.0275	N	3.2402	3.1808	2.7499
O	-1.9649	3.9933	3.1111	O	-1.9706	4.1526	2.9118
O	-0.0183	3.4723	2.1112	O	0.0962	3.5191	2.3061
C	-1.1771	3.1732	2.7006	C	-1.1586	3.2849	2.6707
C	2.6461	2.5013	2.8094	C	2.7261	2.1535	2.6371
C	-1.3799	1.7111	2.7623	C	-1.4637	1.8438	2.7312
C	2.335	1.1267	2.606	C	2.1988	0.8405	2.5227
C	1.0551	0.6405	2.572	C	0.8627	0.5334	2.5978
C	-2.6694	1.2674	3.1564	C	-2.8148	1.531	3.0305
C	-0.333	0.835	2.6253	C	-0.4949	0.8781	2.6652
C	3.4514	0.2463	2.6944	C	3.1565	-0.2076	2.4581
N	-3.7149	0.9431	3.5244	N	-3.9219	1.3561	3.3071
N	4.3901	-0.4154	2.8088	N	3.9508	-1.0432	2.3959
C	0.1928	-0.4682	2.5554	C	-0.111	-0.472	2.6473
C	0.0155	-1.8247	2.5105	C	-0.4174	-1.8074	2.6558
O	-2.2558	-1.5295	2.1771	O	-2.6695	-1.3575	2.3432
H	-4.18	-1.1695	1.7308	H	-4.5717	-0.871	1.9044
C	1.1367	-2.6946	2.5442	C	0.6062	-2.7719	2.8361
C	-1.3279	-2.4272	2.5356	C	-1.8004	-2.3125	2.6534
C	-3.6123	-1.9593	2.2176	C	-4.0567	-1.7149	2.3532
N	2.0513	-3.3984	2.5771	N	1.4239	-3.5684	3.0093
H	-3.7178	-2.9137	1.6979	H	-4.2185	-2.6222	1.773
H	-3.9405	-2.0675	3.2535	H	-4.3929	-1.8695	3.3795
O	-1.5752	-3.571	2.8354	O	-2.1013	-3.4637	2.8865

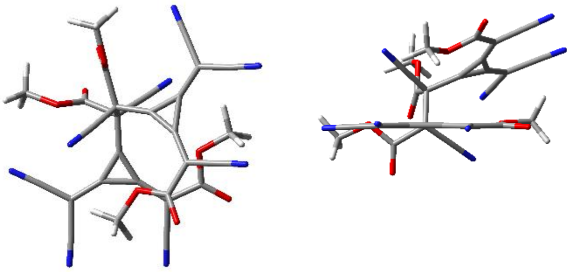

2 sigma dimer

EE + G_{corr} (RwB97XD) = -2113.444999 Ha

O	1.2384	3.7993	-0.4045
O	-0.7454	-1.331	1.8171
O	-0.1494	-3.3784	2.5301
O	1.956	3.1003	1.5997
N	3.3643	-3.6869	1.8092
N	4.666	2.8264	-0.645
N	-1.1069	1.7337	2.5843
C	1.4169	0.544	0.5993
C	1.7479	-0.7284	0.9992
C	2.7187	0.1677	0.4516
C	4.0237	0.447	0.0968
C	2.5176	-2.9102	1.6883
C	5.067	-0.5105	0.1775
C	4.3714	1.7522	-0.3289
C	0.4418	1.6686	0.4732
C	1.477	-1.9545	1.5441
C	-0.454	1.6798	1.6411
C	0.1436	-2.3253	2.0126
C	1.2548	2.997	0.4844
C	-2.0879	-1.6036	2.2098
H	-2.5367	-2.3445	1.544
H	-2.6141	-0.654	2.1328
H	-2.1203	-1.9744	3.2356
C	2.7797	4.2679	1.7134
H	3.5171	4.2766	0.9099
H	3.2646	4.179	2.6828
H	2.1592	5.1652	1.672
N	1.3186	1.2096	-2.8431
N	-4.7382	2.9181	0.3949
C	0.5654	1.3462	-1.988
H	-3.1358	4.5654	-0.934
O	-1.3536	3.2748	-2.3325
C	-4.3863	1.8471	0.1325
C	-0.3828	1.5787	-0.8876
C	-1.1459	2.8942	-1.218
C	-1.4186	0.5025	-0.8319

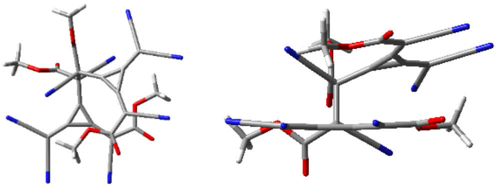

2 sigma dimer SMD(water)

EE + G_{corr} (RwB97XD) = -2113.645995 Ha

O	1.3783	-3.8181	0.3658
O	-0.9456	-1.2432	2.0094
O	-0.52	-3.4467	2.1254
O	1.8209	3.1979	1.7478
N	2.8803	-3.8817	1.2547
N	4.6181	2.5409	-0.9573
N	-1.3346	1.8586	2.4764
C	1.303	0.6136	0.6862
C	1.531	-0.7019	0.9823
C	2.5522	0.1272	0.4418
C	3.8422	0.2767	-0.0189
C	2.117	-3.0123	1.3146
C	4.7425	-0.8103	-0.0338
C	4.271	1.5192	-0.5369
C	0.3931	1.7834	0.5133
C	1.1735	-1.9644	1.3972
C	-0.5938	1.8146	1.5995
C	-0.1561	-2.308	1.8681
C	1.2554	3.08	0.5752
C	-2.2898	-1.4926	2.4418
H	-2.8093	-2.1256	1.7206
H	-2.7626	-0.5151	2.4974
H	-2.2903	-1.967	3.4241
C	2.7071	4.3269	1.9296
H	3.5358	4.2512	1.2259
H	3.0597	4.247	2.9537
H	2.1533	5.2531	1.7802
N	1.5052	1.3874	-2.7572
N	-4.6075	2.7108	0.6891
C	0.705	1.498	-1.9409
H	-3.1951	4.58	-1.0995
O	-1.2321	3.3299	-2.4353
C	-4.2403	1.6738	0.3279
C	-0.3209	1.6925	-0.9065
C	-1.0974	2.9873	-1.2905
C	-1.2948	0.5632	-0.9025

C	-4.0147	0.5204	-0.1976
C	-2.7268	0.2017	-0.5814
C	-1.8084	-0.7999	-1.0328
N	-3.5486	-3.7851	-1.3833
C	-2.6754	-3.0287	-1.3832
H	2.0028	-2.5227	-3.0431
C	-1.5971	-2.104	-1.3916
C	-2.2905	4.6957	-0.2607
O	-1.5848	3.4614	-0.1082
C	-0.2855	-2.6024	-1.8006
O	-0.0476	-3.7302	-2.1671
C	-5.0407	-0.4573	-0.1117
O	0.6552	-1.64	-1.7316
H	-2.65	4.9441	0.734
C	1.9823	-2.0344	-2.0674
H	2.5633	-1.1144	-2.0939
H	-1.6046	5.4549	-0.6431
H	2.3783	-2.7181	-1.313
N	-5.9177	-1.2038	-0.0127
N	5.9576	-1.2465	0.2163

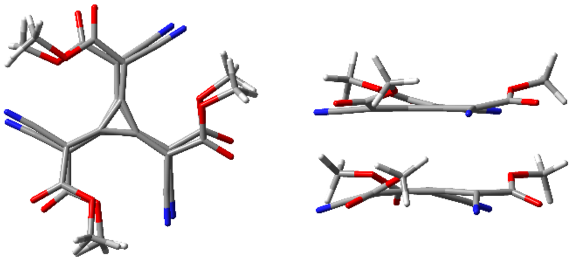

3 pimer

EE + G_{corr} (UwB97XD) = -2384.624745 Ha

O	-3.6301	2.2841	0.1947
O	0.0568	4.3918	0.3026
O	-1.8002	-2.5884	0.7669
O	-1.4662	2.819	0.7907
O	-3.9361	-2.0424	0.353
O	3.0474	-0.1723	0.6764
N	-4.0824	1.397	-0.0065
N	3.0934	2.7943	-0.1594
N	0.7151	-4.1199	-0.1407
C	0.4349	-0.5963	0.0499
C	-0.8852	-0.1196	0.0812
C	0.1877	0.7856	0.0627
C	0.6278	2.0933	0.0634
C	-3.2247	0.6238	0.036

C	-3.8291	0.3902	-0.0947
C	-2.5545	0.1633	-0.5675
C	-1.5773	-0.7705	-1.0118
N	-3.0415	-3.9092	-0.8203
C	-2.2525	-3.0819	-1.0071
H	2.2127	-2.5564	-3.1943
C	-1.2728	-2.0924	-1.2455
C	-2.3455	4.7858	-0.4503
O	-1.5932	3.5717	-0.2339
C	0.041	-2.5595	-1.6516
O	0.3525	-3.7392	-1.7353
C	-4.7484	-0.6719	0.0538
O	0.8804	-1.565	-1.9378
H	-2.6782	5.0932	0.5365
C	2.2184	-1.9357	-2.2974
H	2.7358	-0.9994	-2.4921
H	-1.6909	5.5371	-0.8918
H	2.698	-2.4703	-1.4758
N	-5.5181	-1.5273	0.1859
N	5.4899	-1.6948	-0.0558

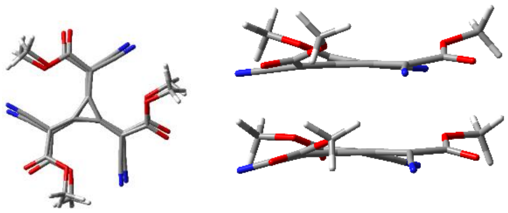

3 pimer SMD(water)

EE + G_{corr} (UwB97XD) = -2384.847129 Ha

O	-4.3278	0.9814	-0.6561
O	1.2057	-4.1256	-0.1586
O	0.7398	3.1667	0.0447
O	2.1649	-2.1957	0.4689
O	2.8724	3.2093	-0.6545
O	-3.2092	-0.7525	0.2278
N	4.0719	0.003	-0.7341
N	-2.1491	-3.5927	-0.614
N	-2.1385	3.5721	-1.1494
C	-0.7879	0.4419	-0.2953
C	0.6133	0.4362	-0.2624
C	-0.0944	-0.7711	-0.1886
C	-0.0877	-2.141	-0.1132
C	3.0351	0.4678	-0.5201

C	-0.2577	3.2239	0.3663	C	1.1422	-2.9262	0.0492
C	1.9973	2.4393	-0.0702	C	-1.2508	-2.9068	-0.37
C	1.3468	-1.6315	0.0295	C	-1.9768	1.1183	-0.4013
C	-2.2373	-0.3924	0.1128	C	1.7984	1.1253	-0.3119
C	0.9574	-2.992	-0.0739	C	-2.0258	2.4788	-0.7902
C	-2.7659	-1.7326	0.3931	C	1.8707	2.5914	-0.3376
C	2.7787	-1.4268	0.2781	C	-3.2843	0.4588	-0.3045
C	-2.2249	-3.904	1.0918	C	0.7007	4.6012	-0.0068
H	-2.7598	-3.9021	2.0463	H	1.5551	5.0211	0.5233
H	-1.3136	-4.4949	1.1506	H	-0.2286	4.8837	0.4794
H	-2.8871	-4.2996	0.3208	H	0.705	4.9338	-1.0458
C	-2.3794	3.8474	1.1446	C	3.4256	-2.8712	0.5977
H	-2.0707	4.3188	2.0825	H	3.3102	-3.7748	1.1954
H	-3.3431	3.354	1.2488	H	4.0846	-2.1644	1.0939
H	-2.4242	4.6113	0.3675	H	3.8112	-3.1242	-0.3911
C	4.4069	0.1098	0.9749	C	-4.4359	-1.4946	0.3091
H	4.6955	-0.377	1.9114	H	-5.2091	-0.8942	0.7874
H	4.465	1.1928	1.0581	H	-4.2059	-2.3716	0.9075
H	5.0612	-0.2476	0.1789	H	-4.7567	-1.7881	-0.6915
H	4.6406	0.9287	-3.5362	N	4.0156	-0.0704	2.6988
H	4.306	1.5253	-1.8857	N	-1.9784	4.0286	2.2603
C	4.3517	0.645	-2.5227	N	-2.5458	-3.2022	2.7833
H	5.0494	-0.1004	-2.1354	C	2.9945	0.4695	2.7465
N	2.6749	3.001	-3.8043	C	-1.9294	2.8904	2.4567
O	3.0276	0.1152	-2.5245	C	-1.5766	-2.5775	2.8658
C	1.6463	2.6077	-3.4583	O	3.0322	3.2402	2.7635
O	3.7564	-1.711	-3.6143	O	-4.3443	1.5733	2.7269
C	2.8581	-1.059	-3.1374	O	0.7844	-3.9759	3.2244
O	-0.6056	4.3109	-3.4883	C	1.7923	1.2157	2.8063
C	0.3461	2.1597	-3.1008	C	-1.9724	1.4955	2.6997
C	-0.7067	3.1953	-3.0358	C	-0.3388	-1.8988	2.9814
C	1.4333	-1.4527	-3.1449	C	0.5612	0.6147	2.8535
C	0.0439	0.8285	-3.0304	C	-0.2452	-0.5326	2.9178
C	0.4348	-0.5244	-3.047	C	-0.8367	0.7363	2.8131
C	1.1577	-2.8065	-3.4773	H	-5.216	-0.91	3.0399
O	-1.7895	2.739	-2.4014	H	3.3815	-3.4481	3.3935
N	0.971	-3.8976	-3.8044	H	1.2661	5.2353	2.7403
C	-0.9322	-0.1866	-3.0148	C	1.9718	2.6697	2.948
H	-2.6026	4.5865	-1.9421	C	-3.3184	0.956	2.9517
C	-2.9101	3.6198	-2.3461	C	0.8093	-2.7606	3.3061
H	-3.3278	3.7541	-3.3454	O	-3.2884	-0.25	3.5001
C	-2.2379	-0.5882	-3.0604	O	1.8515	-2.0722	3.7487
H	-3.6319	3.1233	-1.7019	O	0.8666	3.2791	3.3524
O	-1.6544	-2.7463	-2.4385	C	-4.5476	-0.816	3.8946
C	-3.2844	0.3242	-3.3633	C	2.9864	-2.8287	4.1975
H	-1.0502	-4.5521	-1.8024	C	0.9626	4.6845	3.6295
C	-2.608	-2.0188	-3.0255	H	-4.3086	-1.7969	4.2962
N	-4.1477	1.0281	-3.6656	H	3.7228	-2.0895	4.5004

C	-1.8568	-4.1579	-2.416
H	-1.7898	-4.5598	-3.4286
O	-3.6376	-2.4758	-3.4621
H	-2.8373	-4.3857	-1.993

H	-0.0351	4.9857	3.9368
H	-5.0072	-0.1917	4.662
H	1.6767	4.8531	4.4366
H	2.7013	-3.4525	5.0457

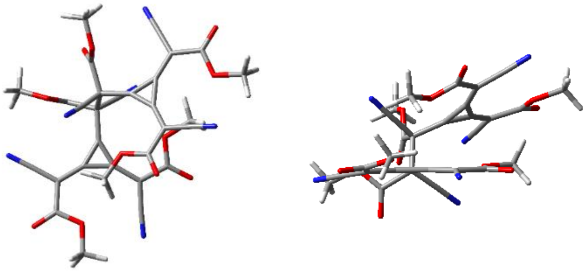

3 sigma dimer

EE + G_{corr} (RwB97XD) = -2384.647395 Ha

O	1.2591	3.7072	-0.4707
O	6.2484	-0.3211	-0.5383
O	-0.6624	-1.3163	1.83
O	4.6507	-1.822	-0.046
O	-0.0934	-3.3632	2.5595
O	1.9861	3.0547	1.546
N	3.3011	-3.838	1.8753
N	4.59	2.8421	-0.7613
N	-0.9587	1.6767	2.6626
C	1.452	0.4771	0.5279
C	1.8151	-0.7917	0.9068
C	2.7453	0.1082	0.2921
C	4.0222	0.4087	-0.1471
C	2.53	-2.9998	1.6773
C	5.0919	-0.5691	-0.2612
C	4.334	1.7435	-0.5024
C	0.4633	1.5983	0.4645
C	1.5364	-2.0042	1.4901
C	-0.363	1.6102	1.683
C	0.209	-2.3271	2.0108
C	1.2785	2.9268	0.4367
C	-1.9917	-1.5455	2.289
H	-2.5018	-2.2516	1.6307
H	-2.4853	-0.5764	2.2535
H	-1.9833	-1.9333	3.3088
C	5.6234	-2.8545	-0.1034
H	6.003	-2.9643	-1.1231
H	5.1053	-3.7526	0.2255

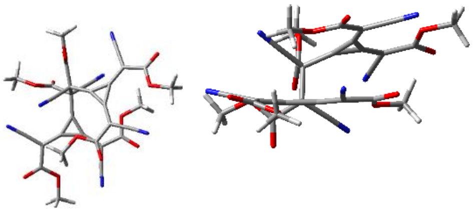

3 sigma dimer SMD(water)

EE + G_{corr} (RwB97XD) = -2384.859351 Ha

O	1.3266	3.8006	-0.3567
O	5.9537	-0.4917	-0.6862
O	-0.9598	-1.1465	2.0213
O	4.5667	-1.8274	0.4687
O	-0.6293	-3.3581	2.217
O	1.8982	3.1357	1.7112
N	2.5931	-4.0972	1.3432
N	4.4015	2.6414	-0.9904
N	-1.2532	1.8932	2.5562
C	1.3138	0.5693	0.7104
C	1.5514	-0.7433	1.0086
C	2.5698	0.0961	0.4644
C	3.8394	0.3246	-0.0254
C	1.9742	-3.119	1.3755
C	4.8831	-0.6761	-0.1213
C	4.1424	1.5985	-0.5574
C	0.4027	1.7385	0.5375
C	1.135	-1.9848	1.4424
C	-0.5541	1.8031	1.649
C	-0.2133	-2.2462	1.9201
C	1.2658	3.0383	0.5707
C	-2.3165	-1.3288	2.4506
H	-2.8611	-1.9482	1.7352
H	-2.7459	-0.3309	2.4871
H	-2.3433	-1.7868	3.4401
C	5.5133	-2.8964	0.3406
H	5.6629	-3.1452	-0.711
H	5.0681	-3.7377	0.8653

H	6.4601	-2.6342	0.5632	H	6.4633	-2.6219	0.8009
C	2.8032	4.2292	1.6323	C	2.769	4.2788	1.8763
H	3.5321	4.2296	0.8209	H	3.5558	4.2448	1.123
H	3.2975	4.1595	2.5988	H	3.1834	4.1757	2.875
H	2.1749	5.1209	1.5834	H	2.1866	5.1955	1.7903
N	1.1222	1.2057	-2.9221	N	1.4517	1.3782	-2.7587
N	-4.6569	2.9887	0.3888	N	-4.46	2.6872	0.8875
C	0.4343	1.3158	-2.01	C	0.6701	1.4617	-1.9215
H	-3.0861	4.6243	-0.6499	H	-3.2021	4.5483	-1.0057
O	-1.5213	3.2249	-2.2052	O	-1.3058	3.2545	-2.3875
C	-4.3634	1.8837	0.2117	C	-4.1661	1.6684	0.4209
C	-0.4426	1.5244	-0.8466	C	-0.3393	1.6403	-0.8678
C	-1.2127	2.8538	-1.1111	C	-1.1263	2.9336	-1.242
C	-1.4817	0.4503	-0.7519	C	-1.3122	0.5085	-0.8666
C	-4.0462	0.5219	-0.0157	C	-3.8621	0.4006	-0.1215
C	-2.783	0.1581	-0.4492	C	-2.5886	0.1221	-0.5744
C	-1.8919	-0.8443	-0.9589	C	-1.6003	-0.8239	-0.9826
N	-3.4911	-3.9316	-1.5748	N	-2.7611	-4.1322	-0.6205
C	-2.6933	-3.103	-1.4605	C	-2.1197	-3.204	-0.881
H	1.8734	-2.462	-3.1437	H	2.2396	-2.4997	-3.1743
C	-1.6609	-2.1321	-1.3805	C	-1.2434	-2.1397	-1.1955
C	-2.1671	4.7202	-0.0757	C	-2.328	4.7576	-0.3913
O	-1.5139	3.4521	0.027	O	-1.5781	3.5419	-0.1801
O	-6.2596	-0.1383	0.5376	O	-5.9935	-0.4053	0.5109
C	-0.3471	-2.5809	-1.8415	C	0.0898	-2.5538	-1.6026
O	-0.0967	-3.6903	-2.2575	O	0.4502	-3.7214	-1.6692
C	-5.1157	-0.429	0.2503	C	-4.9348	-0.5756	-0.08
H	-6.5283	-2.5631	-0.2651	H	-6.6117	-2.3286	-1.1481
O	0.577	-1.6055	-1.7664	O	0.8908	-1.5354	-1.9144
H	-2.402	5.0031	0.947	H	-2.623	5.0853	0.6009
C	1.8952	-1.959	-2.1758	C	2.2364	-1.8734	-2.2812
O	-4.6919	-1.7037	0.1751	O	-4.6695	-1.6769	-0.7822
H	2.4417	-1.0209	-2.2474	H	2.728	-0.9256	-2.4856
C	-5.6714	-2.7078	0.3963	C	-5.6647	-2.7085	-0.7628
H	-1.4845	5.4347	-0.5417	H	-1.6833	5.4954	-0.8691
H	-5.1737	-3.6473	0.1672	H	-5.2818	-3.4925	-1.4104
H	2.359	-2.6116	-1.4331	H	2.7357	-2.39	-1.4596
H	-6.0162	-2.6813	1.4337	H	-5.7973	-3.0903	0.2506

CHAPTER 5: CONCLUSIONS

Main-chain organometallic polymers are one of many possible routes for the incorporation of delocalized, conductive clusters into crystalline frameworks. The surprising ability to reversibly modulate the NHC ligands of these clusters in excess is still underexplored. The development of many crystalline superatomic frameworks can be imagined with such a wide selection of carbenes and carbene stabilized clusters. The recognition of this new class of functional MCOPs will likely depend on the development of the first SCXRD quality structure of this new class of materials. We have discovered promising mechanisms to this end including modular NHC ligands and soluble superatomic ion pairs but have yet to realize a highly crystalline MCOP.

In light of this pursuit, there are a few factors yet to be considered. The fully reduced MCOPs are highly sensitive, often combusting when exposed to air. This makes them very difficult to investigate in the solid state and is a strong reason to repeat some of these experiments using the clusters in different oxidation states. M_4S_4 MCOPs are also formed very fast even at room temperature, inhibiting many of the principals of slow growth necessary for crystallization. It is common to use solvothermal chemistry techniques to slow down the process with modulation or slow activation of the linker. The bis-imidazoles herein required deprotonation *ex situ* to remove the insoluble bromide salts that formed by filtration before forming the polymer. Formation of the carbene in situ, dramatically slowing the formation of MCOP, could improve crystallinity. This could be achieved through proper selection of soluble organic counterions and soluble bases, like KOtBu, along with modifying the sterics of the imidazoles. Alternatively, we may be able to modulate the free carbene by using soluble capping metal complexes, fullerenes, or even through the reversible self-dimerization of carbenes that can be tuned with both sterics and temperature. Even so, our SCXRD of our model NHC ligated cubane cluster implies there may be more flexibility in the organometallic bond with the fully reduced cubanes than anticipated. The investigation of other strong bonding linkers or cluster oxidation states must, therefore, be explored. We also continue to investigate other linkers including isocyanide linkers, imidazolates, phosphines, and pyridines. Single metal ions have coordination environments dictated by their ligands which introduces inherent challenges when designing coordination frameworks. Fatefully clusters as superatoms can share similar challenges since their nuclearity and incidentally the coordination environment of the cluster itself is often determined by that of the ligands. As underlined by our recent isolation of an isocyanide stabilized Co_4S_2 cluster from that of the cubane cluster. We continue to investigate the synthesis of clusters stabilized with similar ligands and coordination geometries to those used in highly crystalline single-metal ion coordination polymers. Isolation of such clusters enables their use as superatoms in the development of cluster-based coordination networks analogous to those based upon single-metal ions for which the synthetic strategies are well established.

Our synthetic and computational pursuit of highly stable [3]radialenes is ongoing. Radical stability scores primarily increased by buried volume calculations have been ineffective at predicting stable [3]radialenes radicals, but Mulliken spin density alone has so far been a rapid and accurate predictor. The tri-pyridinium is computationally promising from a redox potential and spin density analysis and is being synthesized. Other metrics of stability continue to be explored. Calculations used for better understanding the dimerization modes of [3]radialenes are also helping identify highly localized spin density structures with preferred sigma dimerization to be used for reversible and controllable crosslinking in polymers.

REFERENCES

(1) Hoffmann, R. How Should Chemists Think? *Sci Am.* **1993**, *268*(2), 66-73.

(2) Yaghi, O. M.; Kalmutzki, M. J.; Diercks, C. S. Metal-Organic Frameworks. In *Introduction to Reticular Chemistry*; Wiley-VCH: **2019**; pp 3-29.

(3) Yaghi, O. M. Reticular Chemistry in All Dimensions. *ACS Cent Sci.* **2019**, *5* (8), 1295-1300. DOI: 10.1021/acscentsci.9b00750.

(4) Ockwig, N. W.; Delgado-Friedrichs, O.; O'Keeffe, M.; Yaghi, O. M. Reticular Chemistry: Occurrence and Taxonomy of Nets and Grammar for the Design of Frameworks. *Acc Chem Res.* **2005**, *38* (3), 176-182. DOI: 10.1021/ar020022l.

(5) Yaghi, O. M. Reticular Chemistry-Construction, Properties, and Precision Reactions of Frameworks. *J Am Chem Soc.* **2016**, *138* (48), 15507-15509. DOI: 10.1021/jacs.6b11821.

(6) Diercks, C. S.; Yaghi, O. M. The Atom, the Molecule, and the Covalent Organic Framework. *Sci.* **2017**, *355* (6328), eaal1585. DOI: 10.1126/science.aal1585.

(7) Yaghi, O. M.; Kalmutzki, M. J.; Diercks, C. S. Front Matter. In *Introduction to Reticular Chemistry*, Wiley-VCH: **2019**; pp xxiii-xxv.

(8) Wells, A. F. The Geometrical Basis of Crystal Chemistry. Part 1. *Acta Crystallographica* **1954**, *7* (8-9), 535-544. DOI: 10.1107/S0365110X5400182X.

(9) Furukawa, H.; Cordova, K. E.; O'Keeffe, M.; Yaghi, O. M. The Chemistry and Applications of Metal-Organic Frameworks. *Sci.* **2013**, *341* (6149), 1230444. DOI: 10.1126/science.1230444.

(10) Park, K. S.; Ni, Z.; Côté, A. P.; Choi, J. Y.; Huang, R.; Uribe-Romo, F. J.; Chae, H. K.; O'Keeffe, M.; Yaghi, O. M. Exceptional Chemical and Thermal Stability of Zeolitic Imidazolate Frameworks. *PNAS.* **2006**, *103* (27), 10186-10191. DOI: 10.1073/pnas.0602439103.

(11) Geng, K.; He, T.; Liu, R.; Dalapati, S.; Tan, K. T.; Li, Z.; Tao, S.; Gong, Y.; Jiang, Q.; Jiang, D. Covalent Organic Frameworks: Design, Synthesis, and Functions. *Chem Rev.* **2020**, *120* (16), 8814-8933. DOI: 10.1021/acs.chemrev.9b00550.

(12) Jiang, H.; Alezi, D.; Eddaoudi, M. A Reticular Chemistry Guide for the Design of Periodic Solids. *Nat Rev Mater.* **2021**, *6* (6), 466-487. DOI: 10.1038/s41578-021-00287-y.

(13) Li, H.; Eddaoudi, M.; O'Keeffe, M.; Yaghi, O. M. Design and Synthesis of an Exceptionally Stable and Highly Porous Metal-organic Framework. *Nat.* **1999**, *402* (6759), 276-279. DOI: 10.1038/46248.

(14) Davis, M. E. Ordered Porous Materials for Emerging Applications. *Nat.* **2002**, *417* (6891), 813-821. DOI: 10.1038/nature00785.

(15) Ding, M.; Cai, X.; Jiang, H. L. Improving MOF Stability: Approaches and Applications. *Chem Sci.* **2019**, *10* (44), 10209-10230. DOI: 10.1039/c9sc03916c

(16) Doud, E. A.; Voevodin, A.; Hochuli, T. J.; Champsaur, A. M.; Nuckolls, C.; Roy, X. Superatoms in Materials Science. *Nat. Rev. Mater.* **2020**, *5* (5), 371-387. DOI: 10.1038/s41578-019-0175-3.

(17) Steigerwald, M. L. Clusters as Small Solids. *Polyhedron* **1994**, *13* (8), 1245-1252. DOI: 10.1016/S0277-5387(00)80258-2.

(18) Bergeron, D. E.; Castleman, A. W.; Morisato, T.; Khanna, S. N. Formation of $Al_{13}I^-$: Evidence for the Superhalogen Character of Al_{13}. *Sci.* **2004**, *304* (5667), 84-87. DOI: 10.1126/science.1093902.

(19) Dance, I.; Fisher, K. Metal Chalcogenide Cluster Chemistry. *Prog Inorg Chem.* 1994; pp 637-803. DOI: 10.1002/9780470166420.ch9

(20) Wang, D.; Astruc, D. The Recent Development of Efficient Earth-abundant Transition-metal Nanocatalysts. *ChemSoc Rev.* **2017**, *46* (3), 816-854, 10.1039/C6CS00629A. DOI: 10.1039/C6CS00629A.

(21) Valdez, C. E.; Smith, Q. A.; Nechay, M. R.; Alexandrova, A. N. Mysteries of Metals in Metalloenzymes. *Acc. Chem. Res.* **2014**, *47* (10), 3110-3117. DOI: 10.1021/ar500227u.

(22) Foster, S. L.; Bakovic, S. I. P.; Duda, R. D.; Maheshwari, S.; Milton, R. D.; Minteer, S. D.; Janik, M. J.; Renner, J. N.; Greenlee, L. F. Catalysts for Nitrogen Reduction to Ammonia. *Nat Catal.* **2018**, *1* (7), 490-500. DOI: 10.1038/s41929-018-0092-7.

(23) Rohde, M.; Grunau, K.; Einsle, O. CO Binding to the FeV Cofactor of CO-Reducing Vanadium Nitrogenase at Atomic Resolution. *Angew Chem Int Ed.* **2020**, *59* (52), 23626-23630. DOI: 10.1002/anie.202010790.

(24) Kirby, A. J. Enzyme Mechanisms, Models, and Mimics. *Angew Chem Int Ed Engl.* **1996**, *35* (7), 706-724. DOI: 10.1002/anie.199607061.

(25) Raugei, S.; Seefeldt, L. C.; Hoffman, B. M. Critical Computational Analysis Illuminates the Reductive-Elimination Mechanism that Activates Nitrogenase for N_2 Reduction. *PNAS* **2018**, *115* (45), E10521-E10530. DOI: 10.1073/pnas.1810211115.

(26) Hu, Y.; Lee, C. C.; Grosch, M.; Solomon, J. B.; Weigand, W.; Ribbe, M. W. Enzymatic Fischer-Tropsch-Type Reactions. *Chem Rev.* **2023**, *123* (9), 5755-5797. DOI: 10.1021/acs.chemrev.2c00612.

(27) Sickerman, N. S.; Tanifuji, K.; Hu, Y.; Ribbe, M. W. Synthetic Analogues of Nitrogenase Metallocofactors: Challenges and Developments. *Chem Eur J.* **2017**, *23* (51), 12425-12432. DOI: 10.1002/chem.201702496.

(28) Nath, I.; Chakraborty, J.; Verpoort, F. Metal Organic Frameworks Mimicking Natural Enzymes: a Structural and Functional Analogy. *Chem Soc Rev.* **2016**, *45* (15), 4127-4170, 10.1039/C6CS00047A. DOI: 10.1039/C6CS00047A.

(28) Chen, L.; Xu, Q. Metal-Organic Framework Composites for Catalysis. *Matter.* **2019**, *1* (1), 57-89. DOI: 10.1016/j.matt.2019.05.018.

(30) Shu, Y.; Liang, W.; Huang, J. Heterogeneity in Enzyme/Metal–organic Framework Composites for CO_2 Transformation Reactions. *Green Chem.* **2023**, *25* (11), 4196-4221, 10.1039/D2GC04682B. DOI: 10.1039/D2GC04682B.

(31) Kadota, K.; Chen, T.; Gormley, E. L.; Hendon, C. H.; Dincă, M.; Brozek, C. K. Electrically Conductive [Fe_4S_4]-based Organometallic Polymers. *Chem Sci.* **2023**, *14* (41), 11410-11416. DOI: 10.1039/D3SC02195E.

(32) Ji, Z.; Trickett, C.; Pei, X.; Yaghi, O. M. Linking Molybdenum–Sulfur Clusters for Electrocatalytic Hydrogen Evolution. *J Am Chem Soc.* **2018**, *140* (42), 13618-13622. DOI: 10.1021/jacs.8b09807.

(33) Lee, S. C.; Lo, W.; Holm, R. H. Developments in the Biomimetic Chemistry of Cubane-Type and Higher Nuclearity Iron–Sulfur Clusters. *Chem Rev.* **2014**, *114* (7), 3579-3600. DOI: 10.1021/cr4004067.

(34) Lamiel, C.; Hussain, I.; Rabiee, H.; Ogunsakin, O. R.; Zhang, K. Metal-organic Framework-derived Transition Metal Chalcogenides (S, Se, and Te): Challenges, Recent Progress, and Future Directions in Electrochemical Energy Storage and Conversion Systems. *Coord Chem Rev.* **2023**, *480*, 215030. DOI: 10.1016/j.ccr.2023.215030.

(35) Bigness, A.; Vaddypally, S.; Zdilla, M. J.; Mendoza-Cortes, J. L. Ubiquity of cubanes in bioinorganic relevant compounds. *Coord Chem Rev.* **2022**, *450*, 214168. DOI: 10.1016/j.ccr.2021.214168.

(36) Flint, D. H.; Allen, R. M. Iron−Sulfur Proteins with Nonredox Functions. *Chem Rev.* **1996**, *96* (7), 2315-2334. DOI: 10.1021/cr950041r.

(37) Holm, R. H.; Lo, W. Structural Conversions of Synthetic and Protein-Bound Iron–Sulfur Clusters. *Chem. Rev.* **2016**, *116* (22), 13685-13713. DOI: 10.1021/acs.chemrev.6b00276.

(38) Pinkard, A.; Champsaur, A. M.; Roy, X. Molecular Clusters: Nanoscale Building Blocks for Solid-State Materials. *Acc Chem Res* **2018**, *51* (4), 919-929. DOI: 10.1021/acs.accounts.8b00016.

(39) Han, X.-B.; Li, Y.-G.; Zhang, Z.-M.; Tan, H.-Q.; Lu, Y.; Wang, E.-B. Polyoxometalate-Based Nickel Clusters as Visible Light-Driven Water Oxidation Catalysts. *J Am Chem Soc.* **2015**, *137* (16), 5486-5493. DOI: 10.1021/jacs.5b01329.

(40) Laursen, A. B.; Kegnæs, S.; Dahl, S.; Chorkendorff, I. Molybdenum Sulfides—Efficient and Viable Materials for Electro - and Photoelectrocatalytic Hydrogen Evolution. *Energy Environ Sci.* **2012**, *5* (2), 5577-5591. DOI: 10.1039/C2EE02618J.

(41) Darii, M.; van Leusen, J.; Kravtsov, V. C.; Chumakov, Y.; Krämer, K.; Decurtins, S.; Liu, S.-X.; Kögerler, P.; Baca, S. G. $\{Mn_6^{III}Mn^{IV}Dy_2^{III}\}$ Single-Molecule

Magnet Based on Cubane Subunits. *Cryst Growth Des.* **2023**, *23* (9), 6944-6952. DOI: 10.1021/acs.cgd.3c00783.

(42) Gu, W.; Milton, R. D. Natural and Engineered Electron Transfer of Nitrogenase. *Chem.* **2020**, *2* (2), 322-346.

(43) Tanifuji, K.; Ohki, Y. Metal–Sulfur Compounds in N_2 Reduction and Nitrogenase-Related Chemistry. *Chem. Rev.* **2020**, *120* (12), 5194-5251. DOI: 10.1021/acs.chemrev.9b00544.

(44) Hu, Y.; Lee, C. C.; Ribbe, M. W. Extending the Carbon Chain: Hydrocarbon Formation Catalyzed by Vanadium/Molybdenum Nitrogenases. *Sci.* **2011**, *333* (6043), 753-755. DOI: 10.1126/science.1206883.

(45) Noodleman, L. Fe_4S_4 clusters as Small Molecule Catalysts. *Nat Catal.* **2018**, *1* (6), 383-384. DOI: 10.1038/s41929-018-0099-0.

(46) Carter, C. W.; Freer, S.; Xuong, N. H.; Alden, R.; Kraut, J. Structure of the Iron-Sulfur Cluster in the Chromatium Iron Protein at 2.25±Resolution. In *COLD SPRING HARB SYM*. 1972; Cold Spring Harbor Laboratory Press: Vol. 36, pp 381-385.

(47) Herskovitz, T.; Averill, B.; Holm, R.; Ibers, J. A.; Phillips, W.; Weiher, J. Structure and properties of a synthetic analogue of bacterial iron-sulfur proteins. *PNAS.* **1972**, *69* (9), 2437-2441.

(48) Scott, T. A.; Berlinguette, C. P.; Holm, R. H.; Zhou, H. Initial synthesis and structure of an all-ferrous analogue of the fully reduced $[Fe_4S_4]^0$ cluster of the nitrogenase iron protein. *PNAS.* **2005**, *102* (28), 9741–9744. DOI: 10.1073/pnas.0504258102.

(49) Yoo, S. J.; Angove, H. C.; Burgess, B. K.; Hendrich, M. P.; Münck, E. Mössbauer and Integer-Spin EPR Studies and Spin-Coupling Analysis of the $[4Fe\text{-}4S]^0$ Cluster of the Fe Protein from Azotobacter vinelandii Nitrogenase. *J Am Chem Soc.* **1999**, *121* (11), 2534-2545. DOI: 10.1021/ja9837405.

(50) Deng, L.; Holm, R. H. Stabilization of Fully Reduced Iron−Sulfur Clusters by Carbene Ligation: The $[Fe_nS_n]^0$ Oxidation Levels (n = 4, 8). *J Am Chem Soc.* **2008**, *130* (30), 9878-9886. DOI: 10.1021/ja802111w.

(51) Stillman, M. Biological Inorganic Chemistry. Structure and Reactivity. Edited by Ivano Bertini, Harry B. Gray, Edward I. Stiefel and Joan S. Valentine. *Angew Chem Int Ed.* **2007**, *46* (46), 8741-8742. DOI: 10.1002/anie.200785504.

(52) Bertini, I. *Biological inorganic chemistry: structure and reactivity*; University Science Books, 2007.

(53) Smith, C. A.; Narouz, M. R.; Lummis, P. A.; Singh, I.; Nazemi, A.; Li, C. H.; Crudden, C. M. N-Heterocyclic Carbenes in Materials Chemistry. *Chem Rev* **2019**, *119* (8), 4986-5056. DOI: 10.1021/acs.chemrev.8b00514.

(53) Öfele, K. 1,3-Dimethyl-4-imidazolinyliden-(2)-pentacarbonylchrom ein neuer übergangsmetall-carben-komplex. *J. Organomet. Chem.* **1968**, *12* (3), 42-43. DOI: 10.1016/S0022-328X(00)88691-X.

(55) Wanzlick, H.-W.; Schönherr, H.-J. Direct Synthesis of a Mercury Salt-Carbene Complex. *Angew Chem Int Ed Engl.* **1968**, *7* (2), 141-142. DOI: 10.1002/anie.196801412.

(56) Igau, A.; Grutzmacher, H.; Baceiredo, A.; Bertrand, G. Analogous α,α'-Bis-Carbenoid, Triply Bonded Species: Synthesis of a Stable λ^3-Phosphinocarbene-λ^5-Phosphaacetylene. *J Am Chem Soc.* **1988**, *110* (19), 6463-6466. DOI: 10.1021/ja00227a028.

(57) Arduengo, A. J., III; Harlow, R. L.; Kline, M. A stable crystalline carbene. *J Am Chem Soc.* **1991**, *113* (1), 361-363. DOI: 10.1021/ja00001a054.

(58) Dröge, T.; Glorius, F. The Measure of All Rings—N-Heterocyclic Carbenes. *Angew Chem Int Ed.* **2010**, *49* (39), 6940-6952. DOI: 10.1002/anie.201001865.

(59) Hopkinson, M. N.; Richter, C.; Schedler, M.; Glorius, F. An Overview of N-heterocyclic Carbenes. *Nat.* **2014**, *510* (7506), 485-496. DOI: 10.1038/nature13384.

(60) Nelson, D. J.; Nolan, S. P. Quantifying and Understanding the Electronic Properties of N-heterocyclic Carbenes. *Chem Soc Rev.* **2013**, *42* (16), 6723-6753. DOI: 10.1039/C3CS60146C.

(61) Morán-González, L.; Pedregal, J. R.-G.; Besora, M.; Maseras, F. Understanding the Binding Properties of N-heterocyclic Carbenes through BDE Matrix App. *Eur J Inorg Chem.* **2022**, (3), e202100932. DOI: 10.1002/ejic.202100932.

(62) Wanzlick, H. W. Aspects of Nucleophilic Carbene Chemistry. *Angew Chem Int Ed Engl.* **1962**, *1* (2), 75-80. DOI: 10.1002/anie.196200751.

(63) Heinemann, C.; Müller, T.; Apeloig, Y.; Schwarz, H. On the Question of Stability, Conjugation, and "Aromaticity" in Imidazol-2-ylidenes and Their Silicon Analogs. *J. Am. Chem. Soc.* **1996**, *118* (8), 2023-2038. DOI: 10.1021/ja9523294.

(64) Neilson, B. M.; Tennyson, A. G.; Bielawski, C. W. Advances in Bis(N-heterocyclic Carbene) Chemistry: New Classes of Structurally Dynamic Materials. *J Phys Org Chem.* **2012**, *25* (7), 531-543. DOI: 10.1002/poc.1961.

(65) Ibrahim, H.; Ilinca, A.; Perron, J. Energy Storage Systems—Characteristics and Comparisons. *Renew Sustain Energy Rev.* **2008**, *12* (5), 1221-1250. DOI: 10.1016/j.rser.2007.01.023.

(66) Cao, J.; Tian, J.; Xu, J.; Wang, Y. Organic Flow Batteries: Recent Progress and Perspectives. *Energy Fuels.* **2020**, *34* (11), 13384-13411. DOI: 10.1021/acs.energyfuels.0c02855.

(67) Winsberg, J.; Hagemann, T.; Janoschka, T.; Hager, M. D.; Schubert, U. S. Redox-Flow Batteries: From Metals to Organic Redox-Active Materials. *Angew Chem Int Ed.* **2017**, *56* (3), 686-711. DOI: 10.1002/anie.201604925.

(68) Minke, C.; Dorantes Ledesma, M. A. Impact of Cell Design and Maintenance Strategy on Life Cycle Costs of Vanadium Redox Flow Batteries. *J Energy Storage.* **2019**, *21*, 571-580. DOI: 10.1016/j.est.2018.12.019.

(69) Jin, S.; Jing, Y.; Kwabi, D. G.; Ji, Y.; Tong, L.; De Porcellinis, D.; Goulet, M.-A.; Pollack, D. A.; Gordon, R. G.; Aziz, M. J. A Water-Miscible Quinone Flow Battery with High Volumetric Capacity and Energy Density. *ACS Energy Lett.* **2019**, *4* (6), 1342-1348. DOI: 10.1021/acsenergylett.9b00739

(70) DeBruler, C.; Hu, B.; Moss, J.; Luo, J.; Liu, T. L. A Sulfonate-Functionalized Viologen Enabling Neutral Cation Exchange, Aqueous Organic Redox Flow Batteries toward Renewable Energy Storage. *ACS Energy Lett.* **2018**, *3* (3), 663-668. DOI: 10.1021/acsenergylett.7b01302.

(71) Hu, B.; Tang, Y.; Luo, J.; Grove, G.; Guo, Y.; Liu, T. L. Improved Radical Stability of Viologen Anolytes in Aqueous Organic Redox Flow Batteries. *Chem. Commun.* **2018**, *54* (50), 6871-6874. DOI: 10.1039/C8CC02336K.

(72) Luo, J.; Hu, B.; Debruler, C.; Liu, T. L. A π-Conjugation Extended Viologen as a Two-Electron Storage Anolyte for Total Organic Aqueous Redox Flow Batteries. *Angew Chem Int Ed.* **2018**, *57* (1), 231-235. DOI: 10.1002/anie.201710517.

(73) Pang, S.; Wang, X.; Wang, P.; Ji, Y. Biomimetic Amino Acid Functionalized Phenazine Flow Batteries with Long Lifetime at Near-Neutral pH. *Angew Chem Int Ed.* **2021**, *60* (10), 5289-5298. DOI: 10.1002/anie.202014610.

(74) Cannon, C. G.; Klusener, P. A. A.; Brandon, N. P.; Kucernak, A. R. J. Aqueous Redox Flow Batteries: Small Organic Molecules for the Positive Electrolyte Species. *ChemSusChem.* **2023**, *16* (18), DOI: 10.1002/cssc.202300303

(75) Emmel, D.; Kunz, S.; Blume, N.; Kwon, Y.; Turek, T.; Minke, C.; Schröder, D. Benchmarking Organic Active Materials for Aqueous Redox Flow Batteries in Terms of Lifetime and Cost. *Nat.Comm.* **2023**, *14* (1), 6672. DOI: 10.1038/s41467-023-42450-9.

(76) Wang, X.; Tang, W.; Loh, K. P. Para-Substituted Triphenylamine as a Catholyte for Zinc–Organic Aqueous Redox Flow Batteries. *ACS Appl. Energy Mater.* **2021**, *4* (4), 3612-3621. DOI: 10.1021/acsaem.1c00031.

(77) Fang, X.; Li, Z.; Zhao, Y.; Yue, D.; Zhang, L.; Wei, X. Multielectron Organic Redoxmers for Energy-Dense Redox Flow Batteries. *ACS Mat Lett.* **2022**, *4* (2), 277-306. DOI: 10.1021/acsmaterialslett.1c00668.

(78) Karpov, Y.; Kiriy, N.; Al-Hussein, M.; Hambsch, M.; Beryozkina, T.; Bakulev, V.; Mannsfeld, S. C. B.; Voit, B.; Kiriy, A. Hexacyano-[3]-radialene Anion-Radical Salts: A Promising Family of Highly Soluble p-Dopants. *Chem Commun.* **2018**, *54* (3), 307-310, DOI: 10.1039/C7CC08671G.

(79) Enomoto, T.; Kawase, T.; Kurata, H.; Oda, M. Hexaaryl[3]radialenes. *Tetrahedron Lett.* **1997**, *38* (15), 2693-2696. DOI: 10.1016/S0040-4039(97)00431-0.

(80) Turner, N. A.; Freeman, M. B.; Pratt, H. D.; Crockett, A. E.; Jones, D. S.; Anstey, M. R.; Anderson, T. M.; Bejger, C. M. Desymmetrized Hexasubstituted [3]Radialene Anions as Aqueous Organic Catholytes for Redox Flow Batteries. *Chem Commun.* **2020**, *56* (18), 2739-2742, DOI: 10.1039/C9CC08547E.

(81) Huang, R.-W.; Wei, Y.-S.; Dong, X.-Y.; Wu, X.-H.; Du, C.-X.; Zang, S.-Q.; Mak, T. C. W. Hypersensitive Dual-function Luminescence Switching of a Silver-chalcogenolate Cluster-based Metal–organic Framework. *Nat Chem.* **2017**, *9* (7), 689-697. DOI: 10.1038/nchem.2718.

(82) Poyatos, M.; Peris, E. Insights Into the Past and Future of Janus-di-N-heterocyclic Carbenes. *Dalton Trans.* **2021**, *50* (37), 12748-12763. DOI: 10.1039/D1DT02035H.

(83) Wang, Y.; Chang, J.-P.; Xu, R.; Bai, S.; Wang, D.; Yang, G.-P.; Sun, L.-Y.; Li, P.; Han, Y.-F. N-Heterocyclic Carbenes and Their Precursors in Functionalised Porous Materials. *Chem Soc Rev.* **2021**, *50* (24), 13559-13586. DOI: 10.1039/D1CS00296A.

(84) Boydston, A. J.; Williams, K. A.; Bielawski, C. W. A Modular Approach to Main-Chain Organometallic Polymers. *J Am Chem Soc.* **2005**, *127* (36), 12496-12497. DOI: 10.1021/ja054029k.

(85) Sun, Z.; Liu, Y.; Chen, J.; Huang, C.; Tu, T. Robust Iridium Coordination Polymers: Highly Selective, Efficient, and Recyclable Catalysts for Oxidative Conversion of Glycerol to Potassium Lactate with Dihydrogen Liberation. *ACS Catal.* **2015**, *5* (11), 6573-6578. DOI: 10.1021/acscatal.5b01782.

(86) Gonell, S.; Poyatos, M.; Peris, E. Main-Chain Organometallic Microporous Polymers Bearing Triphenylene–Tris(N-heterocyclic Carbene)–Gold Species: Catalytic Properties. *Chem Eur J.* **2014**, *20* (19), 5746-5751. DOI: 10.1002/chem.201400371

(87) Zhang, C.; Wang, J.-J.; Liu, Y.; Ma, H.; Yang, X.-L.; Xu, H.-B. Main-Chain Organometallic Microporous Polymers Based on Triptycene: Synthesis and Catalytic Application in the Suzuki–Miyaura Coupling Reaction. *Chem Eur J.* **2013**, *19* (16), 5004-5008. DOI: 10.1002/chem.201203975.

(88) Longevial, J.-F.; Lo, M.; Lebrun, A.; Laurencin, D.; Clément, S.; Richeter, S. Molecular Complexes and Main-Chain Organometallic Polymers Based on Janus Bis(Carbenes) Fused to Metalloporphyrins. *Dalton Trans.* **2020**, *49* (21), 7005-7014. DOI: 10.1039/D0DT00594K.

(89) Wang, Y.-T.; Chang, M.-T.; Lee, G.-H.; Peng, S.-M.; Chiu, C.-W. Planar Tris-N-heterocyclic Carbenes. *Chem Commun.* **2013**, *49* (65), 7258-7260, 10.1039/C3CC43278E. DOI: 10.1039/C3CC43278E.

(90) Choi, J.; Yang, H. Y.; Kim, H. J.; Son, S. U. Organometallic Hollow Spheres Bearing Bis(N-heterocyclic Carbene)–Palladium Species: Catalytic Application in Three-Component Strecker Reactions. *Angew Chem Int Ed.* **2010**, *49* (42), 7718-7722. DOI: 10.1002/anie.201003101.

(91) Wu, J.; Shen, L.; Duan, S.; Chen, Z.-N.; Zheng, Q.; Liu, Y.; Sun, Z.; Clark, J. H.; Xu, X.; Tu, T. Selective Catalytic Dehydrogenative Oxidation of Bio-Polyols to Lactic Acid. *Angew Chem Int Ed.* **2020**, *59* (33), 13871-13878. DOI: 10.1002/anie.202004174.

(92) Boydston, A. J.; Bielawski, C. W. Bis(imidazolylidene)s as Modular Building Blocks for Monomeric and Macromolecular Organometallic Materials. *Dalton Trans.* **2006**, (34), 4073-4077, 10.1039/B607696N. DOI: 10.1039/B607696N.

(93) Cabeza, J. A.; García-Álvarez, P. The N-heterocyclic Carbene Chemistry of Transition-Metal Carbonyl Clusters. *Chem Soc Rev.* **2011**, *40* (11), 5389-5405. DOI: 10.1039/C1CS15108H.

(94) Narouz, M. R.; Osten, K. M.; Unsworth, P. J.; Man, R. W. Y.; Salorinne, K.; Takano, S.; Tomihara, R.; Kaappa, S.; Malola, S.; Dinh, C.-T.; et al. N-heterocyclic Carbene-functionalized Magic-number Gold Nanoclusters. *Nat Chem.* **2019**, *11* (5), 419-425. DOI: 10.1038/s41557-019-0246-5.

(95) Narouz, M. R.; Takano, S.; Lummis, P. A.; Levchenko, T. I.; Nazemi, A.; Kaappa, S.; Malola, S.; Yousefalizadeh, G.; Calhoun, L. A.; Stamplecoskie, K. G.; et al. Robust, Highly Luminescent Au_{13} Superatoms Protected by N-heterocyclic Carbenes. *J Am Chem Soc.* **2019**, *141* (38), 14997-15002. DOI: 10.1021/jacs.9b07854.

(96) Ube, H.; Zhang, Q.; Shionoya, M. A Carbon-Centered Hexagold(I) Cluster Supported by N-heterocyclic Carbene Ligands. *Organometallics* **2018**, *37* (13), 2007-2009. DOI: 10.1021/acs.organomet.8b00291.

(97) Durham, J. L.; Wilson, W. B.; Huh, D. N.; McDonald, R.; Szczepura, L. F. Organometallic Rhenium(III) Chalcogenide Clusters: Coordination of N-heterocyclic Carbenes. *Chem Commun.* **2015**, *51* (52), 10536-10538. DOI: 10.1039/C5CC03215F.

(98) Kühnel, E.; Shishkov, I. V.; Rominger, F.; Oeser, T.; Hofmann, P. Synthesis and Structures of Copper(I) Complexes with Phosphino-functionalized N-heterocyclic Carbenes (NHCP) and Bis-N-heterocyclic Carbenes (Bis-NHC). *Organometallics* **2012**, *31* (22), 8000-8011. DOI: 10.1021/om300701u.

(99) Chakraborty, I.; Pradeep, T. Atomically Precise Clusters of Noble Metals: Emerging Link between Atoms and Nanoparticles. *Chem Rev.* **2017**, *117* (12), 8208-8271. DOI: 10.1021/acs.chemrev.6b00769.

(100) Fuhr, O.; Dehnen, S.; Fenske, D. Chalcogenide Clusters of Copper and Silver from Silylated Chalcogenide Sources. *Chem Soc Rev.* **2013**, *42* (4), 1871-1906. DOI: 10.1039/C2CS35252D.

(101) Lee, S. C.; Holm, R. H. Nonmolecular Metal Chalcogenide/Halide Solids and Their Molecular Cluster Analogues. *Angew Chem Int Ed Engl.* **1990**, *29* (8), 840-856. DOI: 10.1002/anie.199008401.

(102) Peng, R.; Li, M.; Li, D. Copper(I) halides: A Versatile Family in Coordination Chemistry and Crystal Engineering. *Coord Chem Rev.* **2010**, *254* (1), 1-18. DOI: 10.1016/j.ccr.2009.10.003.

(103) Kalmutzki, M. J.; Hanikel, N.; Yaghi, O. M. Secondary Building Units as the Turning Point in the Development of the Reticular Chemistry of MOFs. *Sci Adv.* **2018**, *4* (10), eaat9180. DOI: 10.1126/sciadv.aat9180.

(104) Stiebritz, M. T.; Hiller, C. J.; Sickerman, N. S.; Lee, C. C.; Tanifuji, K.; Ohki, Y.; Hu, Y. Ambient conversion of CO_2 to hydrocarbons by biogenic and synthetic $[Fe_4S_4]$ clusters. *Nat. Catal.* **2018**, *1* (6), 444-451. DOI: 10.1038/s41929-018-0079-4.

(105) Wang, S.-S.; Yang, G.-Y. Recent Advances in Polyoxometalate-Catalyzed Reactions. *Chem. Rev.* **2015**, *115* (11), 4893-4962. DOI: 10.1021/cr500390v.

(106) Gray, T. G.; Rudzinski, C. M.; Meyer, E. E.; Holm, R. H.; Nocera, D. G. Spectroscopic and Photophysical Properties of Hexanuclear Rhenium(III) Chalcogenide Clusters. *J Am Chem Soc.* **2003**, *125* (16), 4755-4770. DOI: 10.1021/ja0286371.

(107) Morgenstern, D. A.; Ferrence, G. M.; Washington, J.; Henderson, J. I.; Rosenhein, L.; Heise, J. D.; Fanwick, P. E.; Kubiak, C. P. A Class of Halide-Supported Trinuclear Nickel Clusters $[Ni_3(\mu_3\text{-}L)(\mu_3\text{-}X)(\mu_2\text{-dppm})_3]^{n+}$ (L = I^-, Br^-, CO, CNR; X = I^-, Br^-; n = 0, 1; dppm = $Ph_2PCH_2PPh_2$): Novel Physical Properties and the Fermi Resonance of Symmetric μ_3-η^1 Bound Isocyanide Ligands. *J Am Chem Soc.* **1996**, *118* (9), 2198-2207. DOI: 10.1021/ja953010m.

(108) Maniaki, D.; Pilichos, E.; Perlepes, S. P. Coordination Clusters of 3d-Metals That Behave as Single-Molecule Magnets (SMMs): Synthetic Routes and Strategies. *Front. Chem.* **2018**, *6*, Review. DOI: 10.3389/fchem.2018.00461.

(109) Winpenny, R. *Molecular Cluster Magnets*; DOI: 10.1142/7902.

(110) Baran, P.; Boča, R.; Chakraborty, I.; Giapintzakis, J.; Herchel, R.; Huang, Q.; McGrady, J. E.; Raptis, R. G.; Sanakis, Y.; Simopoulos, A. Synthesis, Characterization, and Study of Octanuclear Iron-Oxo Clusters Containing a Redox-Active Fe_4O_4-Cubane Core. *Inorg. Chem.* **2008**, *47* (2), 645-655. DOI: 10.1021/ic7020337.

(111) Goddard, C. A.; Long, J. R.; Holm, R. H. Synthesis and Characterization of Four Consecutive Members of the Five-Member $[Fe_6S_8(PEt_3)_6]^{n+}$ (n = 0−4) Cluster Electron Transfer Series. *Inorg. Chem.* **1996**, *35* (15), 4347-4354. DOI: 10.1021/ic960052i.

(112) Zanello, P. Electrochemistry of Metal-sulfur Clusters: Stereochemical Consequences of Thermodynamically Characterized Redox Changes: Part II. Heterometal Clusters. *Coord. Chem. Rev.* **1988**, *87*, 1-54. DOI: 10.1016/0010-8545(88)80007-9.

(113) Champsaur, A. M.; Yu, J.; Roy, X.; Paley, D. W.; Steigerwald, M. L.; Nuckolls, C.; Bejger, C. M. Two-Dimensional Nanosheets from Redox-Active Superatoms. *ACS Cent. Sci.* **2017**, *3* (9), 1050-1055. DOI: 10.1021/acscentsci.7b00328.

(114) Freeman, M. B.; Edokobi, O. D.; Gillen, J. H.; Kocherga, M.; Dipple, K. M.; Jones, D. S.; Paley, D. W.; Wang, L.; Bejger, C. M. Stepwise Assembly of an Electroactive Framework from a Co_6S_8 Superatomic Metalloligand and Cuprous Iodide Building Units. *Chem Eur J.* **2020**, *26* (55), 12523-12527. DOI: 10.1002/chem.202001215.

.

(115) Horwitz, N. E.; Xie, J.; Filatov, A. S.; Papoular, R. J.; Shepard, W. E.; Zee, D. Z.; Grahn, M. P.; Gilder, C.; Anderson, J. S. Redox-active 1D Coordination Polymers of Iron–sulfur Clusters. *J Am Chem Soc* **2019**, *141* (9), 3940-3951. DOI: 10.1021/jacs.8b12339.

(116) Starikova, O. V.; Dolgushin, G. V.; Larina, L. I.; Komarova, T. N.; Lopyrev, V. A. Synthesis of New Stable Carbenes from the Corresponding 1,3-Dialkylimidazolium and Benzimidazolium Salts. *ARKIVOC* **2003**, (13), 119-124. DOI: 10.3998/ark.5550190.0004.d12.

(117) Huynh, H. V.; Han, Y.; Ho, J. H. H.; Tan, G. K. Palladium(II) Complexes of a Sterically Bulky, Benzannulated N-Heterocyclic Carbene with Unusual Intramolecular C−H···Pd and Ccarbene···Br Interactions and Their Catalytic Activities. *Organometallics* **2006**, *25* (13), 3267-3274. DOI: 10.1021/om060151w.

(118) Fagan, V.; Bonham, S.; Carty, M. P.; Aldabbagh, F. One-pot Double Intramolecular Homolytic Aromatic Substitution Routes to Dialicyclic Ring Fused Imidazobenzimidazolequinones and Preliminary Analysis of Anticancer Activity. *Org Biomol Chem.* **2010**, *8* (14), 3149-3156. DOI: 10.1039/C003511D.

(119) Deng, L.; Bill, E.; Wieghardt, K.; Holm, R. H. Cubane-Type Co_4S_4 Clusters: Synthesis, Redox Series, and Magnetic Ground States. *J Am.Chem Soc.* **2009**, *131* (31), 11213-11221, Article. DOI: 10.1021/ja903847a.

(120) Kamplain, J. W.; Bielawski, C. W. Dynamic Covalent Polymers Based Upon Carbene Dimerization. *Chem. Commun.* **2006**, (16), 1727-1729. DOI: 10.1039/B518246H.

(121) Wang, Y.; Poirier, R. A. Factors that Influence the CN Stretching Frequency in Imines. *J Phys Chem A.* **1997**, *101* (5), 907-912. DOI: 10.1021/jp9617332.

(122) Ma, X.; Zhang, W.; Deng, Y.; Zhong, C.; Hu, W.; Han, X. Phase and Composition Controlled Synthesis of Cobalt Sulfide Hollow Nanospheres for Electrocatalytic Water Splitting. *Nanoscale* **2018**, *10* (10), 4816-4824. DOI: 10.1039/C7NR09424H.

(123) Gong, Y.-N.; Zhong, D.-C.; Lu, T.-B. Interpenetrating Metal–organic Frameworks. *CrystEngComm.* **2016**, *18* (15), 2596-2606. DOI: 10.1039/C6CE00371K.

(124) Dodson, R. A.; Wong-Foy, A. G.; Matzger, A. J. The Metal–Organic Framework Collapse Continuum: Insights from Two-Dimensional Powder X-ray Diffraction. *Chem. Mat.* **2018**, *30* (18), 6559-6565. DOI: 10.1021/acs.chemmater.8b03378.

(125) Smock, S. R.; Alimento, R.; Mallikarjun Sharada, S.; Brutchey, R. L. Probing the Ligand Exchange of N-heterocyclic Carbene-capped Ag_2S Nanocrystals with Amines and Carboxylic Acids. *Inorg Chem.* **2021**, *60* (17), 13699-13706. DOI: 10.1021/acs.inorgchem.1c02018.

(126) Titcomb, L. R.; Caddick, S.; Cloke, F. G. N.; Wilson, D. J.; McKerrecher, D. Unexpected Reactivity of Two-Coordinate Palladium–Carbene Complexes;

Synthetic and Catalytic Implications. *Chem Commun.* **2001**, (15), 1388-1389. DOI: 10.1039/B104297C.

(127) Schuster, O.; Yang, L.; Raubenheimer, H. G.; Albrecht, M. Beyond Conventional N-heterocyclic Carbenes: Abnormal, Remote, and Other Classes of NHC Ligands with Reduced Heteroatom Stabilization. *Chem Rev.* **2009**, *109* (8), 3445-3478. DOI: 10.1021/cr8005087.

(128) *CrysAlisPro*; Rigaku Corporation: Oxford, UK, 2018.

(129) Sheldrick, G. Crystal structure refinement with SHELXL. *Acta Crystallographica Section C* **2015**, *71* (1), 3-8. DOI: 10.1107/S2053229614024218.

(130) Sheldrick, G. A short history of SHELX. *Acta Crystallographica Section A* **2008**, *64* (1), 112-122. DOI: 10.1107/S0108767307043930.

(131) Dolomanov, O. V.; Bourhis, L. J.; Gildea, R. J.; Howard, J. A. K.; Puschmann, H. OLEX2: a Complete Structure Solution, Refinement and Analysis Program. *J Appl Crystallogr.* **2009**, *42* (2), 339-341. DOI: 10.1107/S0021889808042726.

(132) van der Sluis, P.; Spek, A. L. BYPASS: an Effective Method for the Refinement of Crystal Structures Containing Disordered Solvent Regions. *Acta Crystallographica Section A* **1990**, *46* (3), 194-201. DOI: 10.1107/S0108767389011189.

(133) Farrugia, L. WinGX and ORTEP for Windows: an Update. *J Appl Crystallogr.* **2012**, *45* (4), 849-854. DOI: 10.1107/S0021889812029111.

(134) Claridge, S. A.; Castleman, A. W., Jr.; Khanna, S. N.; Murray, C. B.; Sen, A.; Weiss, P. S. Cluster-assembled Materials. *ACS Nano* **2009**, *3* (2), 244-255. DOI: 10.1021/nn800820e.

(135) Jena, P.; Sun, Q. Super Atomic Clusters: Design Rules and Potential for Building Blocks of Materials. *Chem Rev.* **2018**, *118* (11), 5755-5870. DOI: 10.1021/acs.chemrev.7b00524

(136) Roy, X.; Lee, C. H.; Crowther, A. C.; Schenck, C. L.; Besara, T.; Lalancette, R. A.; Siegrist, T.; Stephens, P. W.; Brus, L. E.; Kim, P.; et al. Nanoscale Atoms in Solid-State Chemistry. *Sci.* **2013**, *341* (6142), 157-160. DOI: 10.1126/science.1236259.

(137) Yang, J. J.; Russell, J. C.; Tao, S. S.; Lessio, M.; Wang, F. F.; Hartnett, A. C.; Peurifoy, S. R.; Doud, E. A.; O'Brien, E. S.; Gadjieva, N.; et al. Superatomic Solid Solutions. *Nat Chem.* **2021**, *13* (6), 607-613. DOI: 10.1038/s41557-021-00680-8.

(138) Turkiewicz, A.; Paley, D. W.; Besara, T.; Elbaz, G.; Pinkard, A.; Siegrist, T.; Roy, X. Assembling Hierarchical Cluster Solids with Atomic Precision. *J Am Chem Soc* **2014**, *136* (45), 15873-15876. DOI: 10.1021/ja508698w.

(139) Schulz-Dobrick, M.; Jansen, M. Intermolecular Forces in Intercluster Compounds Consisting of Gold Clusters and Fullerides and in a Series of Model Compounds $C_{60}\cdot 2(PR_3)AuCl$. *CrystEngComm* **2008**, *10* (6), 661-664. DOI: 10.1039/B800093J.

(140) Lee, C. H.; Liu, L.; Bejger, C.; Turkiewicz, A.; Goko, T.; Arguello, C. J.; Frandsen, B. A.; Cheung, S. C.; Medina, T.; Munsie, T. J. S.; et al. Ferromagnetic Ordering in Superatomic Solids. *J Am Chem Soc.* **2014**, *136* (48), 16926-16931. DOI: 10.1021/ja5098622.

(141) Shott, J. L.; Freeman, M. B.; Saleh, N. A.; Jones, D. S.; Paley, D. W.; Bejger, C. Ball and Socket Assembly of Binary Superatomic Solids Containing Trinuclear Nickel Cluster Cations and Fulleride Anions. *Inorg Chem* **2017**, *56* (18), 10984-10990. DOI: 10.1021/acs.inorgchem.7b01259.

(142) O'Brien, E. S.; Russell, J. C.; Bartnof, M.; Christodoulides, A. D.; Lee, K.; DeGayner, J. A.; Paley, D. W.; McGaughey, A. J. H.; Ong, W. L.; Malen, J. A.; et al. Spontaneous Electronic Band Formation and Switchable Behaviors in a Phase-Rich Superatomic Crystal. *J Am Chem Soc.* **2018**, *140* (46), 15601-15605. DOI: 10.1021/jacs.8b09905.

(143) Voevodin, A.; Abella, L.; Castro, E.; Paley, D. W.; Campos, L. M.; Rodriguez-Fortea, A.; Poblet, J. M.; Echegoyen, L.; Roy, X. Dimerization of Endohedral Fullerene in a Superatomic Crystal. *Chem.* **2017**, *23* (54), 13305-13308. DOI: 10.1002/chem.201703203.

(144) O'Brien, E. S.; Trinh, M. T.; Kann, R. L.; Chen, J.; Elbaz, G. A.; Masurkar, A.; Atallah, T. L.; Paley, M. V.; Patel, N.; Paley, D. W.; et al. Single-crystal-to-single-crystal Intercalation of a Low-bandgap Superatomic Crystal. *Nat Chem.* **2017**, *9* (12), 1170-1174. DOI: 10.1038/Nchem.2844.

(145) Ong, W. L.; O'Brien, E. S.; Dougherty, P. S.; Paley, D. W.; Fred Higgs Iii, C.; McGaughey, A. J.; Malen, J. A.; Roy, X. Orientational Order Controls Crystalline and Amorphous Thermal Transport in Superatomic Crystals. *Nat Mater.* **2017**, *16* (1), 83-88. DOI: 10.1038/nmat4739.

(146) Kephart, J. A.; Romero, C. G.; Tseng, C. C.; Anderton, K. J.; Yankowitz, M.; Kaminsky, W.; Velian, A. Hierarchical Nanosheets Built from Superatomic Clusters: Properties, Exfoliation and Single-crystal-to-single-crystal Intercalation. *Chem Sci.* **2020**, *11* (39), 10744-10751. DOI: 10.1039/d0sc03506h.

(147) Lee, K.; Choi, B.; Plante, I. J.; Paley, M. V.; Zhong, X.; Crowther, A. C.; Owen, J. S.; Zhu, X.; Roy, X. Two-Dimensional Fullerene Assembly from an Exfoliated van der Waals Template. *Angew Chem Int Ed Engl.* **2018**, *57* (21), 6125-6129. DOI: 10.1002/anie.201800953.

(148) Choi, B.; Yu, J.; Paley, D. W.; Trinh, M. T.; Paley, M. V.; Karch, J. M.; Crowther, A. C.; Lee, C. H.; Lalancette, R. A.; Zhu, X.; et al. van der Waals Solids from Self-Assembled Nanoscale Building Blocks. *Nano Lett.* **2016**, *16* (2), 1445-1449. DOI: 10.1021/acs.nanolett.5b05049.

(149) Gillen, J. H.; Moore, C. A.; Vuong, M.; Shajahan, J.; Anstey, M. R.; Alston, J. R.; Bejger, C. M. Synthesis and Disassembly of an Organometallic Polymer Comprising Redox-Active Co_4S_4 Clusters and Janus Biscarbene Linkers. *Chem Commun.* **2022**, *58* (31), 4885-4888. DOI: 10.1039/D2CC00953F.

(150) Selby, H. D.; Roland, B. K.; Zheng, Z. Ligand-Bridged Oligomeric and Supramolecular Arrays of the Hexanuclear Rhenium Selenide Clusters− Exploratory Synthesis, Structural Characterization, and Property Investigation. *Acc Chem Res.* **2003**, *36* (12), 933-944. DOI: 10.1021/ar020134c.

(151) Xie, J.; Wang, L.; Anderson, J. S. Heavy Chalcogenide-transition Metal Clusters as Coordination Polymer Nodes. *Chem Sci.* **2020**, *11* (32), 8350-8372. DOI: 10.1039/d0sc03429k.

(152) Shores, M. P.; Beauvais, L. G.; Long, J. R. Cluster-expanded Prussian Blue Analogues. *J Am Chem Soc.* **1999**, *121* (4), 775-779. DOI: 10.1021/ja983530s.

(153) Yu, M.; Liu, C.; Li, S.; Zhao, Y.; Lv, J.; Zhuo, Z.; Jiang, F.; Chen, L.; Yu, Y.; Hong, M. Constructing Multi-cluster Copper (I) Halides Using Conformationally Flexible Ligands. *Chem Commun.* **2020**, *56* (53), 7233-7236. DOI: 10.1039/D0CC02472D.

(154) Fang, Y.; Liu, W.; Teat, S. J.; Dey, G.; Shen, Z.; An, L.; Yu, D.; Wang, L.; O'Carroll, D. M.; Li, J. A Systematic Approach to Achieving High Performance Hybrid Lighting Phosphors with Excellent Thermal and Photostability. *Adv Funct Mater.* **2017**, *27* (3), 1603444. DOI: 10.1002/adfm.201603444.

(155) Benito, Q.; Desboeufs, N.; Fargues, A.; Garcia, A.; Massuyeau, F.; Martineau-Corcos, C.; Devic, T.; Perruchas, S. A Photoactive Copper Iodide Phosphine-based Coordination Polymer. *NJC.* **2020**, *44* (45), 19850-19857.

(156) Nohra, B.; El Moll, H.; Rodriguez Albelo, L. M.; Mialane, P.; Marrot, J.; Mellot-Draznieks, C.; O'keeffe, M.; Ngo Biboum, R.; Lemaire, J.; Keita, B. Polyoxometalate-based Metal Organic Frameworks (POMOFs): Structural Trends, Energetics, and High Electrocatalytic Efficiency for Hydrogen Evolution Reaction. *J Am Chem Soc* **2011**, *133* (34), 13363-13374. DOI: 10.1021/ja201165c.

(157) Stuckart, M.; Monakhov, K. Y. Polyoxometalates as components of Supramolecular Assemblies. *Chem Sci.* **2019**, *10* (16), 4364-4376. DOI: 10.1039/C9SC00979E.

(158) Fang, W.-H.; Wang, J.-F.; Zhang, L.; Zhang, J. Titanium–oxo Cluster Based Precise Assembly for Multidimensional Materials. *Chem Mater.* **2017**, *29* (7), 2681-2684. DOI: 10.1021/acs.chemmater.7b00324.

(159) Liu, X.; McPherson, J. N.; Andersen, C. E.; Jørgensen, M. S.; Larsen, R. W.; Yutronkie, N. J.; Wilhelm, F.; Rogalev, A.; Giménez-Marqués, M.; Mínguez Espallargas, G. A Zero-valent Palladium Cluster-organic Framework. *Nat comm.* **2024**, *15* (1), 1177. DOI: 10.1038/s41467-024-45363-3.

(160) Champsaur, A. M.; Mézière, C.; Allain, M.; Paley, D. W.; Steigerwald, M. L.; Nuckolls, C.; Batail, P. Weaving Nanoscale Cloth through Electrostatic Templating. *J Am Chem Soc.* **2017**, *139* (34), 11718-11721. DOI: 10.1021/jacs.7b07279.

(161) Williams, D. E.; Dolgopolova, E. A.; Godfrey, D. C.; Ermolaeva, E. D.; Pellechia, P. J.; Greytak, A. B.; Smith, M. D.; Avdoshenko, S. M.; Popov, A. A.; Shustova,

N. B. Fulleretic Well-Defined Scaffolds: Donor–Fullerene Alignment Through Metal Coordination and Its Effect on Photophysics. *Ange Chem Int Ed.* **2016**, *55* (31), 9070-9074. DOI: 10.1002/anie.201603584

(162) Sikdar, N.; Hazra, A.; Samanta, D.; Haldar, R.; Maji, T. K. Guest-Responsive Reversible Electron Transfer in a Crystalline Porous Framework Supported by a Dynamic Building Node. *Ange Chem.* **2020**, *132* (42), 18637-18642. DOI: 10.1002/anie.202008189

(163) Sikdar, N.; Jayaramulu, K.; Kiran, V.; Rao, K. V.; Sampath, S.; George, S. J.; Maji, T. K. Redox-Active Metal–Organic Frameworks: Highly Stable Charge-Separated States through Strut/Guest-to-Strut Electron Transfer. *Chem - Eur J.* **2015**, *21* (33), 11701-11706. DOI: 10.1002/chem.201501614.

(164) Yan, T.; Li, Y. Y.; Su, J.; Wang, H. Y.; Zuo, J. L. Charge Transfer Metal-Organic Framework Containing Redox-Active TTF/NDI Units for Highly Efficient Near-Infrared Photothermal Conversion. *Chem - Eur J.* **2021**, *27* (43), 11050-11055. DOI: 10.1002/chem.202101607.

(165) Haldar, R.; Ghosh, A.; Maji, T. K. Charge Transfer in Metal–Organic Frameworks. *Chem Comm.* **2023**, *59* (12), 1569-1588. DOI: 10.1039/D2CC05522H.

(166) Zhang, B.; Qian, B.-B.; Li, C.-T.; Li, X.-W.; Nie, H.-X.; Yu, M.-H.; Chang, Z. Donor–acceptor Systems in Metal–organic Frameworks: Design, Construction, and Properties. *CrystEngComm.* **2022**, *24* (31), 5538-5551. DOI: 10.1039/D2CE00588C.

(167) Kumar, M.; Rao, K. V.; George, S. J. Supramolecular Charge Transfer Nanostructures. *Phys Chem Chem Phys.* **2014**, *16* (4), 1300-1313. DOI: 10.1039/C3CP54190H.

(168) Liu, W.; Zhu, K.; Teat, S. J.; Dey, G.; Shen, Z.; Wang, L.; O'Carroll, D. M.; Li, J. All-in-one: Achieving Robust, Strongly Luminescent and Highly Dispersible Hybrid Materials by Combining Ionic and Coordinate Bonds in Molecular Crystals. *J Am Chem Soc* **2017**, *139* (27), 9281-9290. DOI: 10.1021/jacs.7b04550

(169) Hei, X.; Liu, W.; Zhu, K.; Teat, S. J.; Jensen, S.; Li, M.; O'Carroll, D. M.; Wei, K.; Tan, K.; Cotlet, M. Blending Ionic and Coordinate Bonds in Hybrid Semiconductor Materials: A General Approach Toward Robust and Solution-Processable Covalent/Coordinate Network Structures. *J Am Chem Soc.* **2020**, *142* (9), 4242-4253. DOI: 10.1021/jacs.9b13772.

(170) Beinert, H.; Holm, R. H.; Münck, E. Iron-Sulfur Clusters: Nature's Modular, Multipurpose Structures. *Sci.* **1997**, *277* (5326), 653-659. DOI: 10.1126/science.277.5326.653

(171) Zhou, H.-C.; Holm, R. H. Synthesis and Reactions of Cubane-Type Iron−Sulfur−Phosphine Clusters, Including Soluble Clusters of Nuclearities 8 and 16. *Inorg Chem.* **2003**, *42* (1), 11-21. DOI: 10.1021/ic020464t.

(172) Scott, T. A.; Zhou, H.-C. The First All-Cyanide Fe_4S_4 Cluster: $[Fe_4S_4(CN)_4]^{3-}$. *Ange Chem Int Ed.* **2004**, *43* (42), 5628-5631. DOI: 10.1002/anie.200460879.

(173) Ye, M.; Thompson, N. B.; Brown, A. C.; Suess, D. L. M. A Synthetic Model of Enzymatic [Fe_4S_4]–Alkyl Intermediates. *J Am Chem Soc.* **2019**, *141* (34), 13330-13335. DOI: 10.1021/jacs.9b06975.

(174) Yang, J.; Zhang, B.; Christodoulides, A. D.; Xu, Q.; Zangiabadi, A.; Peurifoy, S. R.; McGinn, C. K.; Dai, L.; Meirzadeh, E.; Roy, X. Solution-processable superatomic thin-films. *J Am Chem Soc* **2019**, *141* (28), 10967-10971. DOI: 10.1021/jacs.9b04705 .

(175) Echegoyen, L.; Echegoyen, L. E. Electrochemistry of Fullerenes and Their Derivatives. *Acc Chem Res* **1998**, *31* (9), 593-601. DOI: 10.1021/ar970138v.

(176) Reed, C. A.; Bolskar, R. D. Discrete Fulleride Anions and Fullerenium Cations. *Chem Rev.* **2000**, *100* (3), 1075-1120. DOI: 10.1021/cr980017o.

(177) Wudl, F.; Bryce, M. R. Apparatus for Two-Probe Conductivity Measurements on Compressed Powders. *J Chem Ed.* **1990**, *67* (8), 717. DOI: 10.1021/ed067p717

(178) Hasan, F.; Gillen, J. H.; Jayaweera, A. T.; McDearmon Jr., W. D.; Winter, A. H.; Bejger, C. M. Cover Feature: Simple Air-Stable [3]Radialene Anion Radicals as Environmentally Switchable Catholytes in Water. *Chem – Eur J.* **2024**, *30* (7), e202304340. DOI: 10.1002/chem.202304340.

(179) Xu, T.; Zhu, J.; Han, Y.; Chi, C. Carbon-centered Radical Based Dynamic Covalent Chemistry for Stimuli-responsive Chromic mMaterials. *J Mater Chem C.* **2023**, *11* (24), 7957-7969. DOI: 10.1039/D3TC00117B.

(180) Chaka, M. D.; Geffe, C. A.; Rodriguez, A.; Seriani, N.; Wu, Q.; Mekonnen, Y. S. High-Throughput Screening of Promising Redox-Active Molecules with MolGAT. *ACS Omega* **2023**, *8* (27), 24268-24278. DOI: 10.1021/acsomega.3c01295.

(181) Peterson, J. P.; Ellern, A.; Winter, A. H. Spin Delocalization, Polarization, and London Dispersion Forces Govern the Formation of Diradical Pimers. *J. Am. Chem. Soc.* **2020**, *142* (11), 5304-5313. DOI: 10.1021/jacs.0c00190.

(182) Meng, E. C.; Goddard, T. D.; Pettersen, E. F.; Couch, G. S.; Pearson, Z. J.; Morris, J. H.; Ferrin, T. E. UCSF ChimeraX: Tools For Structure Building and Analysis. *Protein Science* **2023**, *32* (11), e4792. DOI:10.1002/pro.4792.

(183) Schaefer, A. J.; Ingman, V. M.; Wheeler, S. E. SEQCROW: A ChimeraX Bundle to Facilitate Quantum Chemical Applications to Complex Molecular Systems. *J Comput Chem* **2021**, *42* (24), 1750-1754. DOI: 10.1002/jcc.26700.

(184) Ho, J. Are Thermodynamic Cycles Necessary for Continuum Solvent Calculation of pK_as and Reduction Potentials? *Phys Chem Chem Phys.* **2015**, *17* (4), 2859-2868. DOI: 10.1039/C4CP04538F.

(185) Fonseca Guerra, C.; Handgraaf, J.-W.; Baerends, E. J.; Bickelhaupt, F. M. Voronoi Deformation Density (VDD) Charges: Assessment of the Mulliken, Bader, Hirshfeld, Weinhold, and VDD Methods for Charge Analysis. *Journal of Computational Chemistry* **2004**, *25* (2), 189-210. DOI: 10.1002/jcc.10351.

(186) Bickelhaupt, F. M.; Ziegler, T.; Schleyer, P. v. R. $CH_3^{\bullet}$ Is Planar Due to H−H Steric Repulsion. Theoretical Study of $MH_3^{\bullet}$ and MH_3Cl (M = C, Si, Ge, Sn). *Organometallics* **1996**, *15* (5), 1477-1487. DOI: 10.1021/om950560k.

(187) Blokker, E.; ten Brink, M.; van der Schuur, J. M.; Hamlin, T. A.; Bickelhaupt, F. M. Origin of the Captodative Effect: The Lone-Pair Shielded Radical. *ChemistryEurope* **2023**, *1* (1), e202300006. DOI: 10.1002/ceur.202300006.

(188) Pierrefixe, S. C. A. H.; van Stralen, S. J. M.; van Stralen, J. N. P.; Fonseca Guerra, C.; Bickelhaupt, F. M. Hypervalent Carbon Atom: "Freezing" the S_N2 Transition State. *Ange Chem Int Ed.* **2009**, *48* (35), 6469-6471. DOI: 10.1002/anie.200902125.

(189) Wood, G. P. F.; Moran, D.; Jacob, R.; Radom, L. Bond Dissociation Energies and Radical Stabilization Energies Associated with Model Peptide-Backbone Radicals. *J Phys Chem A.* **2005**, *109* (28), 6318-6325. DOI: 10.1021/jp051860a.

(190) Fonseca Guerra, C.; Bickelhaupt, F. M.; Snijders, J. G.; Baerends, E. J. The Nature of the Hydrogen Bond in DNA Base Pairs: The Role of Charge Transfer and Resonance Assistance. *Chem – Euro J.* **1999**, *5* (12), 3581-3594. DOI: 10.1002/(SICI)1521-3765(19991203)5:12<3581::AID-CHEM3581>3.0.CO;2-Y.